



AMERICAN UNIVERSITY OF BEIRUT

PROPAGATION BEHAVIOR OF GUIDED WAVES IN TIMBER  
UTILITY POLES – TOWARDS APPLICATION IN NON-  
DESTRUCTIVE EVALUATION

by  
JAD JIHAD EL NAJJAR

A thesis  
submitted in partial fulfillment of the requirements  
for the degree of Master of Engineering  
to the Department of Mechanical Engineering  
of the Maroun Semaan Faculty of Engineering and Architecture  
at the American University of Beirut

Beirut, Lebanon  
February 2020

AMERICAN UNIVERSITY OF BEIRUT

PROPAGATION BEHAVIOR OF GUIDED WAVES IN TIMBER  
UTILITY POLES – TOWARDS APPLICATION IN NON-  
DESTRUCTIVE EVALUATION

by  
JAD JIHAD EL NAJJAR

Approved by:



---

Dr. Samir Mustapha, Assistant Professor  
Mechanical Engineering Department

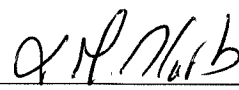
Advisor



---

Dr. Shadi Najjar, Associate Professor  
Civil and Environmental Engineering Department

Member of Committee



---

Dr. Mohammad Harb, Assistant Professor  
Mechanical Engineering Department

Member of Committee

Date of thesis/dissertation defense: 02/12/2020

AMERICAN UNIVERSITY OF BEIRUT

THESIS, DISSERTATION, PROJECT RELEASE FORM

Student Name: EL NAJJAR JAD JIHAD  
Last First Middle

Master's Thesis  Master's Project  Doctoral  
Dissertation

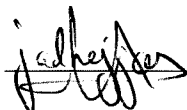
I authorize the American University of Beirut to: (a) reproduce hard or electronic copies of my thesis, dissertation, or project; (b) include such copies in the archives and digital repositories of the University; and (c) make freely available such copies to third parties for research or educational purposes.

I authorize the American University of Beirut, to: (a) reproduce hard or electronic copies of it; (b) include such copies in the archives and digital repositories of the University; and (c) make freely available such copies to third parties for research or educational purposes

after : **One** ---- year from the date of submission of my thesis, dissertation, or project.

**Two** ---- years from the date of submission of my thesis, dissertation, or project.

**Three** ---- years from the date of submission of my thesis, dissertation, or project.

  
Signature

17-02-2020  
Date

This form is signed when submitting the thesis, dissertation, or project to the University Libraries



## ACKNOWLEDGMENTS

I would first like to express my sincere appreciation to my thesis advisor, Dr. Samir Mustapha, who has always showed support, guidance and encouragement throughout my time as a graduate student at AUB. It has truly been a pleasure working and learning from you.

I would like to acknowledge the advice given by the thesis committee, Dr. Mohamad Harb and Dr. Shadi Najjar. The assistance provided by Dr. Harb with my research topic was greatly appreciated.

I wish to extend my special thanks to all my colleagues at AUB, for helping me reach my goal and for always being there.

I want to express my gratitude to my family members and friends for all that I have accomplished.

We acknowledge the financial support of the University Research Board at the American University of Beirut for their Award #103780.

# AN ABSTRACT OF THE THESIS OF

Jad Jihad El Najjar for Master of Engineering  
Major: Mechanical Engineering

Title: Propagation Behavior of Guided Waves in Timber Utility Poles – Towards Application in Non-destructive Evaluation

## ABSTRACT

Long standing in-service utility timber poles require careful health monitoring to prevent them from failure and extend their lifecycle. In this work, we are proposing the application of ultrasonic guided waves (GWs) for the assessment of the embedded length and the health state of western white pine timber pole. The work combined both experimental and numerical modeling using COMSOL Multiphysics.

Macro Fiber Composites (MFCs), due to their flexibility and convenience to install on curved profiles, were used to actuate and sense guided waves along the tested structures. Based on the wave propagation characteristics in these types of structures, an MFC ring was designed and developed. The ring is to ensure the excitation of the wave modes of interest, i.e. with high sensitivity to the presence of defects, at an enhanced amplitude and to reduce the complexity of the captured signals. We have studied the effect of external boundary conditions, such as soil embedment, on GW propagation, as well as the assessment of the health state of the structure under study.

According to our investigation, the soil had minimum impact on the wave propagation characteristics, given that the waves were confined in the timber pole with minimal leakage to the surrounding. The embedded length of the pole was determined accurately, using both experimental and numerical data, with an error less than 3 %. The deterioration in the timber, within the embedded region, was also evaluated and high accuracy was obtained in localizing the damage with a maximum error of 7 %.

Based on the obtained results, guided waves have high potential to be used as a non-destructive tool for assessment and evaluation of timber utility poles.

# CONTENTS

ACKNOWLEDGMENTS .....	v
ABSTRACT .....	vi
ILLUSTRATIONS .....	x
TABLES .....	xvi
Chapter 1 Introduction.....	1
1.1. Background.....	1
1.2. Timber Poles – Applications.....	2
1.3. Decays and Defects in Timber.....	4
Chapter 2 Literature Review .....	8
2.1. Overview.....	8
2.2. Condition Assessment Using Guided Waves .....	12
2.3. Timber Poles Evaluation – Different Practices.....	14
2.3.1. Visual Inspection .....	14
2.3.2. Resistance Drilling .....	14
2.3.3. Radioscopy .....	15
2.3.4. Microwave/Ground Penetrating Radar.....	15
2.3.5. Vibration Methods.....	16
2.4. One-dimensional (1D) Wave Theory .....	16
2.4.1. 1-D Wave Theory Based Non-destructive Testing .....	18
2.4.2. In-situ Assessment of Timber Poles – Ultrasonic Stress Waves.....	20

2.4.3.	Limitations of One-Dimensional Stress Wave Based NDT .....	29
2.5.	Three-dimensional (3D) Guided Wave Theory in Cylindrical Structures.....	30
2.5.1.	Guided Wave Behavior in Isotropic Cylindrical Structures.....	32
2.5.2.	Guided Wave Behavior in Transversely Isotropic Cylindrical Structures 37	
2.5.3.	Limitations of Guided Wave Based NDT .....	40

## Chapter 3 Understanding Guided Wave Propagation Behavior in Utility Timber Poles .....

42

3.1.	Introduction.....	42
3.2.	Methodology .....	43
3.2.1.	Overview .....	43
3.2.2.	Numerical FEA Model .....	62
3.2.3.	Experimental Setup .....	72
3.3.	Signal Processing.....	79
3.4.	Results & Analysis.....	82
3.4.1.	Tuning of the Excitation Frequency .....	82
3.4.2.	MFC – Timber Matching (Experimental) .....	88
3.4.3.	Reducing the Effects of Dispersion (Experimental).....	92
3.4.4.	Ring Design .....	94
3.4.5.	Validation of the Ring Design and Effect of Boundary Conditions.....	101
3.5.	Discussion.....	111

## Chapter 4 Condition Assessment and Damage Detection in Timber Utility Poles using Guided Waves .....

114

4.1.	Introduction.....	114
------	-------------------	-----

4.2. Methodology .....	115
4.2.1. Numerical FEA Model .....	115
4.2.2. Experimental Setup .....	118
4.3. Results and Analysis .....	123
4.3.1. Effect of Boundary Conditions.....	123
4.3.2. Effect of Damage Induction .....	123
4.3.3. Length Estimation and Damage Localization .....	133
4.4. Discussion.....	139
<b>Chapter 5 Future Work.....</b>	<b>142</b>
<b>Chapter 6 Conclusions.....</b>	<b>144</b>
<b>BIBLIOGRAPHY .....</b>	<b>147</b>

## ILLUSTRATIONS

FIGURE 1.1 TIMBER UTILITY POLES.....	3
FIGURE 1.2 (A) BROWN AND (B) WHITE ROTTS IN WOODEN POLES. ....	5
FIGURE 1.3 VARIOUS TYPES OF INSECTS AFFECTING WOOD: (A) TERMITES, (B) CARPENTER ANTS, (C) LYCTUS BEETLES AND (D) CADDIS FLIES. ....	6
FIGURE 1.4 DECAYS IN WOOD CAUSED BY INSECTS.....	7
FIGURE 2.1 SENSOR PLACEMENT AROUND THE CROSS SECTION OF A SPECIMEN [5]. ....	22
FIGURE 2.2 X-RAY CONFIGURATION ON FIXED SPECIMENS.....	25
FIGURE 2.3 TWO-DIMENSIONAL TOMOGRAM OF A TIMBER POST [5].....	26
FIGURE 2.4 DISPERSION CURVES FOR ISOTROPIC MULTILAYERED WOOD: (A) PHASE AND (B) GROUP VELOCITY VS. FREQUENCY PLOTS.....	35
FIGURE 3.1 ORIENTATION OF GROWTH RINGS IN CIRCULAR TIMBER (PINE). 44	
FIGURE 3.2 GROWTH RING ORIENTATION IN THE LAB'S TIMBER SPECIMEN. 46	
FIGURE 3.3 COORDINATE SYSTEM FOR THE CYLINDRICAL TIMBER POLE. ....	46
FIGURE 3.4 DISPLACEMENT COMPONENTS IN CYLINDRICAL ELEMENTS. ....	48
FIGURE 3.5 NON-DISPERSIVE PROPAGATING WAVE PACKET [32].....	49
FIGURE 3.6 DISPERSIVE PROPAGATING WAVE PACKET [32].....	50
FIGURE 3.7 GAUSSIAN FUNCTIONS FOR A NON-DISPERSIVE PACKET (BLACK) AND A DISPERSIVE PACKET (BLUE) [32].....	50
FIGURE 3.8 15KHZ DISPERSIVE WAVE PACKET OF A 4-CYCLE BURST [33].....	51
FIGURE 3.9 5-CYCLE HANNING WINDOW BURST AT 15 KHZ: (A) ORIGINAL CYCLE AND (B) SINGLE SIDED AMPLITUDE SPECTRUM AFTER FOURIER TRANSFORM.....	52
FIGURE 3.10 10-CYCLE HANNING WINDOW BURST AT 15 KHZ: (A) ORIGINAL CYCLE AND (B) SINGLE SIDED AMPLITUDE SPECTRUM AFTER FOURIER TRANSFORM.....	53
FIGURE 3.11 DISPERSION CURVES: (A) GROUP VELOCITY AND (B) PHASE VELOCITY VS. FREQUENCY FOR LONGITUDINAL WAVE MODES.....	54

FIGURE 3.12 DISPERSION CURVES: (A) GROUP VELOCITY AND (B) PHASE VELOCITY VS. FREQUENCY FOR FLEXURAL WAVE MODES OF ORDER 1.55	
FIGURE 3.13 DISPERSION CURVES: GROUP VELOCITY VS. FREQUENCY FOR FLEXURAL WAVE MODES OF ORDERS (A) F(2,M), (B) F(4,M) AND (C) F(8,M).....	56
FIGURE 3.14 WAVELENGTH VS. FREQUENCY.....	57
FIGURE 3.15 MODE SHAPES FOR DIFFERENT THICKNESS NUMBER VALUES (LONGITUDINAL WAVE MODES) [35].....	58
FIGURE 3.16 LONGITUDINAL, TORSIONAL AND FLEXURAL DEFORMATION OF A CYLINDRICAL TUBE [36].....	59
FIGURE 3.17 PARTICLE DISPLACEMENT IN QUASI-LONGITUDINAL WAVES. ...	62
FIGURE 3.18 PARTICLE DISPLACEMENT IN PURE LONGITUDINAL WAVES.....	62
FIGURE 3.19 DISPERSION CURVES: (A) GROUP VELOCITY VS. FREQUENCY PLOT FOR F(4,M) WAVE MODE AND (B) WAVELENGTH VS. FREQUENCY PLOT FOR FLEXURAL MODES F(1,M).....	66
FIGURE 3.20 TIMBER POLE: (A) RING DESIGN MODEL AND (B) 8.8 MM MESH SIZE APPLIED TO THE MODEL IN COMSOL.....	66
FIGURE 3.21 TOP VIEW SKETCH OF THE TIMBER POLE DISPLAYING THE EMBEDDED CONDITION AND THE TRANSDUCERS' LOCATIONS. ....	67
FIGURE 3.22 5.5-METER TIMBER POLE IN COMSOL: (A) TRACTION FREE MODEL, (B) EMBEDDED MODEL, (C) MFC ACTUATOR RING AND SENSOR PLACEMENT AND (D) 5.5 MM MESH APPLIED TO THE EMBEDDED MODEL. ....	69
FIGURE 3.23 SCHEMATIC STRUCTURE OF THE MFC [49].....	70
FIGURE 3.24 VOLTAGE APPLICATION SCHEMATIC AND POLARIZATION DIRECTION OF THE MFC.....	71
FIGURE 3.25 SCHEME OF THE MFC ACTING AS SENSOR.....	72
FIGURE 3.26 MFC CONFIGURATION ON THE TIMBER POLE DISPLAYING THE MFC ACTUATOR RING AND SENSORS.....	74

FIGURE 3.27 (A) 8-METER TIMBER UTILITY POLE AND (B) MFC ACTUATORS AND SENSOR CONFIGURATION ON THE BOTTOM END OF THE POLE.....	75
FIGURE 3.28 RING DESIGN EXPERIMENTAL SETUP.....	76
FIGURE 3.29 SMOOTHING THE POLE'S SURFACE WITH SANDPAPER BEFORE MFC COUPLING. ....	77
FIGURE 3.30 DRY THIN LAYER OF EPOXY ADHESIVE APPLIED FOR ADDITIONAL SMOOTHING. ....	77
FIGURE 3.31 MFC COUPLED AND PRESSED ON ONE POSITION OF THE POLE'S SURFACE.....	78
FIGURE 3.32 8-MFC RING COUPLED AROUND THE CIRCUMFERENCE USED FOR ACTUATION.....	79
FIGURE 3.33 (A) ORIGINAL EXPERIMENTAL ACQUIRED SIGNALS AT 12.5 KHZ FOR TRACTION FREE (SOLID) AND EMBEDDED (DASHED) SINGLE MFC ACTUATION ON THE 8-METER LENGTH POLE, (B) TO (E) SHOW THE FOUR IMFS OF THE SIGNALS AFTER APPLYING CEEMD.....	81
FIGURE 3.34 EXPERIMENTAL CONFIGURATION FOR TUNING THE EXCITATION FREQUENCY. ....	82
FIGURE 3.35 NUMERICAL RESULTS: MFC4 TOP ACQUIRED SIGNAL USING SINGLE MFC ACTUATION AT (A) 10 KHZ, (B) 12.5 KHZ, (C) 15 KHZ, (D) 17.5 KHZ, (E) 20 KHZ, (F) 22.5 KHZ AND (G) 25 KHZ.....	85
FIGURE 3.36 EXPERIMENTAL RESULTS: MFC4 TOP ACQUIRED SIGNAL USING SINGLE MFC ACTUATION AT (A) 10 KHZ, (B) 12.5 KHZ, (C) 15 KHZ, (D) 17.5 KHZ, (E) 20 KHZ, (F) 22.5 KHZ AND (G) 25 KHZ.....	88
FIGURE 3.37 MFC – TIMBER IMPEDANCE MATCHING EXPERIMENT. ....	89
FIGURE 3.38 ACQUIRED SIGNALS FROM THE PZTS AFTER ACTUATING EACH SUBSEQUENT MFC AT 12.5KHZ.....	90
FIGURE 3.39 PRESENCE OF KNOT BETWEEN MFC1 R3 AND PZT R3.....	91
FIGURE 3.40 EXPERIMENTAL RESULTS: ACQUIRED SIGNALS FROM MFC3 TOP SENSOR USING SINGLE MFC ACTUATION FOR A (A) 5-CYCLE AND (B) 10- CYCLE TONE BURST AT 12.5 KHZ.....	93



FIGURE 3.41 EXPERIMENTAL RESULTS: ACQUIRED SIGNALS FROM MFC3 TOP SENSOR USING SINGLE MFC ACTUATION FOR A (A) 5-CYCLE AND (B) 10-CYCLE TONE BURST AT 15 KHZ.....	94
FIGURE 3.42 RAW NUMERICAL DATA COLLECTED USING MFC4 SENSOR FOR (A) SINGLE, (B) 4-RING AND (C) 8-RING ACTUATION AT 12.5KHZ FREQUENCY.....	96
FIGURE 3.43 SURFACE X-VELOCITY COMPONENT FOR AT DIFFERENT TIMES FOR (A) SINGLE, (B) 4-RING AND (C) 8-RING MFC ACTUATION IN COMSOL.....	97
FIGURE 3.44 RAW EXPERIMENTAL DATA COLLECTED USING MFC4 SENSOR FOR (A) SINGLE, (B) 4-RING AND (C) 8-RING ACTUATION AT 12.5KHZ FREQUENCY.....	98
FIGURE 3.45 ANALYSIS FOR THE COLLECTED DATA FROM MFC 4 SENSOR AT 12.5 KHZ FOR (A) SINGLE, (B) 4-RING AND (C) 8-RING MFC ACTUATION IN THE EXPERIMENTAL SETUP.....	99
FIGURE 3.46 ACQUIRED SIGNALS (NORMALIZED) FOR TRACTION FREE/EMBEDDED SOUND TIMBER, SINGLE MFC ACTUATION AT 12.5 KHZ IN (A) NUMERICAL MODEL AND (B) EXPERIMENTAL SETUP.....	102
FIGURE 3.47 NUMERICAL RESULTS: TRACTION FREE (SOLID) AND EMBEDDED (DASHED) USING SINGLE MFC ACTUATION AT 12.5KHZ (A) ORIGINAL SIGNAL AND (B) DECOMPOSED SIGNAL AFTER CEEMD (IMF 1).....	104
FIGURE 3.48 EXPERIMENTAL RESULTS: PROPAGATING WAVE MODES AND THEIR REFLECTIONS– TRACTION FREE/EMBEDDED SIGNALS, USING SINGLE MFC ACTUATION AT 12.5 KHZ.....	106
FIGURE 3.49 NUMERICAL RESULTS: PROPAGATING WAVE MODES AND THEIR REFLECTIONS FOR TRACTION FREE/EMBEDDED SIGNALS USING 4-RING MFC ACTUATION AT 12.5 KHZ.....	107
FIGURE 3.50 EXPERIMENTAL RESULTS: PROPAGATING WAVE MODES AND THEIR REFLECTIONS– TRACTION FREE/EMBEDDED SIGNALS, USING 4-RING MFC ACTUATION AT 12.5 KHZ.....	109

FIGURE 3.51 NUMERICAL RESULTS: PROPAGATING WAVE MODES AND THEIR REFLECTIONS– TRACTION FREE/EMBEDDED SIGNALS USING, 8-RING MFC ACTUATION AT 12.5 KHZ. ....	110
FIGURE 3.52 EXPERIMENTAL RESULTS: PROPAGATING WAVE MODES AND THEIR REFLECTIONS– TRACTION FREE/EMBEDDED SIGNALS, USING 8-RING MFC ACTUATION AT 12.5 KHZ. ....	111
FIGURE 4.1 5.5-METER TIMBER POLE IN COMSOL: (A) ACTUATOR RING AND SENSOR PLACEMENT AND (D) EMBEDDED BOUNDARY CONDITION. ....	116
FIGURE 4.2 DAMAGE INDUCED IN THE TIMBER STRUCTURE FOR (A) TRACTION FREE AND (B) EMBEDDED BOUNDARY CONDITIONS. ....	117
FIGURE 4.3 TOP VIEW SKETCH OF THE TIMBER POLE DISPLAYING EMBEDMENT SOIL, DAMAGE LOCATION AND MFCs. ....	118
FIGURE 4.4 (A) 8-METER TIMBER UTILITY POLE AND (B) MFC ACTUATORS AND SENSOR CONFIGURATION ON THE BOTTOM END OF THE POLE. ....	120
FIGURE 4.5 FLOWCHART OF THE APPROACH UNDERGONE NUMERICALLY AND EXPERIMENTALLY. ....	121
FIGURE 4.6 EXPERIMENTAL SETUP USED ON THE 8-METER LENGTH TIMBER UTILITY POLE. ....	122
FIGURE 4.7 NUMERICAL RESULTS: TRACTION FREE SOUND (SOLID LINE) AND DAMAGED (DASHED LINE) USING SINGLE MFC ACTUATION AT 12.5 KHZ (A) ORIGINAL SIGNAL AND (B) DECOMPOSED SIGNAL AFTER CEEMD (IMF 1). ....	125
FIGURE 4.8 NUMERICAL RESULTS: EMBEDDED SOUND (SOLID LINE) AND DAMAGED (DASHED LINE) USING SINGLE MFC ACTUATION AT 12.5 KHZ (A) ORIGINAL SIGNAL AND (B) DECOMPOSED SIGNAL AFTER CEEMD (IMF 1). ....	126
FIGURE 4.9 EXPERIMENTAL RESULTS: TRACTION FREE SOUND (SOLID LINE) AND DAMAGED (DASHED LINE) USING SINGLE MFC ACTUATION AT 12.5 KHZ. ....	127

FIGURE 4.10 EXPERIMENTAL RESULTS: DECOMPOSED SIGNAL AFTER CEEMD (IMF 2) FOR TRACTION FREE SOUND/DAMAGED USING SINGLE MFC ACTUATION AT 12.5 KHZ. ....	128
FIGURE 4.11 EXPERIMENTAL RESULTS: EMBEDDED SOUND (SOLID LINE) AND DAMAGED (DASHED LINE) USING SINGLE MFC ACTUATION AT 12.5 KHZ. ....	129
FIGURE 4.12 EXPERIMENTAL RESULTS: DECOMPOSED SIGNAL AFTER CEEMD (IMF 2) FOR EMBEDDED SOUND/DAMAGED USING SINGLE MFC ACTUATION AT 12.5 KHZ. ....	129
FIGURE 4.13 NUMERICAL RESULTS: EMBEDDED SOUND (SOLID LINE) AND DAMAGED (DASHED LINE) USING 4 RING MFC ACTUATION AT 12.5 KHZ (A) ORIGINAL SIGNAL AND (B) DECOMPOSED SIGNAL AFTER CEEMD (IMF 1).....	131
FIGURE 4.14 NUMERICAL RESULTS: EMBEDDED SOUND (SOLID LINE) AND DAMAGED (DASHED LINE) USING 8 RING MFC ACTUATION AT 12.5 KHZ (A) ORIGINAL SIGNAL AND (B) DECOMPOSED SIGNAL AFTER CEEMD (IMF 1).....	131
FIGURE 4.15 EXPERIMENTAL RESULTS: DECOMPOSED SIGNAL AFTER CEEMD (IMF 2) FOR EMBEDDED SOUND/DAMAGED USING 4 RING MFC ACTUATION AT 12.5 KHZ. ....	132
FIGURE 4.16 EXPERIMENTAL RESULTS: DECOMPOSED SIGNAL AFTER CEEMD (IMF 2) FOR EMBEDDED SOUND/DAMAGED USING 8 RING MFC ACTUATION AT 12.5 KHZ. ....	133
FIGURE 4.17 TOP VIEW SKETCH OF THE POLE SPECIMEN DISPLAYING THE EMBEDDED AND DAMAGE DISTANCES TO BE ESTIMATED. ....	134

## TABLES

TABLE 2.1 SONIC VS. ULTRASONIC MEASUREMENTS. ....	29
TABLE 2.2 CHARACTERISTICS OF THE THREE MODES IN CYLINDRICAL COMPONENTS [26].....	31
TABLE 3.1 MATERIAL PROPERTIES FOR ORTHOTROPIC TIMBER [31].....	47
TABLE 3.2 MATERIAL PROPERTIES FOR TRANSVERSELY ISOTROPIC TIMBER [31]. ....	48
TABLE 4.1 NUMERICAL RESULTS: BOTTOM EDGE DISTANCE ESTIMATION USING MODE $L(0,1)$ FOR SINGLE, 4-RING AND 8-RING MFC ACTUATION.	136
TABLE 4.2 EXPERIMENTAL RESULTS: BOTTOM EDGE DISTANCE ESTIMATION USING MODE $L(0,1)$ FOR SINGLE, 4-RING AND 8-RING MFC ACTUATION.	137
TABLE 4.3 NUMERICAL RESULTS: DAMAGE LOCALIZATION USING MODE $L(0,1)$ FOR THE SINGLE MFC ACTUATION. ....	138
TABLE 4.4 EXPERIMENTAL RESULTS: DAMAGE LOCALIZATION USING MODE $L(0,1)$ FOR THE SINGLE MFC ACTUATION. ....	138

# Chapter 1 Introduction

## 1.1. Background

The use of timber has commenced thousands of years ago and is still being used today in numerous applications. Being easy to manufacture and customize, practices vary from construction work, transportation applications, equipment and infrastructure. When treated properly, timber can act as a substitute for many renowned materials such as steel and concrete. The cost of manufacturing, transportation and storage is low compared to other materials, in addition to the ability to withstand handling and surface damage due to the lightweight and tough properties [1]. However, there are concerns that must be considered when using timber. Besides being prone to structural damage from carrying loads and connections, wood is subjected to other serious natural decays and damages that require careful assessment. Long-standing in-service timber utility poles need further efforts to prevent them from failure and extend their lifecycle, which could also save millions of dollars on maintenance and replacement costs. Throughout history the evaluation of the interior conditions of timber has always been a challenge, where various have been considered that vary between destructive (D), semi-destructive (SD) and nondestructive (ND). Among all the non-destructive techniques, sonic/ultrasonic stress wave propagation is considered the most common where it can provide sufficient quantitative and qualitative assessment.

The conventional non-destructive technique performed on timber utility poles corresponds of generating low-frequency stress waves. This technique is based on the 1-dimensional wave theory where the waves propagate in bulk form and are independent on

the frequency of excitation. The condition assessment is mainly based on comparing the measured P-wave (bulk wave) velocity ( $V_P$ ) to a reference velocity value for each type of timber. On the other hand, guided stress waves which are based on the 3-dimensional wave theory, could provide more information about the propagation behavior of stress waves for the ND evaluation of timber poles. In this theory, the waves propagate along a certain guideline provided by the geometry of the structure, such as growth rings in timber poles, are dependent on the excitation frequency and are considered highly dispersive. One of the many advantages of guided wave propagation is the ability to control the desired output. For instance, when evaluating the health state of a certain structure, modifications to the experiment can allow the determination of desired defect sizes [2]. One of these modifications can be the wavelength, which is dependent on the excitation frequency and velocity of the propagating wave modes. Guided wave (GW) propagation is not yet common in structures that have complex shape and properties such as timber. Their orthotropic nature forces several challenges for the assessment, in addition to the geometry, where the actual 3-D wave equation becomes difficult to solve and phenomena such as dispersion, attenuation and distortion appear to pose great difficulty when analyzing the results [2].

## **1.2. Timber Poles – Applications**

Wooden poles were one of the first primary tools used by ancient people. Being easy to manufacture and customize, practices started growing and varied between construction work, transportation applications, and equipment. There are important reasons

why wooden poles are still being used today in different applications. When treated properly, wood can act as a substitute for many renowned materials such as steel and concrete. The cost of transportation and storage nowadays is low compared to other materials, in addition to the ability to withstand handling and surface damage due to wood's lightweight and tough properties. Also, the machinability of wood is flexible and can accommodate to various requirements which eventually widens its applications.

One of the most famous current applications of timber is utility poles. These poles support overhead power lines, electrical cables and other utility equipment. The advantage of using wood instead of steel or aluminum poles is the electrical conductivity where wood is a perfect insulator. Embedding wooden poles into the ground is easier than other materials [3], in addition to higher efficiency when installing utility accessories and additions.

Besides utility poles, the oldest and most common application of timber poles is in the construction industry. As mentioned earlier, wood is easy to manufacture and customize along with a long service life of 40 to 80 years depending on the climate conditions. The most important feature is that it can be removed and reused for other purposes with low treatment cost and time.

To maintain the health of timber poles and ensure their safety and reliability in any application, evaluation practices must be conducted to determine whether damage has occurred during the life cycle. In addition to damages, natural defects and decays can occur which might affect the overall strength of the pole and must be appropriately treated.



*Figure 1.1 Timber utility poles.*

### **1.3. Decays and Defects in Timber**

Damages can arise in timber during its life cycle in a certain application. However, during the process of converting timber from natural to commercial form, several defects might occur. The most common production defects are the following [4]:

- Chip marks created by chip on finished surface of the timber.
- Diagonal grain due to improper sawing of timber.
- Torn grain created by tool along cross section.
- Wane due to presence of additional rounded surface on manufactured timber.

These defects vary according to the quality and accuracy of the machinery, where they can be reduced and manipulated carefully. On the other hand, natural decays present a more serious concern since they could greatly affect the overall health. One of the most common decays in wood are due to Fungi. The initial process of decay due to living fungi starts by the deposition of spores. These spores can distribute rapidly by wind, water or insects, and are able to penetrate the timber in a short period of time [4]. Certain conditions must be present for the fungi to grow that include the presence of sufficient oxygen, a favorable temperature range, sufficient food supply (wood) and moisture which is the most important condition. All these requirements must meet in order for the fungi to grow. With respect to the type of fungi present, not all species cause decay in wood. Types like molds, stains, spots, patches and soft rot do not cause any damage. However, there are types of fungi that seriously damage and weaken wood such as brown and white rot. Brown rot degrades the cellulose leaving the lignin as framework which turns wood into brown and crumbly as shown in Figure 1.2 (a). On the other hand, white rot feeds on the cellulose,



hemi-cellulose and lignin which makes the wood white and stringy [4] as shown in Figure 1.2 (b).



Figure 1.2 (a) Brown and (b) white rots in wooden poles.

Brown and white rots are the most common type of decays that cause structural damage to wood and must be treated carefully. The natural resistance to decay is quite vulnerable and depends on certain conditions that are variable most of the time. Another main type of decay that occurs in wood is due to insects. Insects are considered a major threat for wooden species since they can tunnel in and empty the inside of the members for food and shelter [4]. The most common types of insects that lead to decay are shown in include termites, carpenter ants, powder-post beetles (*Lyctus*) and caddis flies. Termites are pale-colored, soft insects that rapidly feed on food. The dangerous feature of termites is that they feed from the inside of the timber and thus the damage is not directly visible. The only visible marks are the white mud runways extending from the ground. Carpenter ants are large, black ants that eat off galleries in softwood. The ants do not use the wood for food; instead they build their galleries in the moist/soft areas of the decayed wood. An indicator for their presence is the accumulation sawdust on the ground at the base of the timber

structure. Another type of insects that hollow the timber structure are Powder-post or Lyctus Beetles. These insects leave the outer surface pockmarked with small holes and a powdery dust as a trace where they seek food and shelter from the inside of the timber. Bacterial and fungal decay attract another type of insects known as Caddis Flies that can also damage timber poles. These insects are aquatic and closely related to moths and butterflies. They can dig small holes in wood during the larva and pupa stages where they do not feed on timber, but they use it as a foundation for their shelters [4].

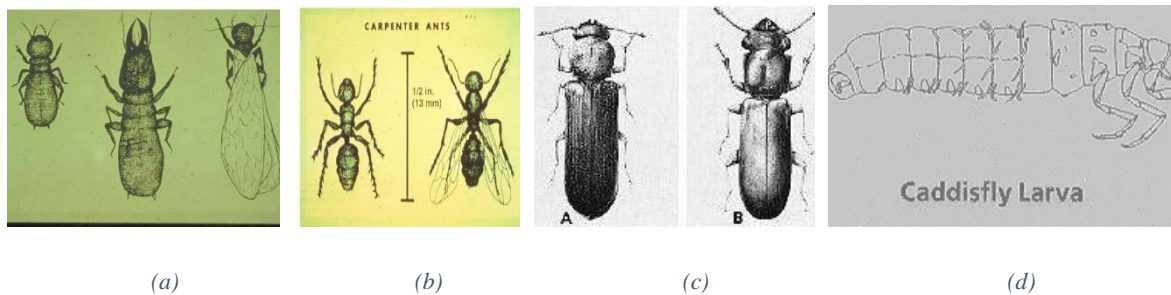


Figure 1.3 Various types of insects affecting wood: (a) Termites, (b) Carpenter ants, (c) Lyctus beetles and (d) Caddis flies.

Figure 1.4 shows the decays formed from the different insects that might live on timber structures, where it is shown how severe the damages can get which could significantly affect the overall health of the structure.



*Figure 1.4 Decays in wood caused by insects.*

## Chapter 2 Literature Review

### 2.1. Overview

Methods for the evaluation of wooden structures and poles have been frequently developing over the past years. Various non-destructive (ND) techniques were established to evaluate the conditions of wood while preserving the integrity of the structure. Among the various non-destructive techniques for the evaluation of timber (such as radioscapy, vibration methods, probing and sounding), sonic/ultrasonic stress wave propagation are considered the most common. They can provide sufficient quantitative and qualitative assessment of the health state of the structure. The conventional method for generating low frequency stress waves occurs by striking one end of the specimen by an instrumented hammer [5]. On the other end of the specimen another sensor is mounted that receives the propagating stress wave. From the known distance between the devices (input and output) the velocity of the stress wave can be calculated which is known as bulk wave. The timber specimen can be evaluated by studying the variation of bulk wave velocity compared to a reference velocity for sound specimens. This technique was discussed by Dackermann et al. where they explained the basic principles of the 1-dimensional (1-D) stress wave technique [5]. On the other hand, Subhani [2] mentioned that the 1-dimensional wave theory does not provide enough information about the actual propagation behavior of stress waves. For instance, the effect of surrounding medium on wave attenuation is not considered in the 1-D theory, where the effect of soil embedment is important for analyzing the results. Also, the 1-D theory interprets the results obtained from impact echo/impulse response tests that are limited to low frequencies [6], which forces some constraints when detecting damages

in the structure. Additionally, embedded length estimation using 1-D stress waves requires the velocity to be known initially (bulk velocity), which is not the case as Subhani [2] mentioned where the velocity is actually unknown and dependent on the frequency of excitation (dispersive). Therefore, the use of the 3-dimension wave theory could provide more information about the propagation behavior of stress waves for the non-destructive evaluation of timber poles. Guided wave propagation is not yet common in structures that have complex nature and properties such as timber. The orthotropic behavior in timber forces several challenges for the assessment. In addition to the geometry, where the actual 3-D wave equation becomes difficult to solve and phenomena such as dispersion, attenuation and distortion appear to pose great difficulty when analyzing results [2].

Guided wave propagation has been used for structural health monitoring (SHM) of various components with different geometries. Modeling the mechanical wave propagation in circular structures was first introduced by J. Pochhammer and C. Chree during the 1800s where they explained how to treat the basic wave equation in cylindrical components such as steel pipes [7]. After being able to identify the solution of the wave equation, the behavior of waves began to be understood widely and used for the assessment of the internal conditions. In 1959, Gazis [8] stated the first official/exact solutions to the Pochhammer-Chree frequency equation. Also, Seco and Jimenez [7] modeled, in 2012, the generation and propagation of ultrasonic signals in cylindrical guidelines and expanded the results obtained by Rose [9] in the year 2000. Seco and Jimenez [7] re-identified the different types of waves that are present in cylindrical components and created a computer program that can solve the wave equation and plot dispersion curves for any excitation frequency.

In orthotropic material, guided wave propagation exhibits different characteristics compared to isotropic material where the properties vary with orientation [7]. Timber has a very complicated internal structure and is considered highly dispersive. The solutions of the wave equation are not available yet for orthotropic cylinders. Therefore, simplifications to the model can be applied where wood can be considered as transversely isotropic. A comparison between modeling isotropic and transversely isotropic wood was conducted by Subhani and Li [10] that highlight the importance of considering timber as an anisotropic medium for guided wave propagation. In addition, Subhani et al. [11] conducted several studies on the dispersive nature and behavior of guided waves in timber poles. The authors depicted analytically the effect of modulus and Poisson's ratio on guided waves dispersion in transversely isotropic timber. In 2014, Subhani et al. [2] presented a complete study on guided wave propagation in cylindrical structures and particularly in utility poles where the authors emphasized once again on the importance of modeling timber as a transversely isotropic material and compared them to isotropic models. The authors noted that the isotropic analysis on timber is important for examining some parametric studies such as the effect of temperature and humidity on the dispersion behavior. Subhani et al. [12] also demonstrated methods for reducing dispersion effects by analyzing energy velocity curves, normalized displacement and the input signal. For instance, the effect of the input signal on the dispersive behavior of both flexural and longitudinal wave modes was studied, where several cycles were tested and compared. Also, Subhani et al. [12] discussed how dispersion and multi-modes can be reduced by creating certain actuator/sensor array configurations around the circumference of the pole.

Numerical investigations on guided waves in timber poles have been conducted by Subhani et al. [13] using the spectral finite element method to determine the embedment length of the pile which was also conducted experimentally. The system was modelled considering partial embedment of the pole in soil, where the timber exhibits an orthotropic behavior. The embedded condition was modeled by a spring-dashpot system where it represented the soil behavior in such conditions. Subhani et al. [14] discussed the effect of soil in energy leakage, wave attenuation and wave velocity. The authors mentioned that the GW theory has not yet been developed for partial embedment, but rather for traction free or fully embedded conditions, which makes understanding the effect of soil challenging. However, they stated that the velocity of the waves is only affected at low frequencies (below 2 kHz), and that attenuation becomes the main feature affected by the soil embedment. Additionally, numerical investigations on guided wave propagation in embedded timber utility poles using finite element method (FEM) and parametric sensitivity analysis were investigated by Yu [15]. Two different finite element methods to simulate the timber – soil interaction and the effects they have on guided wave propagation were presented. The parametric sensitivity analysis was performed to study the relationship between guided wave behavior, excitation location and material properties of the timber specimen. Further, Yan et. al. depicted numerically and experimentally the influence of soil on stress wave propagation in timber utility poles [16].

## **2.2. Condition Assessment Using Guided Waves**

When evaluating the integrity of timber utility poles, two parameters are mainly examined and correspond of the embedded length of the pole and the presence (position) of a damage or decay in the embedded section [8]. Currently, surface non-destructive techniques are the most common in timber structures where longitudinal (compressional) and flexural (bending) stress waves are used for the evaluation process. These techniques include sonic echo (SE) and impulse response (IR) tests, where the embedded length and health state of the timber can be evaluated. The main concept behind the sonic echo method is the travel time measurement of propagating stress waves. In the impulse response method, spectral analysis is performed in the frequency domain for the evaluation process. In both methods, longitudinal and flexural waves are induced by an impact hammer and measured at a specific location along the timber pole. The time of flight of the wave in SE, and the distance between the peaks in the velocity-frequency function in IR, can be used to estimate the embedment depth of the pole. The variation in acoustic impedance can also provide information about the presence of a decay in the structure [8].

Numerical investigations on guided waves in timber poles has been conducted by Subhani et al. using the spectral finite element method to determine the embedment length of the pile which was also validated experimentally [11]. The system was modelled considering partial embedment of the pole in soil, where the timber exhibits an orthotropic behavior. The embedded condition was modeled by a spring-dashpot system to account for the presence of soil. The determination of embedment length experimentally was also performed by Li et al. using wavelet transform [12]. The method applied – Continuous



Wavelet Transform CWT – was proven to work efficiently in processing acquired signals and identifying reflected wave packets considering complex situations such as impact location and the presence of abnormalities in the structure. CWT was also used for embedded length determination using flexural waves in [13], where it was compared to the SKM (short kernel method). CWT proved to be more consistent and straightforward than SKM, leading to 9-17% error compared to 9-23% in SKM when determining the embedded length of the timber pole.

Condition assessment of timber poles can be performed using guided waves where the presence of decay or damage can be detected. Various studies on this matter have been conducted with the use of machine learning techniques. Dackermann et al. [14] used support vector machines (SVM) on a network of tactile transducers that generate guided waves in timber poles. Different damage cases were conducted on several timber and concrete pole specimens where the SVM was used to generate classification results for predicting damage conditions. Other signal processing techniques such as fast Fourier transform (FFT) and principal component analysis (PCA) were also used to process data from damaged specimens. In another study, Dackermann et al. [15] presented machine learning methods for pattern recognition to assess the health condition of timber poles. Guided waves were actuated and captured using a multi-sensor array mounted on the pole. Damage detection using a hierarchical data fusion algorithm was applied on timber poles in [16] with the use of guided waves. Multi-sensor arrays were also used in the model where the hierarchical approach lead to an enhanced accuracy when detecting damages in the timber pole.

## **2.3. Timber Poles Evaluation – Different Practices**

Like any other element, timber can be prone to degradations and defects depending on the application. The overall strength of the structure can be affected in addition to the formation of decays from the inside. Therefore, it is crucial to monitor timber structures where a variety of different ND methods can be used to assess changes that might be occurring. These advanced methods are discussed below.

### **2.3.1. Visual Inspection**

One of the simplest and first ND methods to be used when assessing timber structures is the visual inspection method. Easy-to-detect deficiencies and degradations can be noted out using this method, which include external damages, creep, decay, splits, etc. [17]. Internal deterioration is often hidden beneath the surface of the structure; however, although probing the wood using sharp picks is a bit unpleasant, it enables rapid detection of voids and early stages of decay that are not visible on the surface [18]. Nevertheless, removal of small samples from the wood structure is important for identifying the wood species. This identification is crucial for further stages and methods of inspection because it provides important information regarding the internal structure of the wood, such as the propagation and orientation of its growth rings.

### **2.3.2. Resistance Drilling**

Determination of density and the location and extent of voids can be determined using this method [17], [18]. Drill resistance is a quasi-nondestructive test because of the

small diameter, needle-like hole that remains in the specimen after testing. This hole has negligible effects on the structure of the wood and can be sealed after testing [17].

Variation in the drilling resistance can indicate the presence and location of internal defects.

As the small diameter drill is inserted in the structure, a plot of drilling resistance versus position is created where the determination of defects and voids along with their position becomes relatively easy.

### **2.3.3. Radioscopy**

Radioscopy involves radiation (X-rays) from a radiographic energy source through the section of the element to a recording medium such as film on the other side. From the amount of radiation that passes through the object, accurate measurements of the density can be found. The object can be radiographed from different orientations thus creating a three-dimensional image of the object. This is known as Computed Tomography [17]. Also, X-rays are used to study wood degradation due to fungal attack.

### **2.3.4. Microwave/Ground Penetrating Radar**

Microwave wave inspection methods are based on the propagation of electromagnetic waves from antennas or probes at frequencies that range from 300 MHz to 300 GHz [17]. Two kinds of wave transmission can be employed. The first type includes two probes, an emitter and receiver of the electromagnetic waves. The second type (known as ground-penetrating radar) includes only one probe or antenna which acts as both the emitter and receiver (energy is reflected from a surface). This method is most commonly

used for the determination of the density of wood specimens and can be used along with stress wave methods.

### **2.3.5. Vibration Methods**

This nondestructive technique is beneficial for determining the modulus of elasticity (MOE) of timber specimens. Vibrational analysis can be done on a single member where the elasticity can be measured, along with detection of damages [17]. However, vibratory motion for damage detection has only been applied on metallic beams but may also be applied on timber beams. Mode shapes are recorded for the tested specimens and the extent of damage can be determined.

## **2.4. One-dimensional (1D) Wave Theory**

The most common technique for the evaluation of timber specimens is using sonic or ultrasonic stress waves. The conventional method for generating a low frequency stress or sound wave is by striking one end of the tested specimen by either a normal or instrumented hammer. Upon striking the hammer, a start signal enables a timer. On the other end of the specimen another sensor is mounted directly opposite to the impact sensor that receives the propagating stress wave and sends a stop signal to the timer [5]. From the known distance between the sensors and the measured time of propagation of the stress wave, the velocity of the stress wave can be calculated. The velocity of propagation of stress waves in timber varies relative to several reasons. For instance, sound wood for a certain species has a known stress wave velocity (bulk velocity) and can be used as a

reference to compare and test other specimens for defects. If a defect or decay exists, the velocity of the wave becomes different than the reference velocity and observation/analysis of the waves become very crucial.

Ultrasonic stress waves are high frequency (>20,000 Hz) waves that are above the audible range. The same concept of the conventional stress wave method is used where the wave propagates through the timber structure and the TOF is measured [5]. Stress waves measurements are used for screening the condition of the wood structure and to estimate the modulus of elasticity (MOE) [18]. Defects such as knots, decay in wood members, and slope of grains can be detected using this method [17]. On the other hand, conventional ultrasonic inspection of wood can have several drawbacks and difficulties that include the dependence of the one-dimensional wave theory which might lead to accurate evaluation, effective ultrasonic coupling between transducers and the wood surface and limitations on structural dimensions. [17]. Further discussion of this method is listed in the subsequent section.

Several non-destructive techniques are based on the one-dimensional wave theory which is based on kinematics of deformation. Waves are described as plane waves in a string with an infinite space of propagation, where the solution to the wave equation does not consider Poisson's effect (lateral deformation) [2]. The wave behavior is solely dependent on the initial conditions, where the boundary conditions can affect the wave's amplitude only and not the wave's velocity. A wave propagating in the x-direction has the following displacement equation:

$$\frac{\partial^2 u}{\partial t^2} = C^2 \frac{\partial^2 u}{\partial x^2}$$

Where  $u$  is the displacement and  $C$  is the wave velocity [19]. In this system, the wave velocity is considered constant through the whole media and can be defined from the above equation by bulk longitudinal ( $C_l$ ) and bulk shear ( $C_s$ ) velocities as follows:

$$C_l = \sqrt{\frac{E}{\rho}} \quad \text{and} \quad C_s = \sqrt{\frac{G}{\rho}}$$

Where  $E$  is young's modulus of elasticity,  $G$  is the shear modulus, and  $\rho$  is the mass density of the structure. Another assumption that uses the 1D wave theory is the flexural or bending wave propagation, which has good accuracy in low frequency domains [2]. Pure bending is considered due to Bernoulli-Euler beam theory, where motion in the vertical direction for a homogeneous media becomes as follows:

$$\frac{\partial^4 y}{\partial x^4} + \frac{\rho A}{EI} \frac{\partial^2 y}{\partial t^2} = 0$$

Where  $E$  is the young's modulus of elasticity,  $A$  is the cross-sectional area and  $I$  is the moment of inertia [20]. The flexural wave velocity from the above equation can be seen to increase as the wave frequency increases and is described as follows:

$$C_f = \sqrt{a\omega} \quad \text{and} \quad a = \sqrt{\frac{EI}{\rho A}}$$

Where  $\omega$  is the angular frequency.

#### **2.4.1. 1-D Wave Theory Based Non-destructive Testing**

As mentioned earlier, several NDT are based on stress waves propagation for damage detection and structural assessment. The generated waves vary with the geometry of the structure used. For instance, when working with timber with circular cross sections,

three types of waves can be generated that include torsional, flexural and longitudinal stress waves. The most common types generated are the flexural and longitudinal stress waves which are the easiest to generate and control [2]. This generation can be controlled by the impact location on the structure. If the top cross-sectional area of the pole is impacted, then longitudinal stress waves are generated. However, flexural stress waves are generated when the side section of the pole is impacted.

When evaluating the integrity of a structure using stress waves, two parameters are mainly determined that are the length (could be the embedded length of the wooden pole) and the position of the damage or decay [2]. For surface non-destructive techniques which are the most common, different types of tests can be carried that can either generate longitudinal (compressional) or flexural (bending) stress waves. Sonic Echo (SE) and Impulse Response (IR) tests are used for the evaluation of timber poles and for estimated the embedded length. As mentioned by Subhani [2], these methods can also detect defects, soil inclusions, necking, and diameter bubbling. The main concept behind the Sonic Echo method is the travel time measurement of propagating stress waves. The Impulse Response method use spectral analysis for interpretation in the frequency domain [2]. In both methods (SE/IR), longitudinal wave reflections are measured where the stress waves are induced by an impulse hammer that travels across the pole until it experiences a change in acoustic impedance. This is where the wave is reflected back to a sensor/receiver and the time of flight of the wave is measured. The depth of a foundation can be estimated from the SE data by measuring the time difference between two reflection events as shown in the equation below [2]:

$$L = C_l \frac{\Delta t}{2}$$

Where  $L$  is the reflector depth and  $C_l$  is the longitudinal wave velocity. As for the IR tests, the data extracted can be used to estimate depth from the following equation:

$$L = \frac{C_l}{2\Delta f}$$

Where  $\Delta f$  is the distance between two peaks from the velocity-frequency function. In both methods (SE/IR) that rely on the one-dimensional stress wave theory, the velocity is assumed to be constant without any variation across the length of pole and is used to calculate the length. A complete study and experimental procedure by Dackermann [2] are presented in the next section that rely on the time-of-flight method for the evaluation of timber poles.

#### **2.4.2. In-situ Assessment of Timber Poles – Ultrasonic Stress Waves**

Ultrasonic stress waves are useful to determine properties of a certain element, and by measuring the time-of-flight (TOF) additional information regarding decays and degradations can be provided along with the length estimation of the structure. In this section, basic principles of this ND method are discussed along with different assessment procedures, equipment and application on timber structures.

##### **a) Basic Principles**

Creating stress waves in timber structures by exciting a sensor on one end of the structure can provide crucial information relative to the interior state of the timber. Stress



waves propagate through the cross-section (or any other orientation depends on the position of the sensor) where the velocity of the wave is determined. In general, there is a reference stress wave velocity for each specific type of sound wood. This reference can be compared with measured velocities (in situ) to determine whether voids or defects are present. Stress waves propagate rapidly in dense, solid materials such as perfectly sound wood, while voids or cracks however divert stress waves and thus lead to a longer time of propagation[5]. The propagation of stress waves in timber is affected by various conditions such as the type of species, moisture content and the orientation of growth rings relative to the orientation of the impact [5]. When one end is excited, a stress wave is generated across the whole section where the sensor is mounted. Longitudinal stress waves are generated when the wave passes through the whole length of the timber specimen. The transverse waves whatsoever are generated when the wave passes across the cross section of the specimen. When measuring stress waves to assess a timber structure with a certain cross section, important parameters can affect the wave's propagation and must be taken into consideration. In order to avoid anisotropy in transmission of the waves, one should find the appropriate orientation of the stress waves and thus determine how to mount the sensors on the structure accordingly. For instance, in case of transverse measurements on circular or rectangular timber cross sections where the growth rings are known and diagonally oriented, sensor's placement should occur all around the circumference to create a good acquisition scheme. However, if the growth rings position is unknown, sensors should be placed on opposite sides of the cross section only [21]. On the other hand, in case of longitudinal measurements one should avoid wave-transmission along the fibers instead of across the fibers, and thus the maximal inclination theory of the linear path of the wave

should be considered [22]. Velocities can be monitored and measured from an oscilloscope where the signals should be properly filtered [23]. Cross-sectional imaging of timber structures can be created using ultrasonic tomography. Sensors placed at different positions along the circular cross-section of the specimen (Figure 2.1) measure the TOF and from the distance between the sensors, velocities can be calculated and thus images of the velocity distribution along the specimen's section can be created [5]. After creating the velocity profile of the cross section, various processing and interpretation techniques can be applied to build a well-suited tomographic report.



Figure 2.1 Sensor placement around the cross section of a specimen [5].

## b) Quantitative & Qualitative Assessment

Evaluation of measured stress wave velocities is related to the amount of decay present between the two sensors through the relative difference between measured and reference velocity [5]. The relative decrease of stress wave velocity is determined by:

$$\Delta V_{relative} = \frac{V_{ref} - V_{mes}}{V_{ref}} \times 100$$

The relationship between the relative velocity decrease and the area of decay (in %) are found in tabulated forms and can be used to evaluate the decrease in the overall strength of the timber structure. Nevertheless, stress wave measurements can be used to estimate the dynamic modulus of elasticity ( $MOE_d$ ) and can be derived from the one-dimensional wave theory [5]:

$$MOE_d = V^2 \rho$$

Where V is the velocity of the propagating stress wave and  $\rho$  is the mass density of the timber structure. The mass density of a certain specimen can be estimated by taking multiple samples from the specimen and performing resistance drilling on them. Several methods of in situ assessment of timber structures can be applied before performing stress waves measurements. Assessment of material and mechanical properties, timber density, stiffness and stress wave timing can be performed for a complete evaluation of the structure's conditions.

### c) **In-situ Pre-Assessment**

Important parameters must be determined before proceeding with any kind of timber evaluation. In our project, ultrasonic stress wave assessment on timber requires different inputs, where we will call them pre-assessed parameters. For instance, in order to determine the dynamic modulus of elasticity ( $MOE_d$ ), one has to find the density of the specimen where the mechanical performance can also be directly related. Portable X-ray techniques are available in order to determine the density, as well as to assess the internal

conditions of the specimen to a certain extent [24]. Mechanical properties are also crucial for the assessment of timber where the ductility, hardness and strength can be evaluated using NDT that will be mentioned in this section.

**d) Radiographic Imaging – Wood Density & Mechanical Properties**

One of the most efficient and appropriate methods of evaluating the in-situ density of wood is the density calibration procedure using X-ray equipment. The determination of the elastic modulus highly depends on the speed of propagation of the stress wave but is also dependent on the density of the material and the moisture content present. That is why the accuracy of assessing the mechanical properties of a material depends on the accuracy of measuring the pre-assessed parameters such as the density. Additional analysis can be applied using semi-destructive techniques – such as resistance drilling – to verify the obtained density value but depends on each case of study.

Quantitative assessment of different components can be done by the application of digital imaging processing (digital radiography or X-ray). The short-wavelength rays can be used to determine important characteristics of the structure. For example, the penetration of an X-ray is the intensity projection on the image plate, and is affected by the following [24]:

- Type of material & material characteristics
- Material composition
- Density of the material
- Porosity of the material & it's moisture inclusion

- Attenuation factor ( $\mu$ )
- Penetration thickness of the X-rayed object

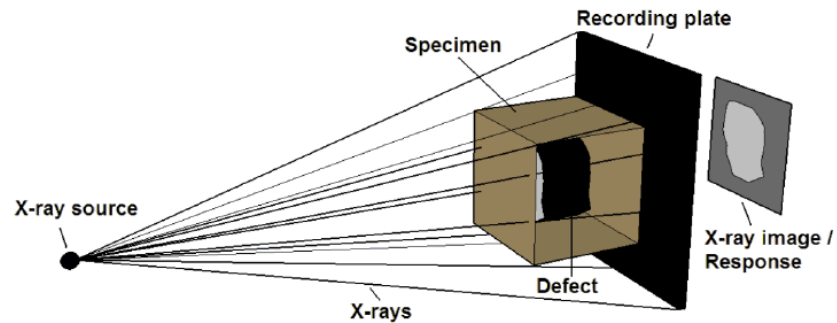


Figure 2.2 X-ray configuration on fixed specimens.

The obtained image can be sorted in a matrix formed and processed in MATLAB's image processing toolbox or LABVIEW's vision & image processing unit. The below schematic shows the concept of radiographic imaging on fixed components. Since wood is a highly anisotropic material, its characteristics vary between different directions (longitudinal, transverse, radial, etc.) and mainly depend on the wood species, moisture content, natural growth defects and the type of structure [24]. The static elastic modulus (MOE)<sub>s</sub> can be estimated from the dynamic elastic modulus (MOE)<sub>d</sub> discussed earlier using specific correlations that depend on the material itself.

#### e) **Assessment of Decays using Stress Wave Timing**

Velocity profiles help indicate the presence of decays and defects in timber structures, however in order to properly understand these profiles, decays should be

investigated properly. One should understand the reason why stress waves get affected by decays, and how does the geometric orientation of a defect or decay affect the measurement as well. A guide for the assessment of decays in standing trees and timber structures is available for complete analysis and information on velocity measurements, commercial equipment and usage, references and considerations, and tomographic imaging [22], [24].

A 2-d tomogram can be created from the velocities calculated by the sensors mounted on the specimen where colored lines indicated stress waves' speeds and are used to reconstruct and display internal conditions [5]. Figure 2.3 shows a 2-d tomogram of a timber specimen where red lines are an indication of unusual stress wave velocities that might indicate deteriorations, and green lines indicate sound velocities (normal) and intact internal areas.

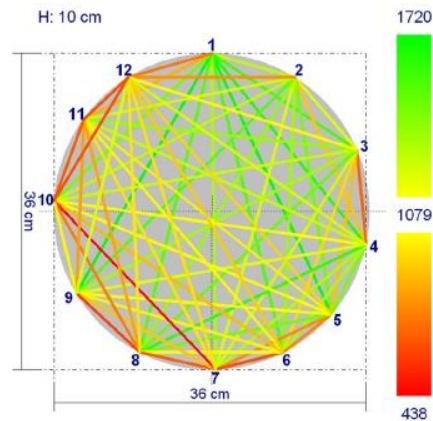


Figure 2.3 Two-dimensional tomogram of a timber post [5].

The velocity distribution over square pixels (tomography) depends on the geometric arrangement of the sensors mounted. The minimum size of detectable decays or

defects strongly depends on the frequency used and resolution of the tomography [5]. This resolution is determined as:

$$\text{Resolution } R = \left( \frac{d \times V}{4f} \right)^{\frac{1}{2}}$$

Where  $d$  is the distance between transmitting and receiving point,  $V$  is the velocity and  $f$  is the signal dominant frequency. Shorter wavelengths allow the determination of smaller features, however there is a limit for short wavelengths that should be taken into account. Therefore, one should determine a compromise between resolution and attenuation by choosing an appropriate frequency [23]. Proper analysis should be applied on the acquired signal and the signal-to-noise ratio at a later stage. An assumption that stress waves propagate in a linear straight direction (or in bent rays) is taken when constructing 2-d tomograms. Iterative inversion algorithms and direct inversion algorithms can be also used for tomographic reconstruction. Several software are available for the construction of these graphs, and some of them are specifically available for timber structures and trees [5]. For interpretation of results, different analysis techniques can be applied to tomograms such as image processing and histogram equalization techniques, which can highlight heterogeneities and adjust the image's global contrast. Good approximation of tight knots' position and direction can be estimated using this method. However, this technique is only qualitative, and does not provide quantitative assessment for the internal structure and state of the inspected specimens. Coupling with other techniques is very useful for estimating properties of the inspected element, such as resistance drilling. On the other hand, ultrasonic tomography can be adopted as a large scale global evaluation method for decay detection and assessment, to be followed by further investigation in specific areas [5].

A series of connected sensors attached across the cross-section of the timber specimen can create a 2-D tomography as mentioned earlier. The number of sensors attached is limited to the diameter size of the specimen and does not have a certain rule for placement. The equipment required for stress wave TOF measurements consists of the following [5]:

- Oscilloscope (visualization & data analysis)
- Function generator, with a given pulse repetition frequency
- Timer, which controls both the trigger of the generator and the counter
- Signal amplifier
- Signal filter
- Piezoelectric transducers for emitting high frequency signals (50 – 100 kHz)
- Piezoelectric transducers for receiving signals
- Preamplifiers which are required in most applications on wood, because of the high attenuation of the transmitted waves in the material, especially in the case of thick elements
- Multi-channel device to speed up measurements for tomographic data acquisition

The following table presents a brief comparison between Ultrasonic and Sonic time-of-flight measurement methods. The decision between choosing one of the methods is based on the size of the timber specimen to be tested, and the defect size of interest.



<b>Sonic Measurements</b>	<b>Ultrasonic Measurements</b>
Low frequency stress waves (audible)	High frequency stress waves (>20kHz)
Can travel large distances (large wavelength)	Can travel short distances (short wavelength)
Better determination of average material properties	Greater ability to detect smaller voids and defects
Suitable for timber depth > 89 mm	Suitable for small size timber specimens

*Table 2.1 Sonic vs. ultrasonic Measurements.*

### **2.4.3. Limitations of One-Dimensional Stress Wave Based NDT**

Non-destructive techniques based on the one-dimensional stress wave theory might not provide sufficient information regarding the integrity of the structure tested. As mentioned earlier, the 1D theory considers wave propagation in an infinite media without any boundary conditions. Therefore, the velocity of the wave becomes constant across the pole and can be used to estimate the length or embedded length. As mentioned by Wang [25], at low frequencies the longitudinal wave velocity and attenuation is almost constant for poles with large diameters, which makes the tests that use this theory accurate to a certain extent. As for tests based on the bending wave theory, flexural waves in nature are highly dispersive where the velocity increases with frequency increase which limits the practice of this method to low frequency ranges only.

Surface non-destructive testing methods cannot be used as a precise indicator for the evaluation of a certain structure due to the lack of understanding of the actual wave behavior. However, in the case of the guided wave theory boundary conditions are present for solving the wave equation where the velocity of the wave becomes a function of the

frequency of excitation. As well as the displacement function which varies as the wave propagates through the pole [2]. This provides a better understanding of how the wave is propagating, where the evaluation process becomes much more accurate and precise.

## 2.5. Three-dimensional (3D) Guided Wave Theory in Cylindrical Structures

The Pochhammer-Chree theory provides a numerical solution to the behavior of cylindrical waveguides, in addition to tracing the frequency-wavenumber curves, mode shapes, and modal analysis [26]. Determining the propagating wave modes from dispersion curves (frequency-wavenumber curves) and studying mode shapes is crucial for the assessment of the overall health condition of a structure. Therefore, every structure must be modeled and solved numerically to account for the shape/geometry and boundary conditions to achieve an accurate solution.

In the case of timber poles with circular cross section, the wave equation must be solved considering two main properties, circumferential guided waves (cylindrical) and guided waves in anisotropic media. In literature, wave propagation solution in anisotropic media is divided into solid and hollow cylinders. Research on hollow cylinders such as pipes and shafts is more common than solid and multilayered ones. However, the solutions of the wave equation in any cylindrical material are directly found using potentials and separation of variables, resulting in the general form of the displacement vector ( $u$ ) and stress tensor ( $\sigma$ ) described as the following [26]:

$$u(r, \theta, z) = u'(r, \theta)e^{jkz} = u(r)e^{jm\theta}e^{jkz} \quad \sigma(r, \theta, z) = \sigma'(r, \theta)e^{jkz} = \sigma(r)e^{jm\theta}e^{jkz}$$

where,

- $(r, \theta, z)$  are the polar coordinates of the cylinder.
- $(e_r, e_\theta, e_z)$  are the unit vectors.
- $e^{-j\omega t}$  is the harmonic time variation.
- $k$  is the wavenumber.

The solution of the wave equation is classified in a family of modes according their symmetry properties [26] and are divided into Torsional modes T(n,m), Longitudinal modes L(n,m) and Flexural modes F(n,m) where n is the circumferential order (0 for torsional and longitudinal,  $\geq 1$  for flexural modes) and m is the second index used to order them. The following table summarizes the three major modes in cylindrical structures with their displacement components.

Mode	Coefficient	Displacement Component	Stress Component
<i>Torsional</i>	$SH_{\pm}$	$u_{\theta}$	$\sigma_{\theta z}, \sigma_{r\theta}$
<i>Longitudinal</i>	$L_{\pm}, SV_{\pm}$	$u_r, u_z$	$\sigma_{rr}, \sigma_{\theta\theta}, \sigma_{zz}, \sigma_{rz}$
<i>Flexural</i>	$L_{\pm}, SV_{\pm}, SH_{\pm}$	$u_r, u_z, u_{\theta}$	$\sigma_{rr}, \sigma_{\theta\theta}, \sigma_{zz}, \sigma_{rz}, \sigma_{\theta z}, \sigma_{r\theta}$

Table 2.2 Characteristics of the three modes in cylindrical components [26].

Where L, SV, and SH correspond to longitudinal, shear vertical and shear horizontal deformation components. The + and – terms correspond to perturbations propagating in the direction of increasing and decreasing radius [26].

In orthotropic material, guided wave propagation exhibits different characteristics compared to isotropic material where material properties vary with orientation [10]. Timber

has a very complicated internal structure and is considered highly dispersive. The solutions of the wave equation are not available yet for orthotropic cylinders due to the complexity of guided waves. Therefore, simplifications to the model can be applied where wood can be considered as transversely isotropic instead of orthotropic. However, wood cannot be modeled as an isotropic material due to the deviation of the results from the actual ones. A comparison between modeling isotropic and transversely isotropic wood is conducted by Subhani and Li [10] that highlight the importance of considering timber as an anisotropic medium for guided wave propagation.

### **2.5.1. Guided Wave Behavior in Isotropic Cylindrical Structures**

As mentioned earlier, guided waves in a finite medium are affected by the geometry and boundary conditions present. The velocity becomes a function of frequency and is defined by the phase velocity and group velocity. As notes by Subhani [2] the equation that governs guided wave propagation can be expressed by the Navier-Stokes equation. From Hook's law it is given that:

$$[\sigma] = [C][\varepsilon]$$

Where  $\sigma$  is the stress matrix,  $C$  is the stiffness matrix and  $\varepsilon$  is the strain matrix. The elastic components in an isotropic model depend on two independent constants where the stiffness matrix is shown below:

$$[C] = \begin{bmatrix} C_{11} & C_{12} & C_{12} & 0 & 0 & 0 \\ C_{12} & C_{11} & C_{12} & 0 & 0 & 0 \\ C_{12} & C_{12} & C_{11} & 0 & 0 & 0 \\ 0 & 0 & 0 & \frac{C_{11} - C_{12}}{2} & 0 & 0 \\ 0 & 0 & 0 & 0 & \frac{C_{11} - C_{12}}{2} & 0 \\ 0 & 0 & 0 & 0 & 0 & \frac{C_{11} - C_{12}}{2} \end{bmatrix}$$

Where  $C_{11} = \frac{E(1-\nu)}{(1+\nu)(1-2\nu)}$  and  $C_{12} = \frac{E\nu}{(1+\nu)(1-2\nu)}$  [2]. The solution of guided wave

propagation in isotropic cylinders can be found in [20], [25], and [27] where they presented the solutions for different boundary conditions considering traction-free and embedded cylinders. From the GW solutions, important parameters such as the displacement field, dispersion relation and modes shapes can be determined and are presented in the following sections.

The wave equation is solved for the angular frequency ( $\omega$ ) and wavenumber ( $\xi$ ). The dispersion relation is derived from the relation between the real part of the wavenumber and input frequency. This relation was first derived by Pochhammer and Chree for longitudinal wave propagation. In traction free isotropic cylinders, the relation is described as follows [2]:

$$\frac{2\alpha}{a}(\beta^2 + \xi^2)J_1(a\alpha)J_1(\beta a) - (\beta^2 - \xi^2)^2J_0(a\alpha)J_1(\beta a) - 4\xi^2\alpha\beta J_1(a\alpha)J_0(\beta a) = 0$$

$$\begin{vmatrix} \left[ \frac{\lambda}{2\mu} (\alpha^2 + \xi^2) a^2 + (\alpha^2 a^2 - p^2) \right] J_p(\alpha a) + \alpha a J_p'(\alpha a) & (\beta^2 a^2 - p^2) J_p(\beta a) + \beta a J_p'(\beta a) & 2p[\beta a J_p'(\beta a) - J_p(\beta a)] \\ p[\alpha a J_p'(\alpha a) - J_p(\alpha a)] & p[\beta a J_p'(\beta a) - J_p(\beta a)] & -(2p^2 - \beta^2 \alpha^2) J_p(\alpha a) + 2\beta a J_p'(\alpha a) \\ -\alpha a J_p'(\alpha a) & -\left( \frac{\xi^2 - \beta^2}{2\xi^2} \right) \beta a J_p'(\beta a) & p J_p(\beta a) \end{vmatrix} = 0$$

$$\alpha^2 + \xi^2 = \frac{\omega^2}{C_l^2}$$

$$\beta^2 + \xi^2 = \frac{\omega^2}{C_s^2}$$

Where  $a$  is the cylinder radius,  $\alpha$  is the wavenumber for longitudinal waves,  $\beta$  is the wave number for shear waves,  $\xi$  is the wavenumber in the direction of propagation,  $J$  is the Bessel's function, and  $p$  is the cylinder's circumferential order. As mentioned earlier, the circumferential order  $p$  for longitudinal waves is zero, as for flexural waves it is greater than zero. The dispersion relation, also known as characteristic equation or frequency equation [2]. The solutions to this equation can be both real and imaginary, where the real roots represent the propagating branches of the present mode at the input frequency. It was previously stated that for cylindrical structures there are three main propagating wave modes that vary from torsional, longitudinal and flexural wave modes. Subhani mentioned that at each frequency the propagating branches have two types of velocities. The phase velocity which corresponds to the propagation of a constant phase, and the group velocity that indicated the energy of the wave propagating. These velocities are described in the following equations [2]:

$$V_{ph} = \frac{\omega}{Re(\xi)}$$

$$V_{gr} = \frac{d\omega}{Re(d\xi)}$$

As the velocity changes over the frequency range, the degree of dispersion becomes larger where at the same frequency the number of branches present increases. Frequency-wavenumber or dispersion curves can be traced from the numerical solution of the wave equation, and several computer software are available for this purpose. However, there are only two programs that model guided wave propagation for cylindrical geometries and are known to be DISPERSE and PCDISP. PCDISP is a MATLAB based program that solves the wave equation for single-layered and multi-layered cylindrical rods and traces phase and group velocity curves at different frequencies. However, only isotropic material can be modeled using this program. Below are the phase and group velocity curves generated using PCDISP for a multilayered cylinder with properties similar to that of wood. The propagating wave modes are indicated in Figure 2.4 which include flexural (a) and longitudinal wave modes (b).

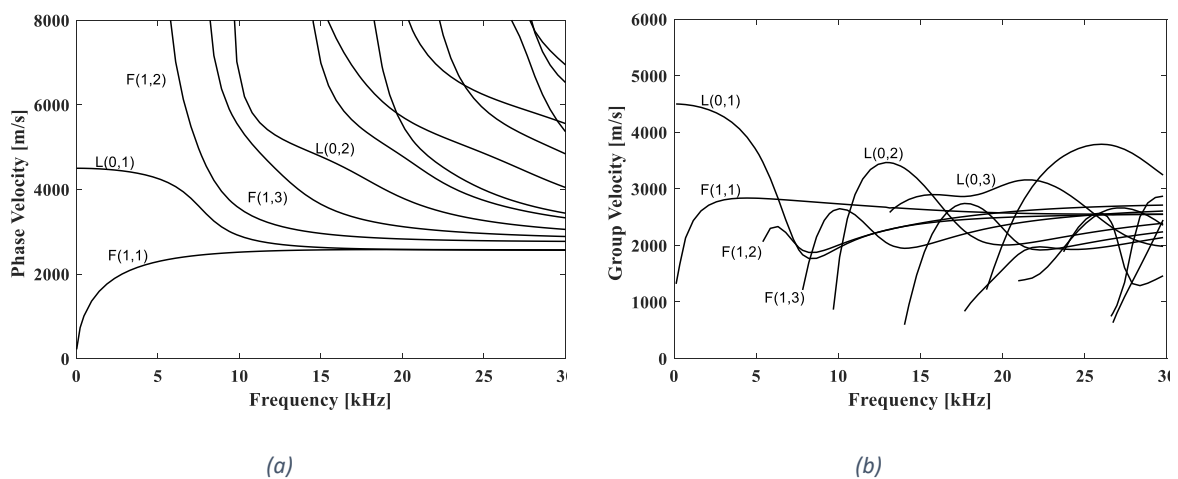


Figure 2.4 Dispersion curves for isotropic multilayered wood: (a) Phase and (b) Group velocity vs. frequency plots.

The displacement components for guided waves in polar coordinate systems considering an isotropic model are described as follows [2]:

$$u_r = \left[ A_1 \alpha Z'_p(\alpha r) - A_4 \xi Z'_p(\beta r) + A_6 \left( \frac{p}{r} \right) Z_p(\beta r) \right] \cos p \theta e^{i(\xi z - \omega t)}$$

$$u_\theta = \left[ -A_1 \left( \frac{p}{r} \right) Z_p(\alpha r) + A_4 \left( \frac{p \xi}{\beta r} \right) Z_p(\beta r) - A_6 \beta Z'_p(\beta r) \right] \sin p \theta e^{i(\xi z - \omega t)}$$

$$u_z = \left[ -A_1 \xi Z_p(\alpha r) - A_4 \beta Z_p(\beta r) \right] \cos p \theta e^{i(\xi z - \omega t)}$$

Where,  $u_r, u_\theta, u_z$  are the displacement components along radial, tangential and longitudinal direction.  $Z$  is the Bessel function.  $A_1, A_4$  and  $A_6$  are undetermined coefficients where  $A_1$  represents stretch (longitudinal effect) and  $A_4$  and  $A_6$  represent shear effect [10]. It is shown from the above equations that for  $p = 0$  only longitudinal components are present ( $u_r, u_z$ ). Whereas for  $p = 1$ , all three components are present which indicates the present of flexural waves.

When using guided waves propagation in SHM it is crucial to determine and separate the propagating waves in the structure. When impact is made longitudinally (eccentric or with an angle) both longitudinal and flexural wave can be generated. Also, it is clear from the above equations that longitudinal waves are not affected by the impact angle  $\theta$  [10]. The displacement field can be used to separate between the waves, since longitudinal waves are considered to be symmetric whereas flexural waves are antisymmetric.



## 2.5.2. Guided Wave Behavior in Transversely Isotropic Cylindrical Structures

Guided wave propagation differs between isotropic and transversely isotropic material, especially relative to the cut-off frequency of higher branches. This frequency is lower in transversely isotropic than the isotropic model [10]. Several factors are present when solving the wave equation that favor the transversely isotropic model. Some of these factors are fiber orientation in the timber pole, boundary conditions, and difference in material properties along cross section (latewood/earlywood) where a different density and modulus of elasticity must be considered. The stress strain relationship for anisotropic media are defined by the compliance matrix  $[S]$  as follows:

$$[\varepsilon] = [S][\sigma]$$

For transversely isotropic material the compliance matrix is defined by:

$$[S] = \begin{bmatrix} \frac{1}{E_r} & \frac{\nu_{\theta r}}{E_r} & \frac{\nu_{zr}}{E_r} & 0 & 0 & 0 \\ \frac{\nu_{r\theta}}{E_r} & \frac{1}{E_\theta} & \frac{\nu_{z\theta}}{E_\theta} & 0 & 0 & 0 \\ \frac{\nu_{rz}}{E_r} & \frac{\nu_{\theta z}}{E_\theta} & \frac{1}{E_z} & 0 & 0 & 0 \\ 0 & 0 & 0 & \frac{1}{G_{\theta z}} & 0 & 0 \\ 0 & 0 & 0 & 0 & \frac{1}{G_{rz}} & 0 \\ 0 & 0 & 0 & 0 & 0 & \frac{1}{G_{r\theta}} \end{bmatrix}$$

If the plane of isotropy is the  $r - \theta$  plane then  $\nu_{\theta r} = \nu_{r\theta}$ ,  $\nu_{rz} = \nu_{zr}$ ,  $\nu_{z\theta} = \nu_{\theta z}$ . In the case of timber, when considering a transversely isotropic model it is crucial to choose 5

elastic constrains available from litation or from semi-destructive testing to be able to generate the appropriate dispersion curves for analysis. For a wave propagating in the longitudinal direction of the cylinder (z-axis), the characteristic equation for a transversely isotropic cylinder is shown below [2]:

$$s^4(s^2 + \xi^2)(C_{11}C_{44}s^4 - \varsigma s^2 + \zeta) \left( \left( \frac{C_{11}-C_{12}}{2} \right) S^2 - \rho\omega^2 + \xi^2 \right) = 0,$$

$$\varsigma = (C_{13} + C_{44})^2 \xi^2 + C_{11}(\rho\omega^2 - C_{33}\xi^2) + C_{44}(\rho\omega^2 - C_{44}\xi^2),$$

$$\zeta = (\rho\omega^2 - C_{44}\xi^2)(\rho\omega^2 - C_{33}\xi^2)$$

The solution to the above equation was described by Honarvar [28] as follows:

$$s_1^2 = \frac{\varsigma - \sqrt{\varsigma^2 - 4C_{11}C_{44}\zeta}}{2C_{11}C_{44}}$$

$$s_2^2 = \frac{\varsigma + \sqrt{\varsigma^2 - 4C_{11}C_{44}\zeta}}{2C_{11}C_{44}}$$

$$s_3^2 = \frac{2(\rho\omega^2 - C_{44}\xi^2)}{2C_{11}C_{44}}$$

The same velocity relations presented in the previous section can be derived from the above solutions. As mentioned earlier, the programs that can generate dispersion curves for orthotropic or transversely isotropic materials are limited. DISPERSE is one of those programs that has the capability to calculary dispersion curves for cylindrical geometries with a multilayered structure. The layers can be modeled as either elastic, damped isotropic,

or anisotropic solid, which makes it a great solution for modeling guided waves in timber poles. For a transversely isotropic cylinder the displacement fields are shown as follows

[2]:

$$u_r = \left\{ \begin{array}{l} A_p \left[ \left( s_1 \frac{p}{r} + i\xi a s_1 \frac{p}{r} q_1 \right) J_p(s_1 r) + (-s_1 - i\xi a q_1 s_1) J_{p+1}(s_1 r) \right] \\ + B_p \left[ \left( s_2 \frac{p}{r} q_2 + i\xi a s_2 \frac{p}{r} \right) J_p(s_2 r) + (-s_2 q_2 - i\xi a s_2) J_{p+1}(s_2 r) \right] \\ + C_p \left[ \left( \frac{p}{r} \right) J_p(s_3 r) \right] \end{array} \right\} \cos(p\theta) e^{i(\xi z - \omega t)}$$

$$u_z = \left\{ \begin{array}{l} A_p [(i\xi + a q_1 s_1^2)(s_1 r)] \\ + B_p [(i\xi q_2 + a s_2^2) J_p(s_2 r)] \end{array} \right\} \cos(p\theta) e^{i(\xi z - \omega t)}$$

$$u_r = \left\{ \begin{array}{l} A_p \left[ \left( -\frac{p}{r} - i\xi a \frac{p}{r} q_1 \right) J_p(s_1 r) \right] \\ + B_p \left[ \left( -\frac{p}{r} q_2 - i\xi a \frac{p}{r} \right) J_p(s_2 r) \right] \\ + C_p \left[ \left( -\frac{p}{r} \right) J_p(s_3 r) + s_3 J_{p+1}(s_3 r) \right] \end{array} \right\} \sin(p\theta) e^{i(\xi z - \omega t)}$$

It is also shown from the above equations that for  $p = 0$ , only longitudinal and axial components are present. The equations have the same features as the isotropic model, but with a more complicated structure. For  $p = 1$ , all three components are present, and the waves are considered as flexural. In literature, the circumferential order 'n' is a more common than 'p' indicating whether the propagating modes are axisymmetric or non-axisymmetric. For  $n = 0$ , waves are considered as axisymmetric waves (longitudinal and

torsional), whereas if  $n \geq 1$  non-axisymmetric waves (flexural) are present. Further information about each type of wave is discussed in detail in section 4.

### **2.5.3. Limitations of Guided Wave Based NDT**

When modeling wave propagation in timber it is important to consider the three-dimensional wave theory that is also known by guided wave theory. As Subhani [2] mentioned, the actual three-dimensional behavior of the propagating waves is better understood where the velocities of the different modes, displacements and power functions can be determined. On the hand, some limitations are present for non-destructive tests based on the guided wave theory. One of the main assumptions is that the waves propagate in an infinite medium with certain boundary conditions. The limitations are within the application of these boundary conditions, which can be explained from the dispersion relation and is discussed by Subhani [2]. Studies on circular rods are continuously performed but with some simplifications to the model. For instance, longitudinal loading is considered where the loading is considering symmetrical across the length of the rod [2], which is due to the fact that the studies are performed on semi-infinite cylinders.

Guided waves are one of the most successful NDT to evaluate circular timber elements. The effects of dispersion can be minimized by creating various actuator-sensor arrangements that can limit the propagation of unwanted wave modes. Subhani [2] presented a complete study on the importance of considering timber a transversely isotropic material by comparing it to the isotropic model. He also highlighted that the simplifications to the boundary conditions applied might limit the time domain reconstruction of a finite

length element as well as the negligence of loads in the characteristic equation. Therefore, numerical methods can be integrated and are beneficial for this purpose.

# **Chapter 3 Understanding Guided Wave Propagation Behavior in Utility Timber Poles**

## **3.1. Introduction**

Timber is considered one of the important substitutes for steel and other materials when it comes to construction, utility poles or any other application. There are many characteristics that favor wood over these materials; however, there are additional concerns that must be taken into consideration when using wood in any application. For instance, besides being prone to structural damage from loads and connections, wood is subjected to other serious natural decays and damages that could affect its health. Therefore, careful health monitoring must be conducted to timber structures in order to maintain the condition and extend the total life cycle. Among the various non-destructive techniques for the evaluation of timber, guided stress wave propagation is considered one of the most efficient and reliable techniques that provide sufficient quantitative and qualitative assessment. However, for circular timber in particular, it is more complicated than other materials and geometries due to its orthotropic non-linear nature, and to the fact that not enough experimental validation has been provided regarding guided wave propagation.

A detailed study on a western white pine timber pole is conducted numerically and experimentally where the guided wave (GW) theory is directly applied to primarily understand the behavior of GWs, test methods for wave mode tuning and mode characterization, and to suitably investigate ways for reducing the dispersion phenomenon. Macro Fiber Composites (MFCs), which are active piezoceramic composite transducers (PCTs) were used to generate and sense guided waves along the structure (Smart Material

corp., 2017). The MFCs were conveniently coupled to the timber's surface and were able to accommodate changes in the geometry of the pole. Dispersion curves were generated using DISPERSE [17] for transversely isotropic round timber to assist in the frequency selection. The application of an MFC-ring was then depicted to eliminate the propagation of unwanted wave modes and enhance the desired ones and their reflections. The excitation frequency was selected according to a set of factors such as the number of propagating wave modes and the amount of dispersion present. The MFC-ring application also depended on the excitation frequency and the order of propagating wave modes. Additionally, the effect of change in boundary conditions on guided wave behavior was portrayed where soil was added numerically and experimentally. The effect of soil on reflections was analyzed using the proposed MFC actuation configurations and the selected excitation frequency.

## **3.2. Methodology**

### **3.2.1. Overview**

Oscillatory motions occur in a solid due to the displacement of particles from their original equilibrium position. The movement of these particles is restricted by the physical properties of the structure. As mentioned, wood is an orthotropic material with a complex nature where particles can only move along a guided path they're associated with. This path corresponds of circular waveguides that can be affected with the wood species available, moisture content, temperature, and the orientation of growth rings. In the case of circular

white pine timber which is the material used in this study, growth rings are oriented along the axial or longitudinal direction of the specimen as shown in Figure 3.1.

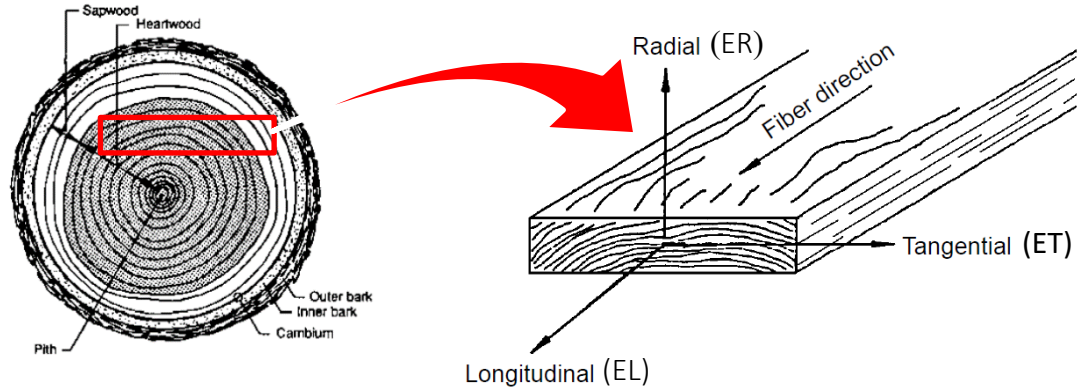


Figure 3.1 Orientation of growth rings in circular timber (pine).

As shown in Figure 3.1, the longitudinal axis (L) is parallel to the fiber direction, the radial axis R is normal to the orientation of growth rings; and the tangential axis T is tangent to the growth rings.

#### a) **Material Properties of Wood**

To properly describe the elastic behavior of wood, twelve constants are needed when considering an orthotropic model. The compliance matrix  $[S]$  is described as follows:



$$[S] = \begin{bmatrix} \frac{1}{E_r} & \frac{\nu_{\theta r}}{E_\theta} & \frac{\nu_{zr}}{E_z} & 0 & 0 & 0 \\ \frac{\nu_{r\theta}}{E_r} & \frac{1}{E_\theta} & \frac{\nu_{z\theta}}{E_z} & 0 & 0 & 0 \\ \frac{\nu_{rz}}{E_r} & \frac{\nu_{\theta z}}{E_\theta} & \frac{1}{E_z} & 0 & 0 & 0 \\ 0 & 0 & 0 & \frac{1}{G_{\theta z}} & 0 & 0 \\ 0 & 0 & 0 & 0 & \frac{1}{G_{rz}} & 0 \\ 0 & 0 & 0 & 0 & 0 & \frac{1}{G_{r\theta}} \end{bmatrix}$$

As mentioned by Mascia [29], the theory of elasticity in wood is based on the assumption that wood has three planes of elastic symmetry. Most of the studies consider wood as a cylindrical anisotropic body where the properties and characteristics are in function of the cylindrical coordinate system  $r, z, \theta$ . The elastic modulus and Poisson's ratio are related by the following expression [30]:

$$\frac{\mu_{ij}}{E_i} = \frac{\mu_{ji}}{E_j}, \quad i \neq j, j = L, R, T$$

When examining wave propagation in timber, several parameters must be taken into consideration such as the effect of humidity and temperature, growth rings and grain angle. For the timber specimen used in the experimental setup, the type of wood is western white pine mainly found in the United States and is used for utility poles and railroads. Figure 3.2 shows the timber specimen in the lab where the growth rings are shown to be oriented longitudinally.



Figure 3.2 Growth ring orientation in the lab's timber specimen.

The global coordinate system is denoted in the cartesian form  $(X, Y, Z)$  where the origin is located in the center of the element. As for the material coordinate system the axis is shown in polar or local coordinate system  $(R, L, T)$  or  $(r, z, \theta)$  where the origin is located in the center of the material, L axis is along the axial (longitudinal direction), and the R-T plane depends on the grain direction. The coordinate system is shown in Figure 3.3 with the components.

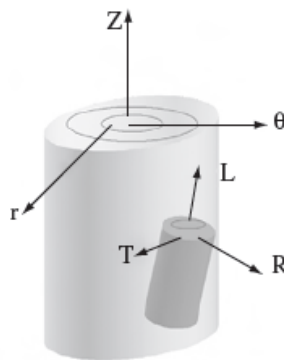


Figure 3.3 Coordinate system for the cylindrical timber pole.

A transformation between the element and material coordinate systems is described as follows:

$$\begin{bmatrix} x \\ y \\ z \end{bmatrix} = A^T \begin{bmatrix} l \\ r \\ t \end{bmatrix}$$

$$\text{where } A = \begin{bmatrix} l_x & l_y & l_z \\ r_x & r_y & r_z \\ t_x & t_y & t_z \end{bmatrix}$$

To properly model the problem and compare the experimental results to the numerical ones, the same type of wood must be considered where the mechanical properties are required. From literature [31], the elastic properties are extracted where they are present in function of the longitudinal elastic modulus. For the specimen used in the experimental setup, the material is western white pine wood with the following elastic properties:

Property	E <sub>L</sub> (GPa)	E <sub>R</sub> (GPa)	E <sub>T</sub> (GPa)	G <sub>LR</sub> (GPa)	G <sub>LT</sub> (GPa)	G <sub>RT</sub> (GPa)	ρ (kg/m <sup>3</sup> )
Value	11.11	0.422	0.866	0.825	0.795	0.250	380

*Table 3.1 Material Properties for Orthotropic Timber [31].*

To simplify the analysis for both experimental and numerical tests, the material is considered to be transversely isotropic instead of orthotropic with the properties shown below. The dispersion curves were generated according to these properties, as well as the numerical experiments performed on COMSOL that are further elaborated in the following sections.

Property	$E_L$ (GPa)	$E_R$ (GPa)	$E_T$ (GPa)	$G_{LR}$ (GPa)	$G_{LT}$ (GPa)	$G_{RT}$ (GPa)	$\rho$ (kg/m <sup>3</sup> )
Value	11.11	0.866	0.866	0.577	0.577	0.533	380

Table 3.2 Material Properties for Transversely Isotropic Timber [31].

## b) Dispersion Curves

The propagation of mechanical waves is governed by the direction of elongation of waveguides present in the structure as mentioned earlier. In general, waveguide propagation has two main characteristics, discretizing the waves into propagating modes and the existence of dispersion. From the solutions of the dispersion equation it is shown that there is an infinite number of propagating wave modes as the frequency reaches infinity. However, for a given frequency there must a finite number of propagating modes present whose properties are determined by the material properties, geometry of the cross section and the boundaries of the waveguides [26]. In this study, the cross section of the specimen is circular, and the waveguides are cylindrical where the displacement vector has three components as shown in Figure 3.4.

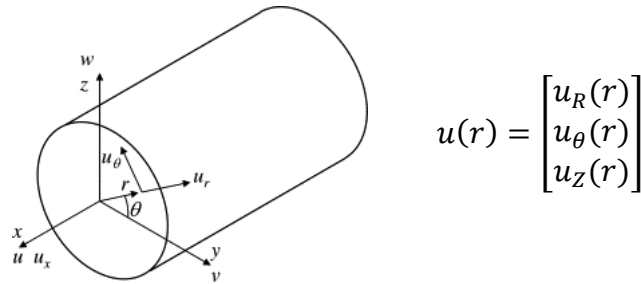
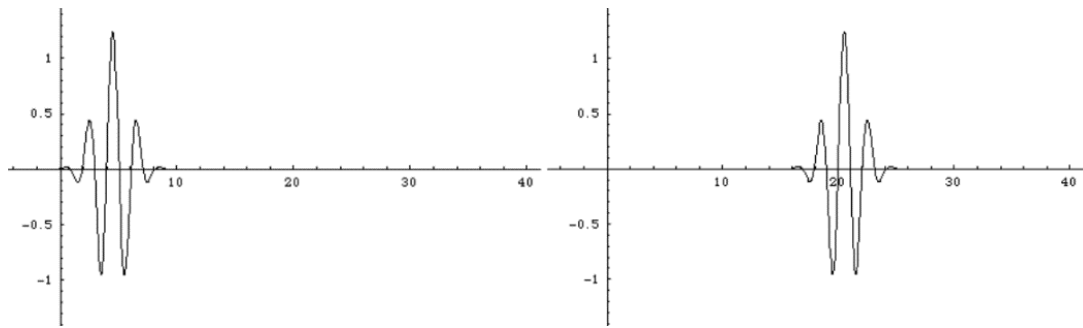


Figure 3.4 Displacement components in cylindrical elements.

There exists a nonlinear relationship between frequency and wavenumber, where the signals can get distorted as they travel along the waveguides. The change of shape and amplitude of the propagating packet makes it much harder to analyze, determine peaks and indicate reflections. Consider the wave packet shown in Figure 3.5 with multiple frequency components that is propagating in a non-dispersive medium.



*Figure 3.5 Non-dispersive propagating wave packet [32].*

It can be shown from the above figure that as the wave propagates in the non-dispersive medium, the shape is maintained because the velocity is not dependent on frequency anymore. However, in a dispersive medium it is the complete opposite. Since the propagating packet is made up of several frequency components each travelling at a different speed, the shape of the packet changes completely as it propagates in the dispersive medium. Figure 3.6 shows how the shape changes with time for a case where the low frequency components (large wavelength) travel faster than high frequency components of the packet (small wavelength) [32].

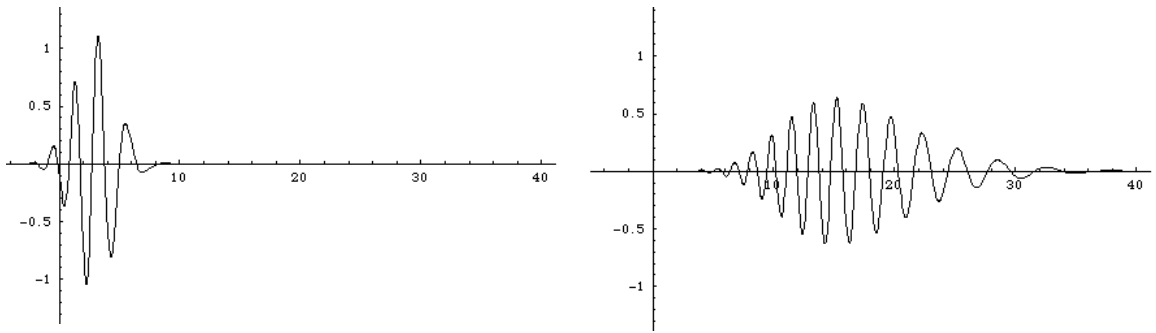


Figure 3.6 Dispersive propagating wave packet [32].

The above wave packets can be displayed by a Gaussian function containing multiple frequencies where it is shown in Figure 3.7 that for a non-dispersive medium (shown in black) the frequencies travel all at the same speed and the central frequency is kept constant. However, for the dispersive medium (blue) the frequencies travel at different speeds and the shape of the function dramatically changes.

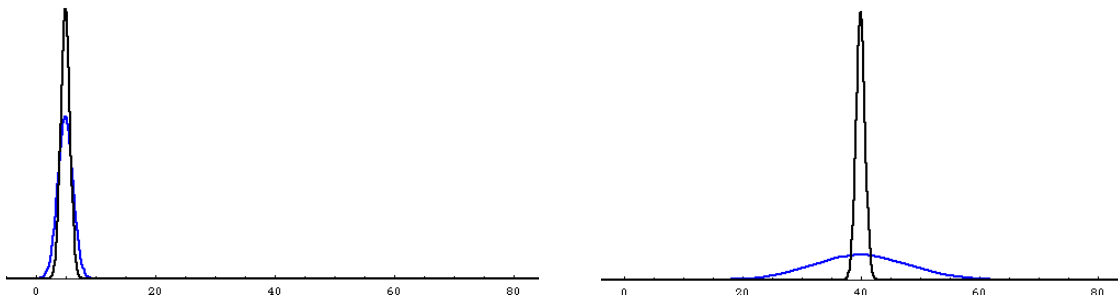


Figure 3.7 Gaussian functions for a non-dispersive packet (black) and a dispersive packet (blue) [32].

In a research performed on natural fiber composite panels [33], J. Tucker explained how a dispersive wave packet changes shape as it propagates due do the

difference between the group and phase velocities. This difference creates distortion inside the signal as seen in Figure 3.8.

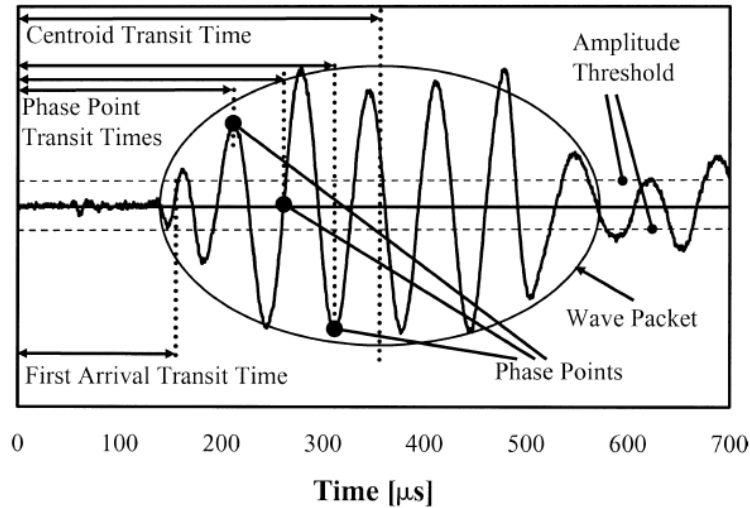


Figure 3.8 15kHz dispersive wave packet of a 4-cycle burst [33].

J. Tucker mentioned that the phase points within a wave packet move relative to the centroid of the packet. The centroid transit time shown in Figure 3.8 is the time used to calculate the group velocity, while the phase point transit time is used to calculate the phase velocity [33]. However, the phase point transit times are usually extremely hard to indicate. In bulk wave propagation, the group and phase velocity are equal where there is no effect of dispersion.

Wood is considered a highly dispersive medium due to its complex nature in addition to the non-linear geometry of the structure. When working with guided waves in timber poles, extreme care should be taken when it comes to the dispersive nature of the propagating modes which calls a need to control this issue. M. Subhani in [12] studied how the effect of dispersion can be reduced in timber poles by increasing the number of cycles

used in the input tone burst. Consider the 5-cycle hanning window burst shown below with a central frequency of 15kHz. Applying Fourier transform to the above packet we can see the single sided amplitude spectrum of  $S(t)$  in Figure 3.9 where the frequency ranges  $9\text{ kHz} < f < 21\text{ kHz}$ .

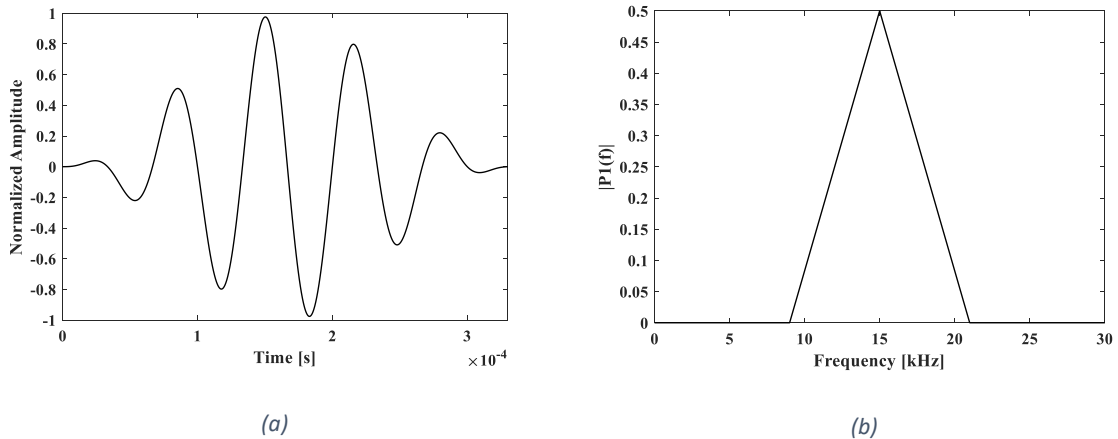
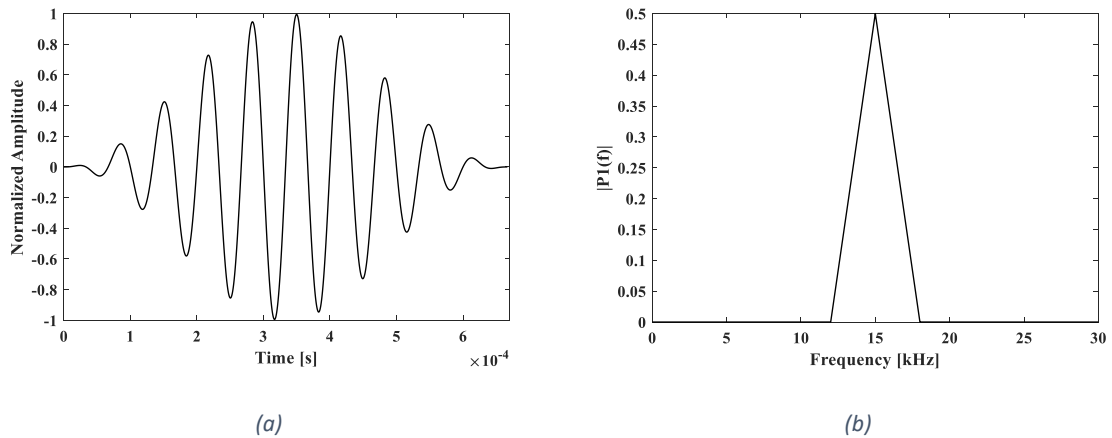


Figure 3.9 5-cycle Hanning window burst at 15 kHz: (a) original cycle and (b) single sided amplitude spectrum after Fourier transform.

As mentioned earlier, multiple frequency components of a dispersive packet travel at different speeds, and when the range of the components is large the effect of dispersion will be higher, causing the signal to get more distorted. Consider a 10-cycle hanning window burst with 15kHz frequency shown in Figure 3.10 below.





(a) (b)  
 Figure 3.10 10-cycle Hanning window burst at 15 kHz: (a) original cycle and (b) single sided amplitude spectrum after Fourier transform.

The overall time of this packet is rather larger than the 5-cycle one, however if the single sided spectrum is observed one can notice that the frequency components are much lower. The components vary from the central frequency in the range of  $12 \text{ kHz} < f < 18 \text{ kHz}$ . The frequency components for both tone bursts are different, increasing as the number of cycles decrease. This might have a significant effect on dispersion, since the frequency components travel at different speeds. The effect of number of cycles on the propagating signals is highlighted in the results section.

As mentioned in the previous sections, in circular solids three types of modes may be present: Longitudinal (L), Torsional (T), and Flexural (F) waves. For a certain frequency there exist a finite number of  $L(0,m)$ ,  $T(0,m)$  and  $F(n,m)$  modes that might be propagating depending on the cutoff frequency of each mode. The cut-off frequency is the value for which a certain mode starts to propagate. Below the cut-off frequency of a given mode, it does not propagate and can only exist as an evanescent wave [34]. Dispersion curves were generated from DISPERSE software for a transversely isotropic timber pole. Group and

phase velocity vs. frequency curves are shown only for longitudinal and flexural wave modes which are the main interest in this study. The group velocity is directly used to characterize the propagating wave modes. The central transit time of each propagating packet is extracted and used for the calculation of the velocities. The phase and group velocity of the longitudinal wave modes is shown in Figure 3.11.

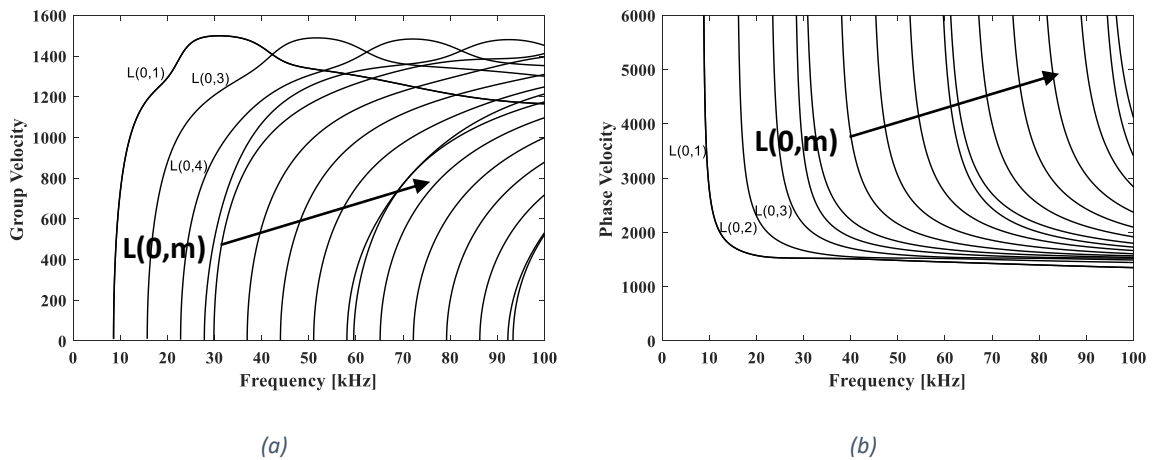


Figure 3.11 Dispersion curves: (a) group velocity and (b) phase velocity vs. frequency for longitudinal wave modes.

For the flexural wave modes, it is a much more complicated case. For every circumferential order  $n \geq 1$  there exist a flexural wave mode of a given family. During the generation of these curves in DISPERSE some issues were accompanied since the software does not automatically plot all circumferential orders. Instead, they were calculated manually which lead to a loss of accuracy with respect to the group velocity. However, these faults were disregarded in this work where the range of interest was between 10 kHz to 20 kHz, due to the presence of lower number of wave modes. Figure 3.12 displays the group and phase velocity plots for the flexural modes of order 1.

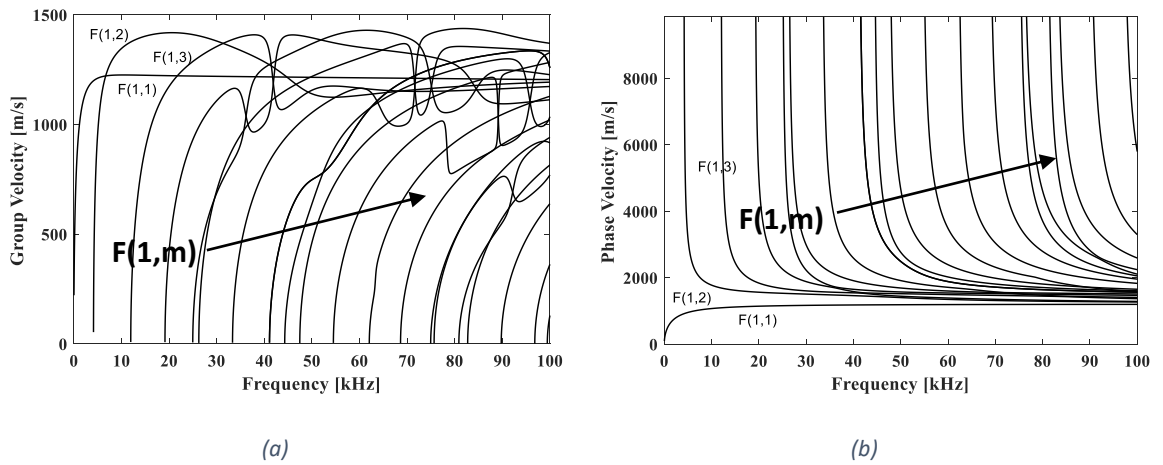


Figure 3.12 Dispersion curves: (a) group velocity and (b) phase velocity vs. frequency for flexural wave modes of order 1.

Figure 3.13 shows the group velocity plots for flexural modes of higher orders  $n = 2, 4$  and 8.

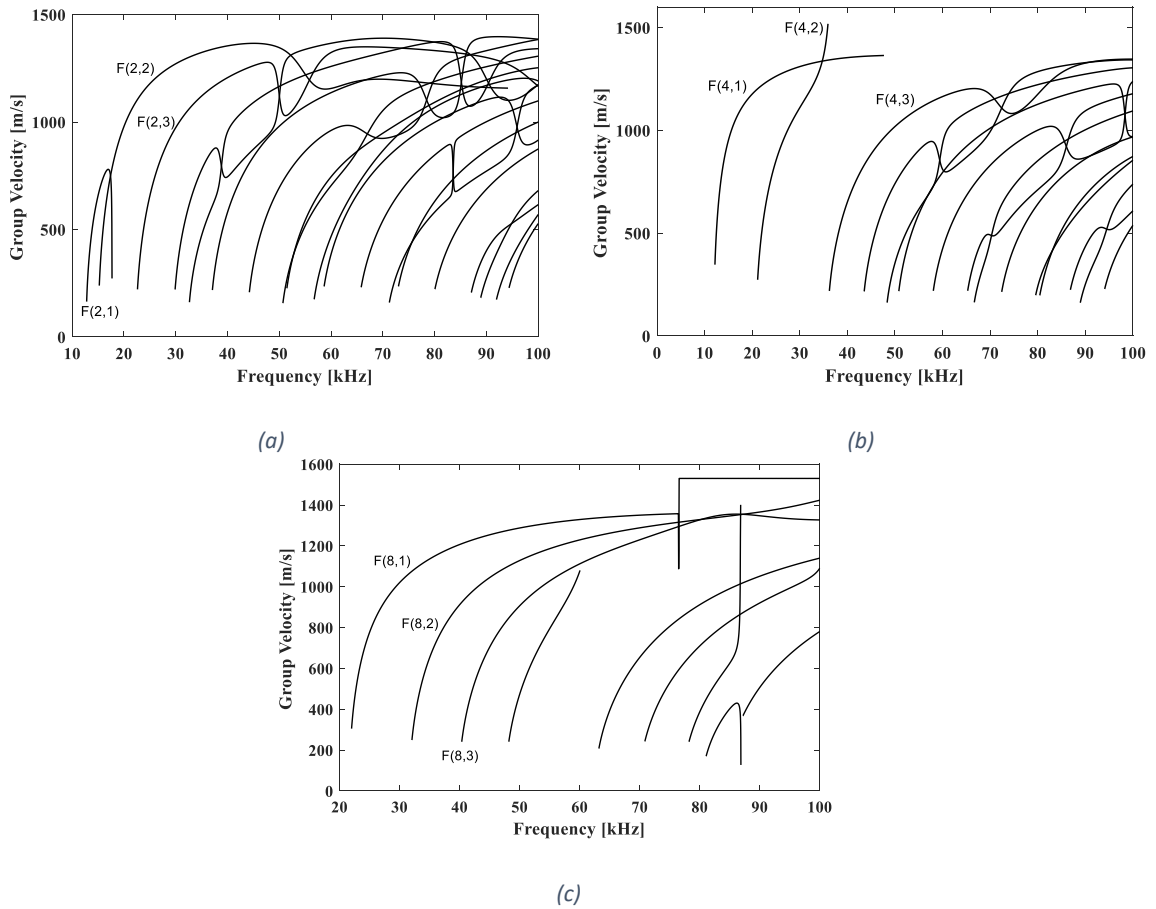


Figure 3.13 Dispersion curves: group velocity vs. frequency for flexural wave modes of orders (a)  $F(2,m)$ , (b)  $F(4,m)$  and (c)  $F(8,m)$ .

The wavelength at certain frequencies is crucial for the numerical analysis since the size of the mesh depends on it. In general, when studying wave propagation in solids, it is very crucial to determine the wave mode that is being excited. For this reason, the frequency of excitation must be carefully selected to prevent the excitation of several modes which makes it much harder to differentiate between them, in addition to the presence of dispersion that could distort the signal completely. From the phase velocity of

the flexural modes of first order, which have the highest velocities, the minimum wavelengths can be calculated and are shown in Figure 3.14.

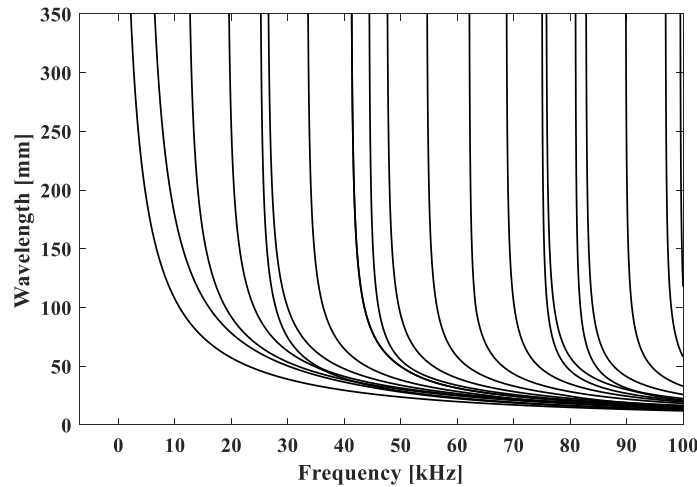


Figure 3.14 Wavelength vs. Frequency.

### c) Propagating Wave Modes and Their Characteristics

The high number of propagating wave modes in the first range of low frequencies is shown from the above curves, in addition to the presence of dispersion in both longitudinal and flexural modes. In this section the modes of interest in this study are discussed in detail, and the excitation frequency is selected according to that criteria. Nevertheless, one method for controlling the propagation of certain wave modes – which is later applied in the methodology – is depicted in the second section.

The solutions of the wave equation are classified into wave modes depending on their symmetry properties, which is in function of the circumferential order  $n$  [26]. Torsional modes  $T(0,m)$  involve the azimuthal component of the displacement vector  $u_{\theta}(r)$  with  $n = 0$ . Longitudinal modes  $L(0,m)$  involve both radial and axial components of

the displacement vector  $u_R(r), u_Z(r)$  with  $n = 0$  and propagate with axially symmetry along the cylinder. Flexural modes  $F(n,m)$  involve all three components of the displacement vector and are labeled as anti-symmetric with circumferential order  $n \geq 1$ . As for the index  $m$ , it is labeled as the thickness mode number since it characterizes the number of nodes of the mode shape across the tube's wall [35]. Figure 3.15 shows the mode shapes for longitudinal wave modes for different values of thickness mode number. For  $m = 0$ , a bulk longitudinal wave propagates (non-dispersive media). It is shown that when the mode shape has one node  $m$  is equal to 1. When two nodes exist,  $m$  is equal to 2. The same applies for the rest of the wave types.

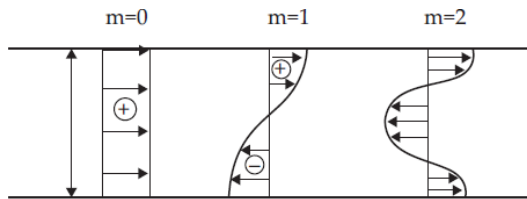


Figure 3.15 Mode shapes for different thickness number values (longitudinal wave modes) [35].

In longitudinal waves, particles move parallel to the direction of propagation of the wave where the cylinder can be considered as being compressed. Particles in torsional waves move in perpendicular to the wave propagation direction where the cylinder is considered twisted along its axial direction. On the other hand, flexural waves include particle motion parallel and perpendicular to the wave propagation at the same time. The three waves can be visualized in Figure 3.16 by the deformation caused to the cylinder. In general, torsional modes are the hardest to generate with conventional PZT devices.

Longitudinal waves excitation is easier but might encounter the excitation of flexural wave modes that might distort the signal and get affected by additional boundary conditions on the surface. Therefore, it is crucial to excite certain type of modes and eliminate any unwanted ones.

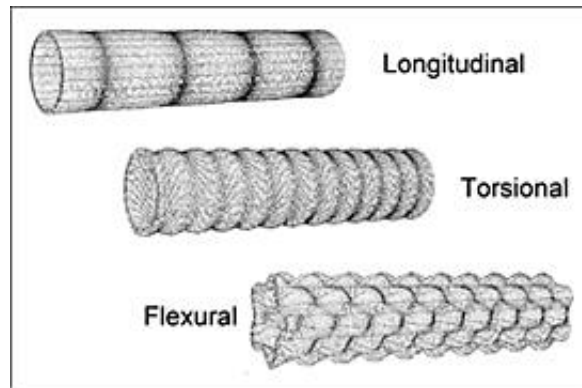


Figure 3.16 Longitudinal, Torsional and Flexural deformation of a cylindrical tube [36].

As mentioned by M.G. Silk in [37], axisymmetric wave modes  $T(0,m)$  and  $L(0,m)$  would be sensitive to wall thickness. As for the non-axisymmetric waves  $F(n,m)$ , they are also sensitive to wall thickness in addition to anything that affects the cylinder's flexural properties (mounting on the tube's surface). Flexural wave modes are one of the most complicated waves due to their non-axisymmetric properties and highly dispersive nature. They are only present in circular structures and are dependent on the circumferential order  $n$  as mentioned earlier. This value provides critical information when dealing with wave tuning and mode characterization, where it indicates the integer number of wavelengths present around the circumference – i.e. the order of symmetry around the axial direction [34]. For axisymmetric modes (longitudinal and torsional) the displacements do not vary

with angle. However, for  $n = 1$  (first order flexural mode) the displacements on top and bottom of the cylinder are  $180^\circ$  out of phase [34]. It is mentioned in [35] that flexural wave modes depend on the angular coordinate ( $\theta$ ) variation which is determined by the circumferential index  $n$ .

#### **d) Wave Mode Tuning**

The propagation of certain wave modes depends mainly on the frequency of excitation and the position of the excitation signal. If the surface of a cylindrical pole is excited at one point only, signals measured from an axial location will contain both longitudinal and flexural wave modes. The excitation of torsional wave modes is the most difficult where it requires specific torsional piezoelectric transducers, so they won't be encountered in the study. Nevertheless, for the evaluation of timber poles it is crucial to tune the propagating modes as much as possible. From the dispersion curves shown in the previous section, the high number of modes was shown to be present even at low frequencies with a significant effect of dispersion. Therefore, a need to cancel out unwanted modes is required at least in the frequency range of 10kHz to 20kHz which is the range of interest in this study.

The generation of non-axisymmetric wave modes can be restricted by the excitation of a transducer ring of piezoelectric elements equally spaced around the circumference of the cylinder. The configuration can cancel out the flexural modes and enhance the propagating longitudinal modes present at the frequency of excitation. Also, D.N. Alleyne and P. Cawley mentioned in [38] that longitudinal wave modes can be



suppressed if the length of the piezoelectric element is equal to the wavelength of the mode. The mode will be suppressed over the full wavelength and no propagation will occur. However, in the case of timber the wavelength of the low order modes is large (88 mm) which makes it difficult to apply this process. In order to suppress flexural wave modes, the total number of transducers placed around the circumference must be greater or equal than the highest circumferential order present at the frequency of excitation. For instance, when operating at a 12.5 kHz frequency the maximum mode order is 4 in F(4,m). This means that a minimum of 4 piezoelectric transducers must be mounted equally to suppress all the propagating flexural modes. L. Rose commented on the generation of purely axisymmetric guided waves in [9] by employing a uniform 360° loading in the circumferential direction. In some cases, exciting the complete circumference around the cross section with piezoelectric devices is not achievable due to the presence of gaps between the transmitters. These gaps can cause the generation of several wave modes that might include both axisymmetric and non-axisymmetric wave modes [7]. In addition to that, L. Rose mentions that the superposition of a high number of propagating modes can lead to the generation of quasi-axisymmetric wave modes [9]. Hence, by decreasing the gaps between the transmitters, non-axisymmetric waves are reduced and quasi-axisymmetric waves become almost purely axisymmetric [9]. Quasi-longitudinal waves can be generated from the transducer ring where they can travel at a lower speed. They can be thought of by partial longitudinal waves that are compressing and stretching the cylinder at the same time. On the contrary, pure longitudinal waves only compress the cylinder and propagate at a higher speed. The behavior of the particles in quasi-longitudinal and pure longitudinal waves are shown in Figure 3.17 and Figure 3.18 respectively. In Figure 3.17, compression makes the

bar thicker and stretching makes it thinner where the wave is not purely longitudinal. At the surface of the rod the quasi-longitudinal wave shows a transverse motion.

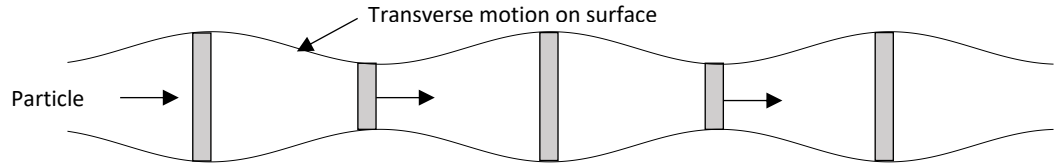


Figure 3.17 Particle displacement in quasi-longitudinal waves.

However, in pure longitudinal waves the bar is subjected to compression where the particles move axially in the direction of propagation of the wave with no movement in the transverse direction.

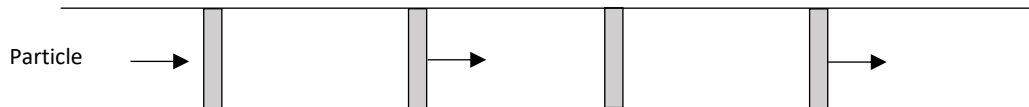


Figure 3.18 Particle displacement in pure longitudinal waves.

### 3.2.2. Numerical FEA Model

Guided wave propagation in timber poles was modelled numerically to validate the effect of actuating the circumference, optimize transducer configurations and study the wave behavior in a transversely isotropic medium at selected excitation frequencies.

COMSOL MULTIPHYSICS [39] is a powerful tool for the finite element modeling of

piezoelectric transducers generating guided waves in structures. The Piezoelectric Devices module is composed of two physics, Solid Mechanics and Electrostatics where each component in the study can be modelled separately. The guided wave propagation resulting in particle displacement and deformation was solved in the Solid Mechanics physics, while the piezoelectric effect and the actuation/sensing of the transducers were solved in the Electrostatics physics. The numerical model was simulated on an Intel ® Xeon ® 2.10 GHz virtual machine with 150 GB RAM and 300 GB disc space, which created some computational limits especially at high frequencies.

A complete finite element model for the timber specimen was conducted in COMSOL where the actual geometry and boundary conditions were applied, in addition to the MFCs for actuation and sensing processes. Modelling the MFC numerically was challenging due to the complexity of the structure, where it is composed of several stacked layers of different materials. Therefore, the MFC was modeled as a thin flat piezoelectric transducer of type PZT-5A coupled to a flat surface on the timber pole. The properties were determined using a macroscopic approach, where the MFC was considered as a representative volume element (RVE) [40], which corresponded of a small section of the MFC that contained all layers present. The properties of the RVE were considered to be the same as the entire MFC structure and were directly applied to the plate-like (rectangular) transducer in the numerical simulations.

**a) Model 1 – Ring Design**

The propagation of certain wave modes depends mainly on the excitation frequency and the position of the excitation signal. If the surface of the timber pole is excited at one point only, signals measured from an axial location will contain both longitudinal and flexural wave modes [41]. The excitation of torsional waves is the most difficult where it requires specific torsional piezoelectric transducers, so they were not accounted for in this work. For the evaluation of timber poles, it is important to tune the propagating modes as much as possible. From the dispersion curves, the high number of modes was shown to be present even at low frequencies with a significant effect of dispersion. Especially for the case of flexural modes that are much more complicated than longitudinal ones. Therefore, a need to cancel them out in the frequency range of 10 kHz to 20 kHz is required. As mentioned, the number of transducers actuated around the circumference of the pole must be greater or equal than the highest circumferential order of flexural modes. Figure 3.19 (a) shows the dispersion curves for mode F(4,m) where at 12.5 kHz, the maximum circumferential order is 4. This means that a minimum of 4 MFCs must be mounted equally to suppress the propagating flexural modes at this excitation frequency. However, at higher frequencies the maximum circumferential order is  $> 7$  which requires the actuation of 8 or more MFCs around the circumference. Therefore, the excitation frequency was selected at 12.5 kHz where the effect of MFC ring can be investigated properly. In addition, fewer number of modes propagate at this excitation frequency with a lower amount of dispersion than other frequencies. The selected frequency was also restricted by the maximum capability of the virtual machine used for the simulations. As

for the number of transducers in the ring, a total of 8 MFCs was added to properly test the effectiveness of the ring (flexural modes cancellation). Three actuation configurations were tested and compared, which corresponded of single, 4 and 8-MFC actuation.

Wavelength curves from DISPERSE shown in Figure 3.19 (b), are crucial for the numerical analysis in order to calculate the mesh size, where an average of 6-10 elements per wavelength is required [42, 43]. For instance, the wavelength at 12.5 kHz is around 88 mm which results in a maximum element size of 14.7 mm when divided among 6 elements (minimum value). However, convergence tests were performed on the calculated mesh size and yielded stable results at 6.5 mm with around 13 elements per wavelength, which was used throughout the entire simulations. The input signal to the MFC actuators is a 5-cycle Hanning window sine wave, where one face of the MFCs was set to be grounded with zero voltage and the other face set to have the electric potential with the input signal. Figure 3.20 (a) displays the timber pole modeled in COMSOL where the ring design is displayed. The MFC actuator ring (MFC1) is shown on the left end of the pole, in addition to the sensor rings (MFC2 to MFC4) placed at different locations along the specimen. The rings correspond of 8 MFCs equally mounted around the circumference. Figure 3.20 (b) shows the 6.5 mm mesh applied to the timber specimen in the ring design model. All mesh elements were swept triangular elements resulting mainly in prism, hexahedral and quadrilateral elements. The total number of elements was 219580 leading to 704211 degrees of freedom, which used up to 80 GB RAM and 100 GB disc space. The length of the pole modeled in this section was 1-meter with a 22 cm diameter, which was sufficient for the MFC ring design testing.

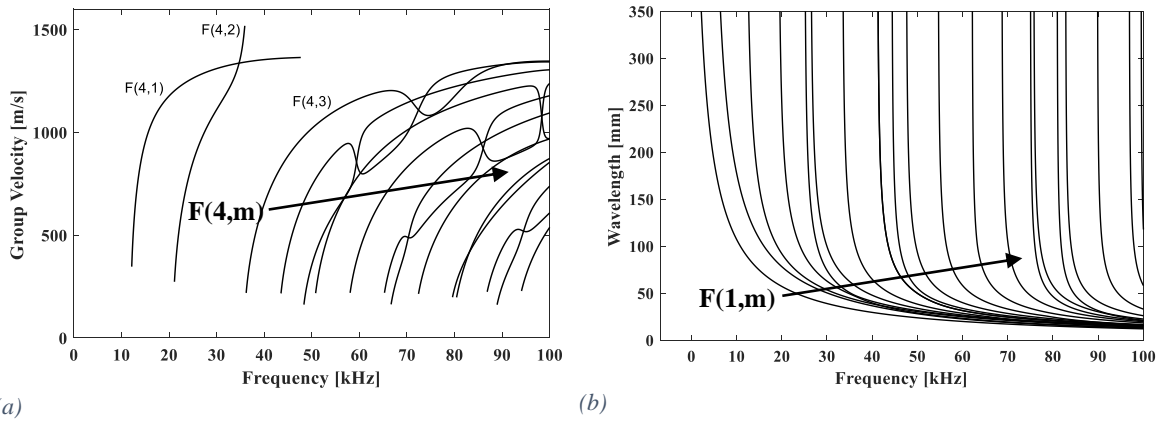


Figure 3.19 Dispersion curves: (a) group velocity vs. frequency plot for  $F(4,m)$  wave mode and (b) wavelength vs. frequency plot for flexural modes  $F(1,m)$ .

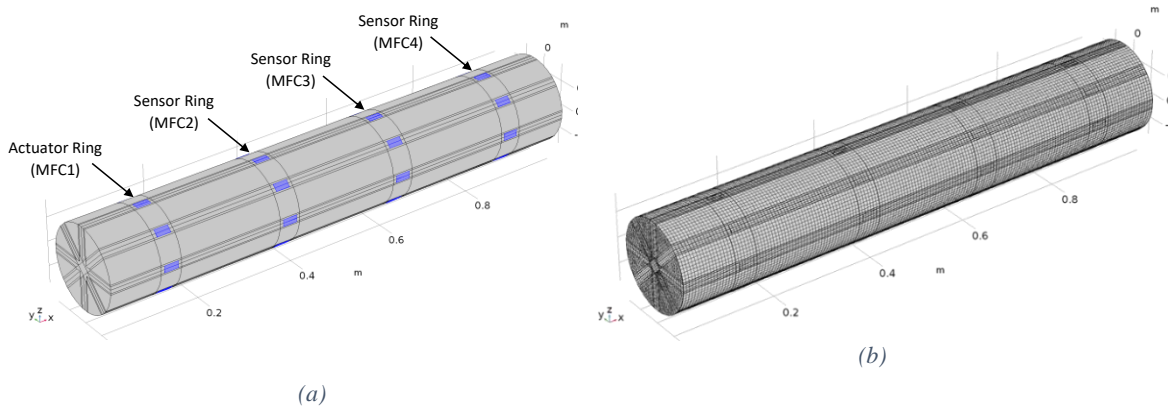


Figure 3.20 Timber pole: (a) Ring design model and (b) 8.8 mm mesh size applied to the model in COMSOL.

## b) Model 2 – Effect of Boundary Conditions

The change in boundary conditions was scrutinized in this work by comparing a traction free and embedded timber model. Soil was added to a section of the timber pole to analyze the effect on guided wave behavior both numerically in COMSOL and experimentally. For utility poles in specific, the recommended embedment depth is 10% of the total pole's length plus 2 ft (61 cm) [44]. Modeling soil numerically can be done using several methods which are found in literature [45-47], however in this work it was modeled

as linear elastic material with isotropic properties [48]. The effect of soil embedment on damping and attenuation of the propagating wave modes was inspected in COMSOL, as shown in Figure 3.22, where the traction free model (a) is shown next to the embedded model (b). In this section, the length of the pole was 5.5 meters which is longer than the one used in Model 1, in order to account for a suitable embedment length of 1.45 meters. The selected embedment length was the probable value of an in-service embedded utility pole with an 8-meter length. However, due to computational limits the 8-meter pole cannot be modeled in COMSOL and was substituted by a 5.5-meter model.

The actuation and sensing locations were optimized to reduce the effects of overlapping wave mode arrivals and simplify the acquired signals. The actuators were placed 0.8 meters from the sensor, which is located 1.5 meters from the right edge of the pole as shown in Figure 3.21. Figure 3.22 (c) shows the MFC actuator ring and MFC sensor in the COMSOL model. The excitation frequency was selected at 12.5 kHz for the same reasons discussed in the previous section, and the actuator ring contained 8 transducers, to be able to actuate single, 4 and 8-MFCs separately to test for flexural mode suppression.

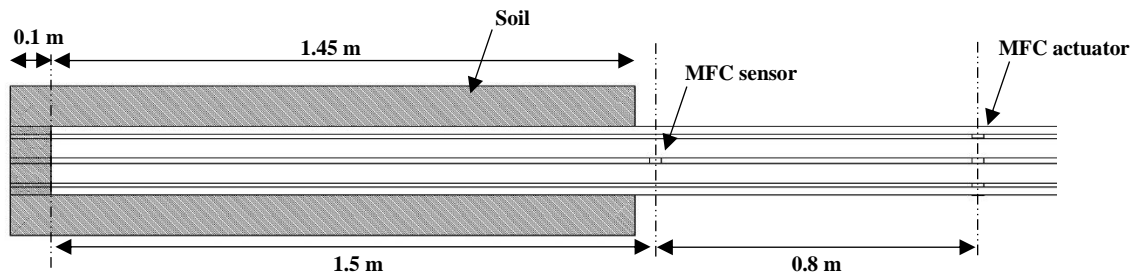


Figure 3.21 Top view sketch of the timber pole displaying the embedded condition and the transducers' locations.

Soil – timber interaction must be modelled carefully in COMSOL to provide an appropriate understanding of the effect of soil on guided waves. A contact node was added to the common surface between both timber and soil. The contact pressure method used was Penalty, which is based on the insertion of a spring between the contact surfaces [39]. The stiffness of the spring, or the penalty factor, is crucial for the stability and accuracy of the model. The effective gap distance between the two surfaces in contact was forced to be zero initially, considering that there is a perfect bond between the soil and the timber. As for applying mesh to the model, the same elements as Model 1 were used which are mainly quadrilateral elements with initial maximum element size of 8.8 mm at 12.5 kHz frequency. The mesh size converged at 5.5 mm, which was used in the simulations and is shown in Figure 3.22 (d). The total number of elements generated was 2142013 with 6502028 degrees of freedom which used 150 GB RAM and 280 GB disc space, the maximum capacity of the virtual machine available in our laboratory.



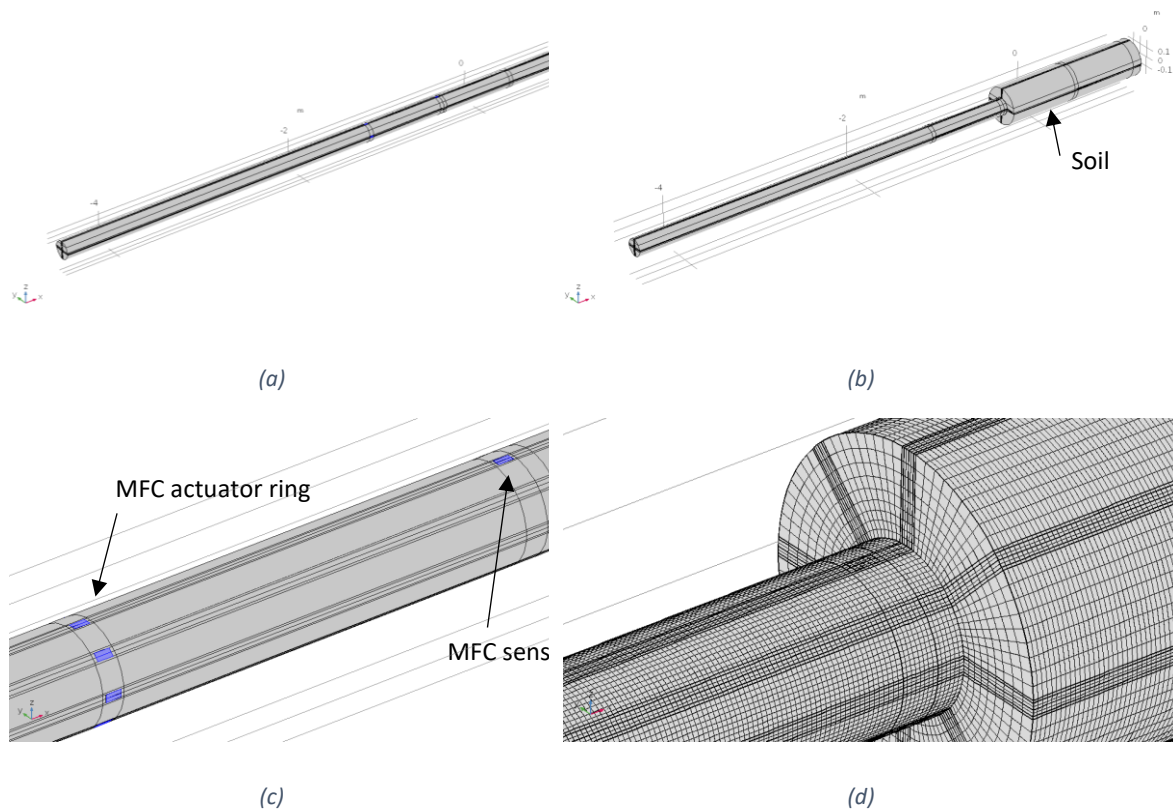


Figure 3.22 5.5-meter timber pole in COMSOL: (a) traction free model, (b) embedded model, (c) MFC actuator ring and sensor placement and (d) 5.5 mm mesh applied to the embedded model.

### c) Macro Fiber Composites (MFCs)

MFC transducers were chosen in this study because of their numerous advantages in guided wave propagation applications. As shown in Figure 3.23, the MFC structure is composed of a Polyimide film on the top and bottom with a 60  $\mu\text{m}$  thickness (50  $\mu\text{m}$  PI + 18  $\mu\text{m}$  Cu), and piezoelectric fibers of type PZT-5A with a thickness of 180  $\mu\text{m}$ , 28 mm length and 350  $\mu\text{m}$  width. The total number of fibers in the structure is 34 with a 55  $\mu\text{m}$  spacing between each. Structural epoxy is filled in the gap spacing between the fibers and the Polyimide film.

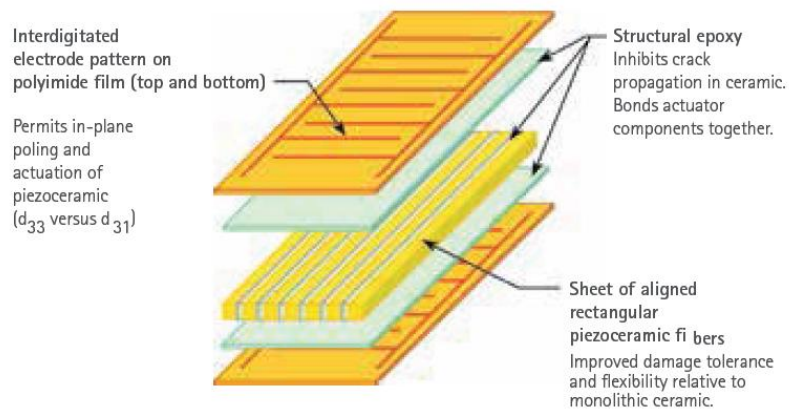


Figure 3.23 Schematic structure of the MFC [49].

One of the advantages of using MFCs is the capability to couple them to any structure due to their physical flexibility, unlike any other piezoelectric transducer. The surface of the timber pole is curved, where the MFC can be easily coupled after treating the pole's surface. Vibrations are actuated from the MFC where the strain direction or the direction of propagation of the waves is along the longitudinal directions. The polarization direction is normal to the piezoelectric fiber's longitudinal direction (33) as shown in Figure 3.24. In addition, when the MFC is used as a sensor the strain is measured from the same direction and the polarization also occurs in the z-axis resulting in the piezoelectric effect.

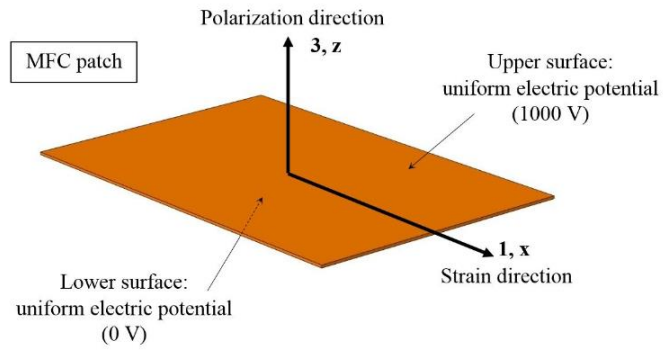


Figure 3.24 Voltage application schematic and polarization direction of the MFC.

The MFCs used in the experiment are the F1 type d33 defect model M-2814-P1 which are the most suitable for actuation/sensing operations. For the transducers used in sensing mode, the propagating waves generate strain across the structure and leads to the generation of a mechanical force on the front edges of the MFC (along its length). This force causes the displacement  $\Delta l_f$  in the piezoelectric element, which also generates a charge  $Q$  on the IDE electrodes that is introduced to the NC [40]. The electric voltage is then fed back to the IDE electrodes as shown in the Figure 3.25. The same process occurs for the transducers acting as actuators but in an opposite manner where the voltage is introduced to the IDE electrodes leading to the generation of the force along the length of the transducer.

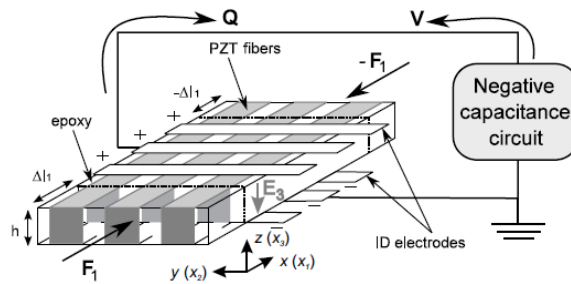


Figure 3.25 Scheme of the MFC acting as sensor.

### 3.2.3. Experimental Setup

The timber used in the experimental work was a western white pine (scots pine) pole which is the most common type used in utility poles for electric supply lines (also known as *Pinus Sylvestris* [50]). The setup is also divided into two sections as the numerical, where in the first section the excited modes are analyzed, and the effect of ring design was experimented on a 1-meter timber specimen. The second section depicts the validation of the setup and the effect of change in boundary conditions on an 8-meter length timber utility pole. MFCs of type M-2814 P1 were coupled to the pole's surface using Loctite's E120 HP epoxy adhesive at different locations along the specimen. The surface of the pole required treatment with sandpaper before the coupling process, where the position of interest was scraped to smooth off the surface. The location placement of the MFCs was extremely critical due to the presence of knots and cracks that can affect the propagating signal. The same locations as mentioned in the numerical model were applied in the experimental setup.

**a) Ring Design**

Several factors can affect the tuning and propagation of guided waves in timber poles. In addition to the presence of defects in the structure, the configuration of MFC transducers play an important role to acquire appropriate desired signals. As mentioned in the numerical model, the propagation of specific guided waves can be controlled by actuating an MFC ring placed around the circumference of the pole. The unwanted waves such as the flexural modes can be eliminated in addition to enhancing the propagating longitudinal modes and their reflections (in terms of voltage acquired). A total of 8 MFCs were coupled around the circumference as shown in

Figure 3.26 on the right (actuator ring MFC1). Sensors were placed at different locations along the specimen in a similar manner as the numerical model in COMSOL. The pole was simply supported on both ends. Regarding the excitation frequency, several values were tested between 10 kHz and 20 kHz to test the effectiveness of the actuator ring in eliminating propagating flexural modes. However, from the dispersion curves it was shown that at 12.5 kHz, 4 or more of the MFCs in the ring would be enough to cancel high order modes  $F(4, m)$ . At higher frequencies 7 or more MFCs might be needed, which restricts the range of frequencies that can be used in the experiments. Therefore, the frequency selected was 12.5 kHz which was used throughout the entire experimental testing and the actuation ring contained a total of 8-MFCs.

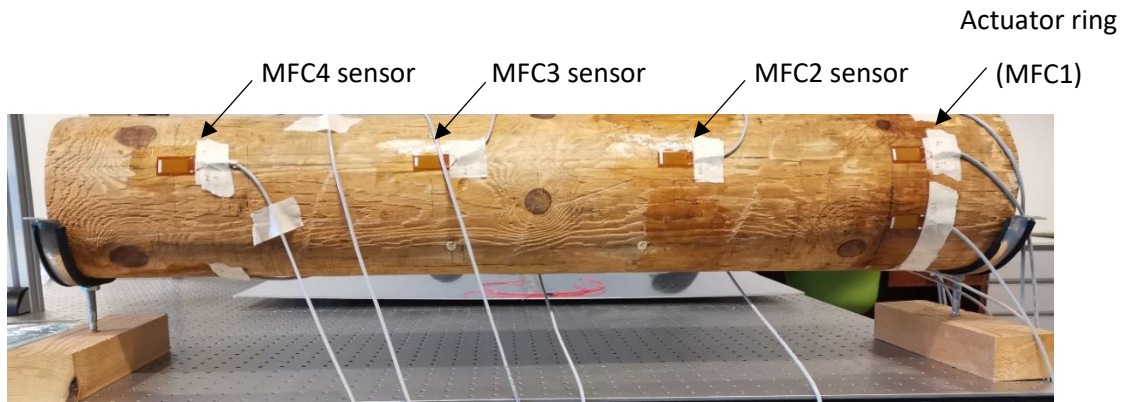


*Figure 3.26 MFC configuration on the timber pole displaying the MFC actuator ring and sensors.*

**b) Validation – Effect of Boundary Conditions**

Experimental validation was performed on an 8-meter timber utility pole where the effect of MFC actuator ring was tested, in addition to the change in boundary conditions considering traction free and soil embedment setups. In order to create an arrangement where the variable is the embedded condition, a wooden box was inserted at the back end of the pole where soil can be added and removed. Figure 3.27 (a) displays the 8-meter pole where the bottom section is inserted into the box. The pole was simply supported at the top end with metal supports and wood plies at the bottom end inside the box. The testing setup was only performed on the bottom section of the pole, which was the location of interest, where less reflections from the top end of the pole can be acquired. The 8-MFC actuator ring and sensor were placed 2.3 meters and 1.5 meters from the bottom end of the pole as shown in Figure 3.27 (b). In order to avoid variations during the experiment, all setups were performed simultaneously where the embedded setup was directly tested after the traction free setup. To simulate the embedded condition, soil was added gradually to the

wooden box and pressed at each layer to provide as much contact as possible with the surface of the timber pole.



(a)



Figure 3.27 (a) 8-meter timber utility pole and (b) MFC actuators and sensor configuration on the bottom end of the pole.

### c) Data Acquisition

The equipment used in the experimental setup were a Keysight 33500B signal generator, EPA-104 Piezo System Inc amplifier and Keysight InfiniiVision DSO-X-3024A oscilloscope. The 5-cycle Hanning window input signal to the actuator was generated with an initial peak to peak voltage of 10 V, then passed through the signal amplifier which



increased the gain to reach almost 300 V peak to peak. Signals from the sensors were then acquired using the oscilloscope at a sampling rate of 2 MHz. The experimental setup for the ring design on the 1-meter length timber specimen is shown in Figure 3.28 below. The same setup was used for the validation performed on the 8-meter timber utility pole.

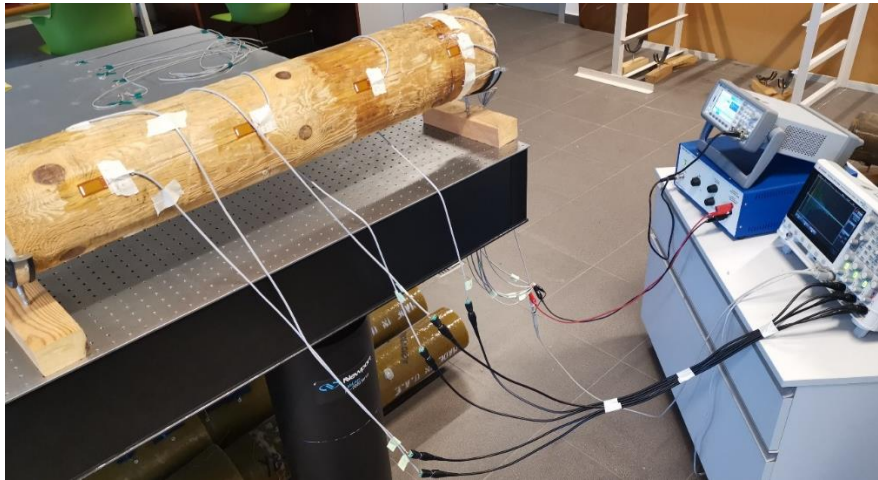


*Figure 3.28 Ring design experimental setup.*

#### **d) MFC – Timber Coupling**

Macro fiber composites (MFCs) were coupled to the surface of a 1-meter timber specimen for the generation and sensing of guided waves. The surface of the pole needed to be treated with sandpaper before the coupling process, where the position of interest was scratched to smooth off the surface (as shown in Figure 3.29). Due to the severe roughness of the wood's surface, an additional step was performed before the final coupling. A very thin layer of adhesive tape was applied to the smoothed surface which was left to dry for 24 hours. Figure 3.30 shows the four locations where the layer of coupling was applied which has been dried and ready for the final MFC coupling.





*Figure 3.29 Smoothing the pole's surface with sandpaper before MFC coupling.*



*Figure 3.30 Dry thin layer of epoxy adhesive applied for additional smoothing.*

After the last smoothing process, the MFC was ready to be coupled to the pole's surface. The same adhesive (Loctite's E120 HP Epoxy) was applied which is appropriate for both wood and MFC surfaces. The MFCs were pressed against the surface using rubber bands and Teflon tape during the 24-hour curing time. The Teflon was used to prevent sticking of the tape on the pole's surface where the adhesive was applied. Figure 3.31 shows the MFC coupled at the first position on the timber specimen.



*Figure 3.31 MFC coupled and pressed on one position of the pole's surface.*

The rest of the MFCs were coupled in the same manner, leaving them to cure for more than 24 hours to ensure decent bonding. The positions of the rest of the transducers were the same as the numerical model, where 3 sensor MFCs are mounted on the top surface (90 degrees) along the axial length of the pole where no cracks or knots are present. Two additional sensors were placed at the 4<sup>th</sup> position on the right and left side of the circumference, placed at a 0-degree angle from the radial axis. A total of 8 MFCs were coupled equally around the circumference where the actuation position took place. Figure 3.32 shows the MFC ring during curing where the Teflon tape is wrapped around the circumference.



*Figure 3.32 8-MFC Ring coupled around the circumference used for actuation.*

Three different actuation configurations can be performed after the final coupling of the MFCs to the structure. Since the 8 actuator transducers were placed equally around the circumference, the actuation of a single, 4-ring and 8-ring MFCs was only applicable. The single transducer that was excited was the one facing the top position where the rest of the sensors are placed. In the 4-ring configuration MFC1 TOP, MFC1 RIGHT 2, MFC1 LEFT 2 and MFC1 BOTTOM were excited, due to the location of the sensors placed at the 4<sup>th</sup> position. Last, in the 8-ring configuration all the transducers around the circumference were actuated.

### **3.3. Signal Processing**

The signals acquired experimentally/numerically were complex and difficult to analyze and process, especially due to the high dispersion, multi-modes and reflections from edges. Basic processing of the signals was applied initially to identify the propagating

wave modes from their group velocity in addition to some of their reflections by determining the time of flight. However, to further analyze the signals specific signal processing techniques were required that were able to decompose wave packets, identify reflections and compare amplitude variations. Also, high and low frequency components were removed using band pass filters on the acquired signals. Decomposing the signals in this work was done using the improved complete ensemble empirical mode decomposition with adaptive noise (CEEMDAN) method which was proposed by Colominas et. al. [51] and was proven to be reliable and more robust than its predecessors. This method decomposes the input signal into modes that are composed of multiple frequency and amplitude modulated functions. The sum of these modes, or intrinsic mode functions (IMFs), form the complete initial input signal [52]. The IMFs generated can help identify mode reflections and compare two signals more accurately.

When comparing the experimental acquired signals in the traction free and embedded setups, it was difficult to observe the difference or change in reflections as shown in Figure 3.33 (a) where the two signals are plotted above each other. However, after using CEEMD and decomposing the two signals the difference can be identified more clearly and the different wave packets were separated as shown in Figure 3.33 (b) to (d). The results displayed are for single MFC actuation at 12.5 kHz excitation frequency in the experimental testing performed on the 8-meter length pole.

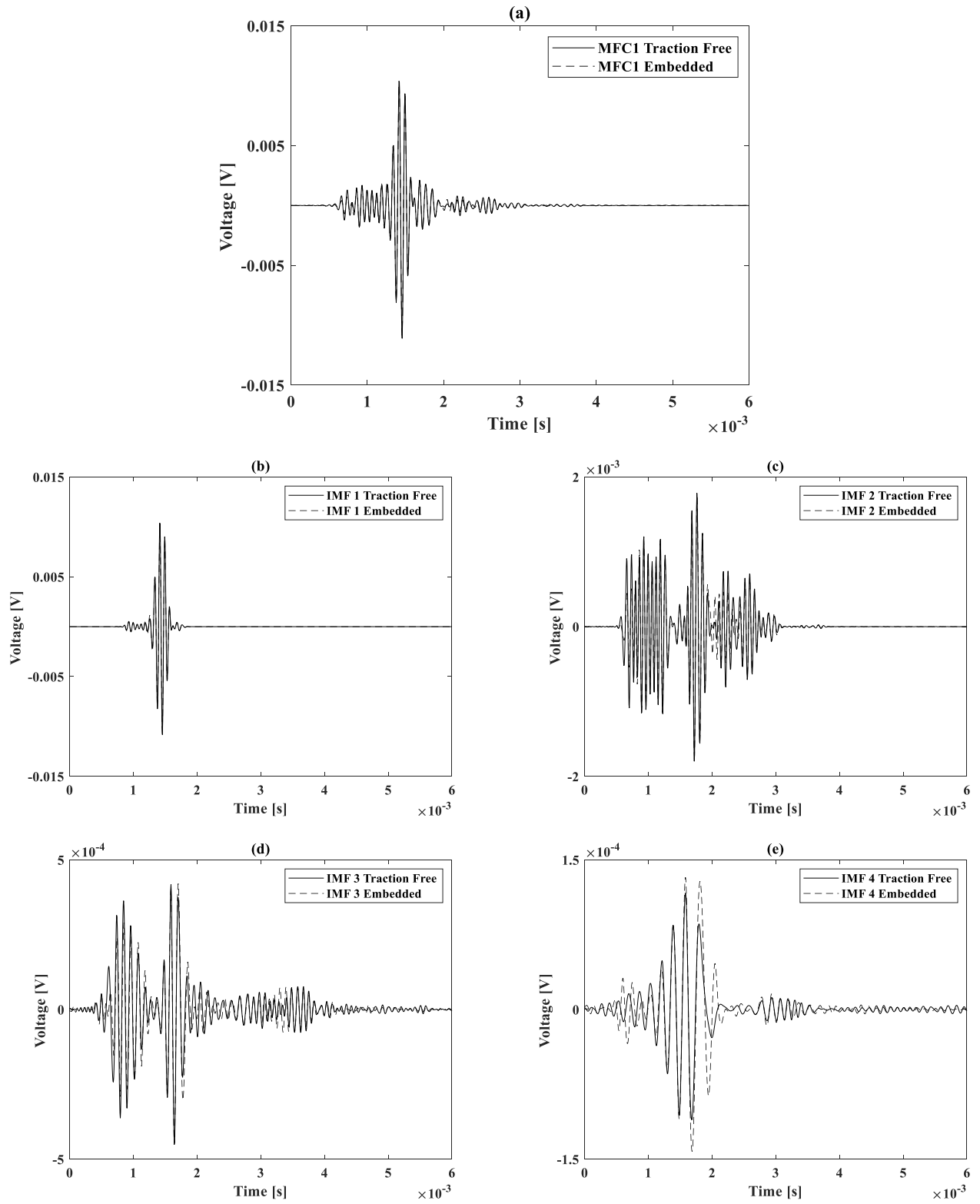


Figure 3.33 (a) Original experimental acquired signals at 12.5 kHz for traction free (solid) and embedded (dashed) single MFC1 actuation on the 8-meter length pole, (b) to (e) show the four IMFs of the signals after applying CEEMD.

### 3.4. Results & Analysis

#### 3.4.1. Tuning of the Excitation Frequency

In this section the excitation frequency was varied to analyze the propagating wave modes and their group velocity in the single actuation configuration, on the 1-meter timber specimen shown in Figure 3.34. From the dispersion curves it was observed that as the frequency increases, the number of modes present increase in both axisymmetric and non-axisymmetric waves. Plots for the raw data at several frequency values are represented in both experimental and numerical results for the sensor MFC4 TOP where the amplitude was normalized with respect to the maximum value.



Figure 3.34 Experimental configuration for tuning the excitation frequency.

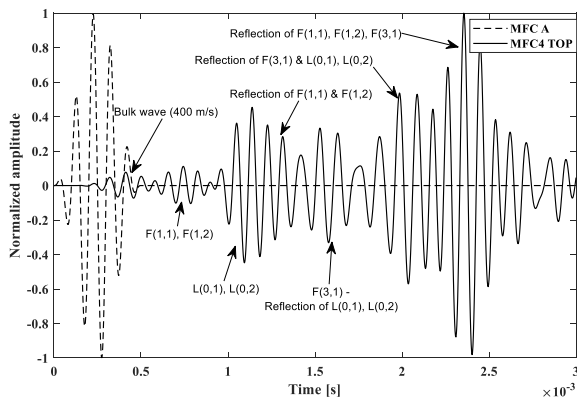
#### a) Numerical Results

The following plots represent data acquired numerically in COMSOL from MFC4 TOP sensor, for frequency values that range from 10 kHz to 25 kHz. This range will help understand the propagating wave modes at each frequency of excitation, determining the newly generated waves after their cut-off frequencies. The time of the simulations was  $3E-3$

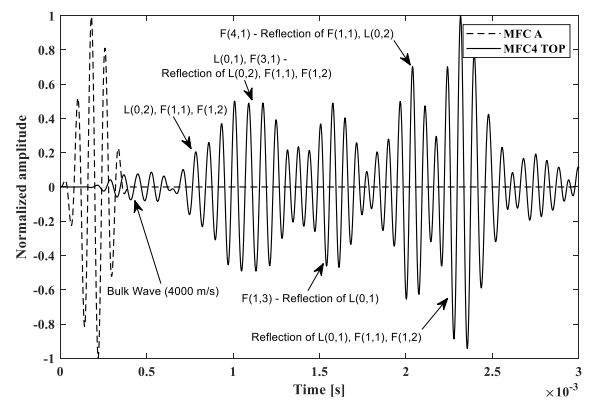
seconds for 10kHz to 17kHz, whereas the time for the rest of the frequencies was  $2E-3$  seconds due to the large mesh size and long simulation time. The numerical results confirm the propagating wave modes' characteristics from the dispersion curves shown previously due to several reasons. The mechanical properties used in the simulations were the same as the ones used for generating the dispersion curves in DISPERSE. This means that the group velocities calculated were more accurate and the propagating wave modes were identified more efficiently. Also, the timber pole modeled in COMSOL was a sound cylinder with no cracks or knots in the structure, unlike the specimen used in the experimental setup.

Looking at Figure 3.35 (a) for the 10 kHz excitation frequency. The bulk wave is captured propagating at a speed of 4000 m/s in the beginning of the acquired signal. F(1,1) and F(1,2) propagating at around 1345 m/s arrive after  $0.5E-3$  seconds. Longitudinal modes L(0,1) and L(0,2) arrive after  $1E-3$  propagating at around 750 m/s. The reflection of F(1,1) and F(1,2) also appears at the end of the same packet. F(3,1) and the reflection of L(0,1) and L(0,2) appear at  $1.5E-3$ . Also, the high-amplitude packet after  $2E-3$  is due to the concatenation of the reflections of L(0,1), L(0,2) and the flexural modes present. For 12.5 kHz excitation shown in Figure 3.35 (b), the same modes propagate since no additional cut-off frequency is reached. Figure 3.35 (c) shows the signal from exciting at 15 kHz, where additional flexural wave modes start to propagate that include F(1,3) and F(4,1) which makes the acquired signal more complicated. The dispersion of almost all the modes except F(1,1) causes the additional peaks shown. As for the 17.5 kHz excitation frequency in Figure 3.35 (d), the cut-off frequency is reach for mode L(0,3) where it start to propagate at  $1.5E-3$  seconds. Also, F(5,1) start to propagate and is reflected right after  $1.5E-3$ , in addition to the arrival of F(6,1) propagating at 443 m/s right after the time  $2E-3$  seconds.

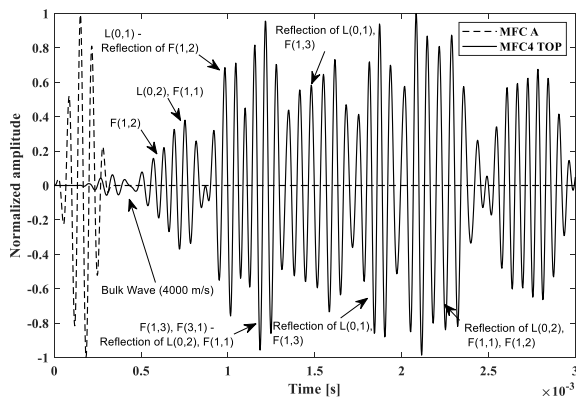
As the frequency increases to 25 kHz, additional wave modes start to propagate such as  $L(0,4)$ ,  $F(1,4)$ , and  $F(8,1)$  where they are shown in Figure 3.35 (e) – (g). The number of propagating wave modes increases as the frequency increases, which leads to several concatenated packets, that represent different wave mode arrivals, causing the signals to be more complicated to analyze.



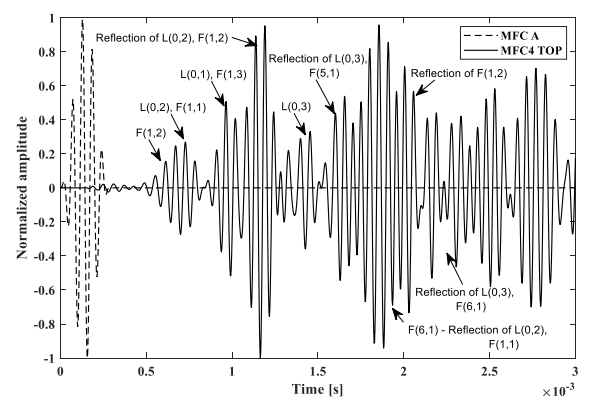
(a)



(b)



(c)



(d)



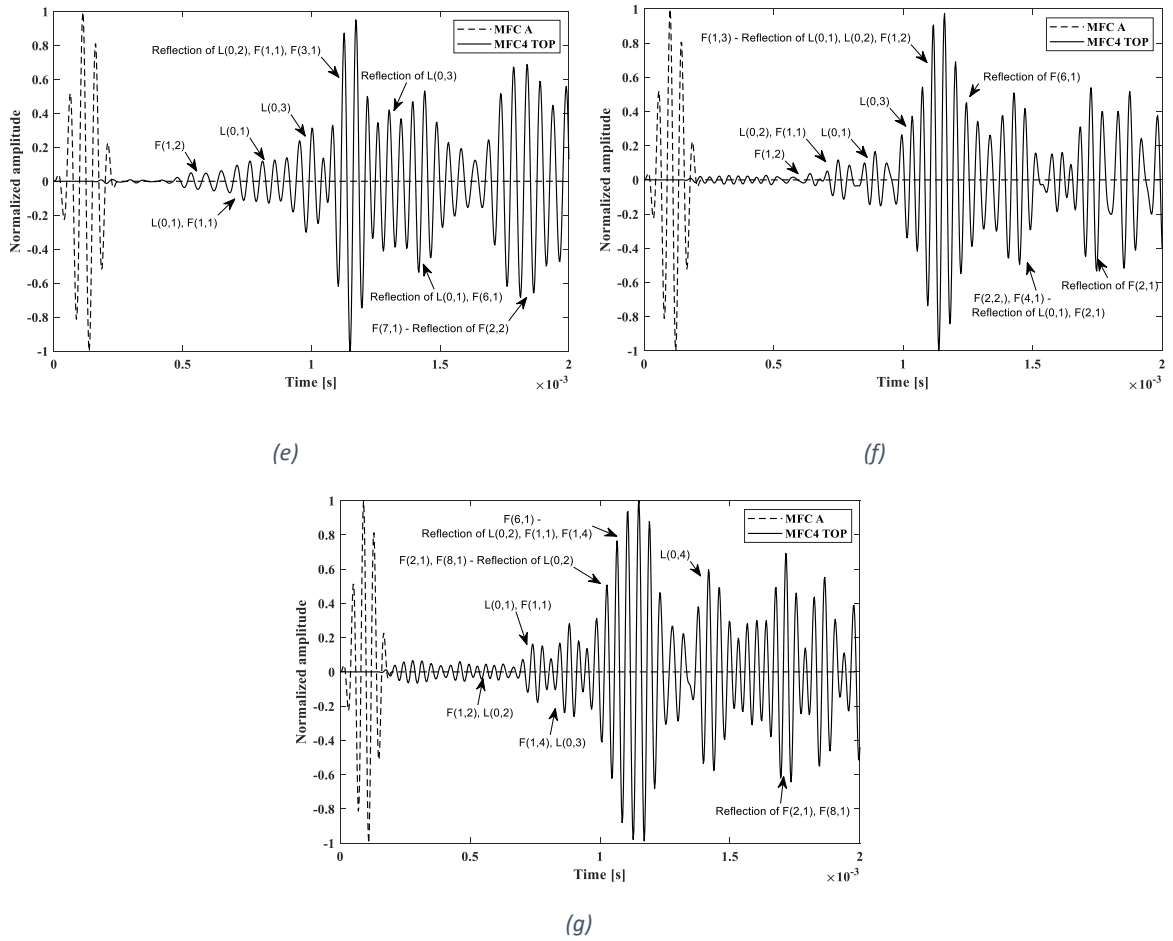


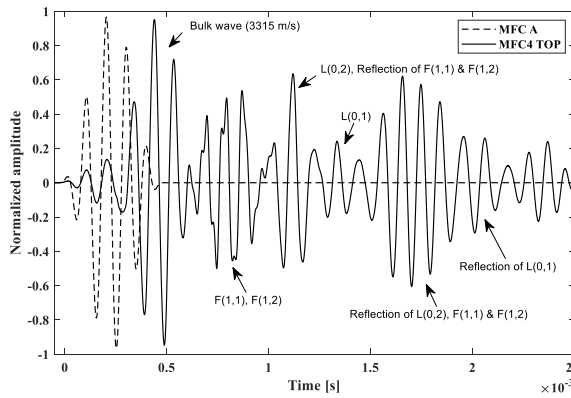
Figure 3.35 Numerical results: MFC4 TOP acquired signal using single MFC actuation at (a) 10 kHz, (b) 12.5 kHz, (c) 15 kHz, (d) 17.5 kHz, (e) 20 kHz, (f) 22.5 kHz and (g) 25 kHz.

## b) Experimental Results

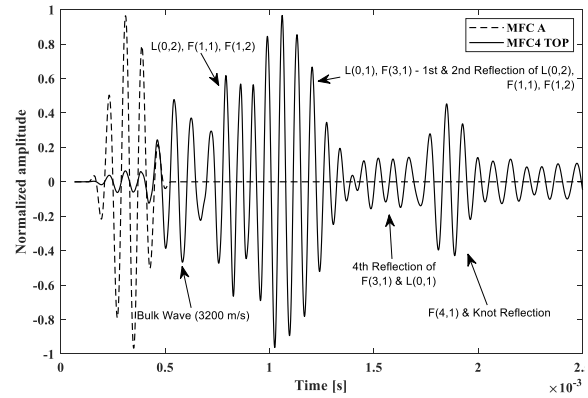
Similar to the numerical results, the same procedure is performed on the ones acquired in the experimental configuration. The frequency of excitation using the single actuation configuration is varied between 10kHz and 25kHz. From the acquired experimental results shown in Figure 3.36, it can be showed that as the frequency of excitation increases the number of propagating modes in the timber pole increase. As the frequency reaches the cut-off value of a certain wave mode, the evanescent nature decays

and the mode starts to propagate. For the 10 kHz excitation frequency, the dispersion curves show the propagation of longitudinal modes L(0,1) and L(0,2), in addition to the flexural modes F(1,1), F(1,2), F(2,1), F(3,1) and F(4,1) which all appear in the single actuation of MFC 1. All these modes appear in Figure 3.36 (a) in addition to a bulk longitudinal wave that is captured at low frequencies with a speed that varies between 3200 m/s and 4500 m/s. F(1,1) and F(1,2) propagate around 1346 m/s, where L(0,1) and L(0,2) propagate at 860 m/s and 734 m/s. The reflection of F(1,1) and F(1,2) concatenates with the arrival of L(0,1) after 1E-3 seconds as shown. In addition to that, the reflection of L(0,2), F(1,1) and F(1,2) appear between 1.5E-3 and 2E-3 seconds crossing a total distance of 1.25 meters. For the 12.5 kHz plot shown in Figure 3.36 (b), the bulk wave is present at the start of the signal at a speed of 3200 m/s. L(0,2), F(1,1) and F(1,2) arrive right before 1E-3 seconds crossing a distance of 75 cm with a speed of around 1350 m/s and 1226 m/s. The large-amplitude packet at 1E-3 seconds corresponds to the first arrival of L(0,1) and F(3,1) propagating at 1034 m/s in addition to the 1<sup>st</sup> and 2<sup>nd</sup> arrival of L(0,2), F(1,1) and F(1,2) crossing a total distance of 99.76 cm. The 4<sup>th</sup> reflection of F(3,1) and L(0,1) appears at 1.5E-3 seconds, in addition to the first arrival of F(4,1) right before 2E-3 seconds propagating at around 400 m/s. The high amplitude probably refers to the presence of a knot on the left side of the timber specimen. In Figure 3.36 (c), the same modes appear at the excitation frequency of 15 kHz. At 17.5 kHz shown in Figure 3.36 (d), an additional longitudinal mode L(0,3) appears where the cut-off frequency is reached. L(0,1), L(0,2) and F(1,2), F(1,1), F(3,1) propagate at almost the same speed of 1230 m/s and are concatenated in the high-amplitude packet present right before 1E-3 seconds. The reflection of L(0,2) and F(1,2), in addition to the first arrival of F(4,1) and F(5,1) appears between 1E-3 and 1.5E-3

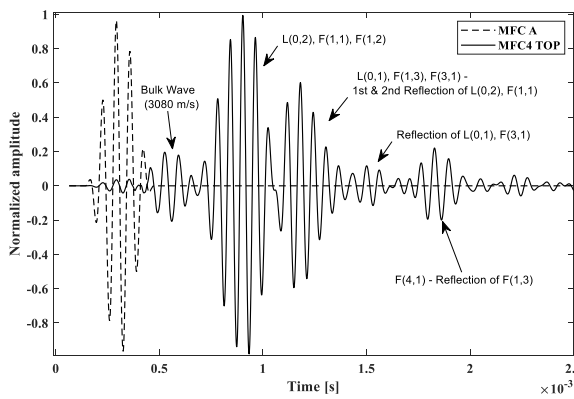
seconds. The new longitudinal mode  $L(0,3)$  arrives at  $1.5E-3$  propagating at a speed of 625 m/s and is reflected right before  $2E-3$  seconds. For the rest of the frequencies, some of the propagating modes are shown on the figures to prevent more complexity. However, at 25 kHz shown in Figure 3.36 (g) the additional modes propagating are  $L(0,4)$ ,  $F(1,4)$ ,  $F(6,1)$ ,  $F(7,1)$  and  $F(8,1)$ .



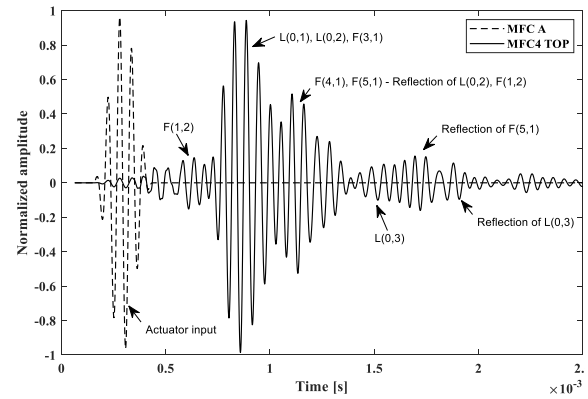
(a)



(b)



(c)



(d)

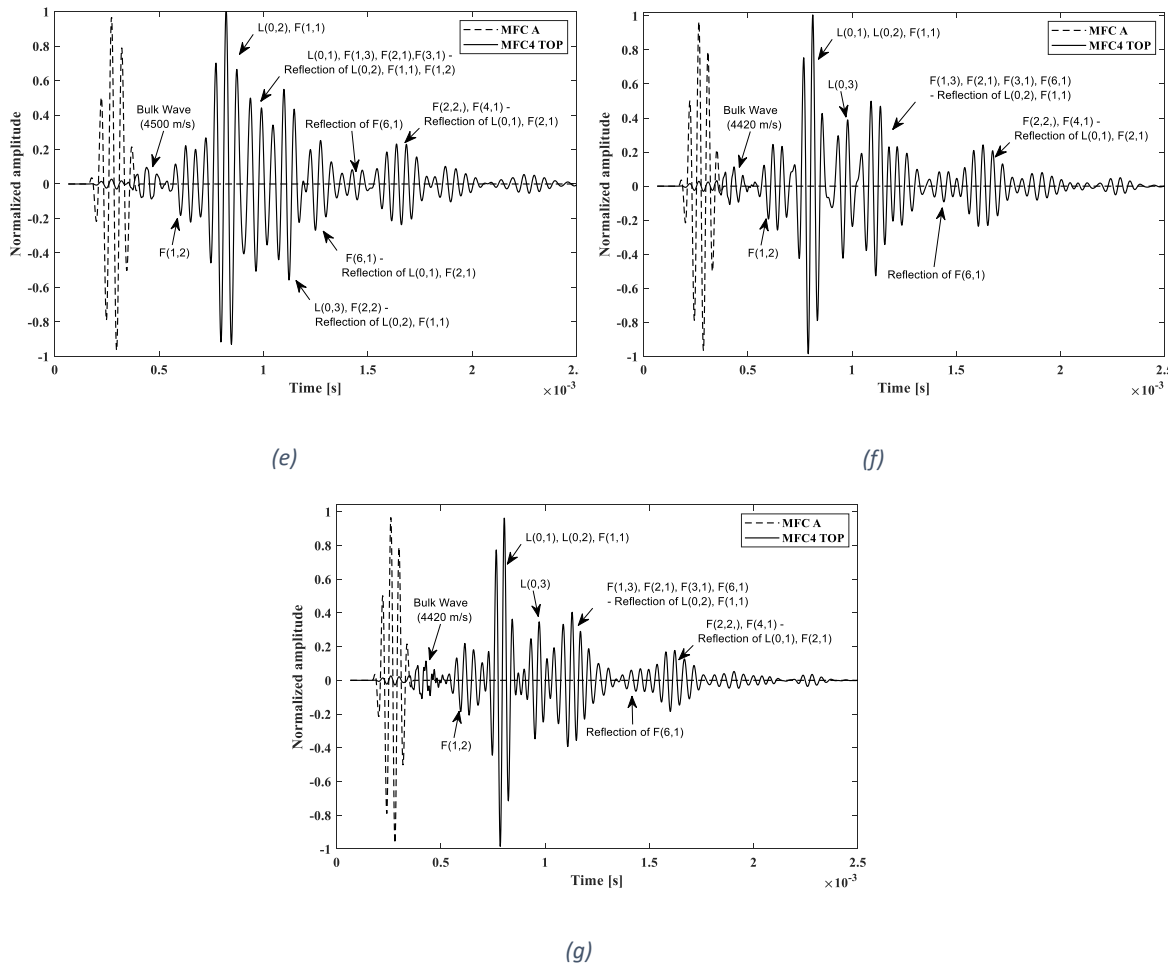


Figure 3.36 Experimental results: MFC4 TOP acquired signal using single MFC actuation at (a) 10 kHz, (b) 12.5 kHz, (c) 15 kHz, (d) 17.5 kHz, (e) 20 kHz, (f) 22.5 kHz and (g) 25 kHz.

### 3.4.2. MFC – Timber Matching (Experimental)

After performing frequency tuning using single actuation, an important experiment must be conducted to examine the MFC-wood impedance matching. This step is done before actuating several transducers around the circumference, to detect if all the MFCs around the circumference are generating the same wave when actuated. The experiment is done by coupling piezoelectric transducers of type PZT-5H in front of each MFC on the

circumference. The MFCs are actuated one by one at a time where the signal is measured using the PZT coupled in front it. Figure 3.37 shows the experimental configuration.



*Figure 3.37 MFC – Timber impedance matching experiment.*

Each PZT is labeled according to its position (TOP, LEFT 1, LEFT 2, etc.). Each MFC is actuated with a 5-cycle burst, where the PZT in front of it is measured in each of the eight locations. Figure 3.38 shows the signals acquired from the PZTs for an excitation frequency of 12.5 kHz.

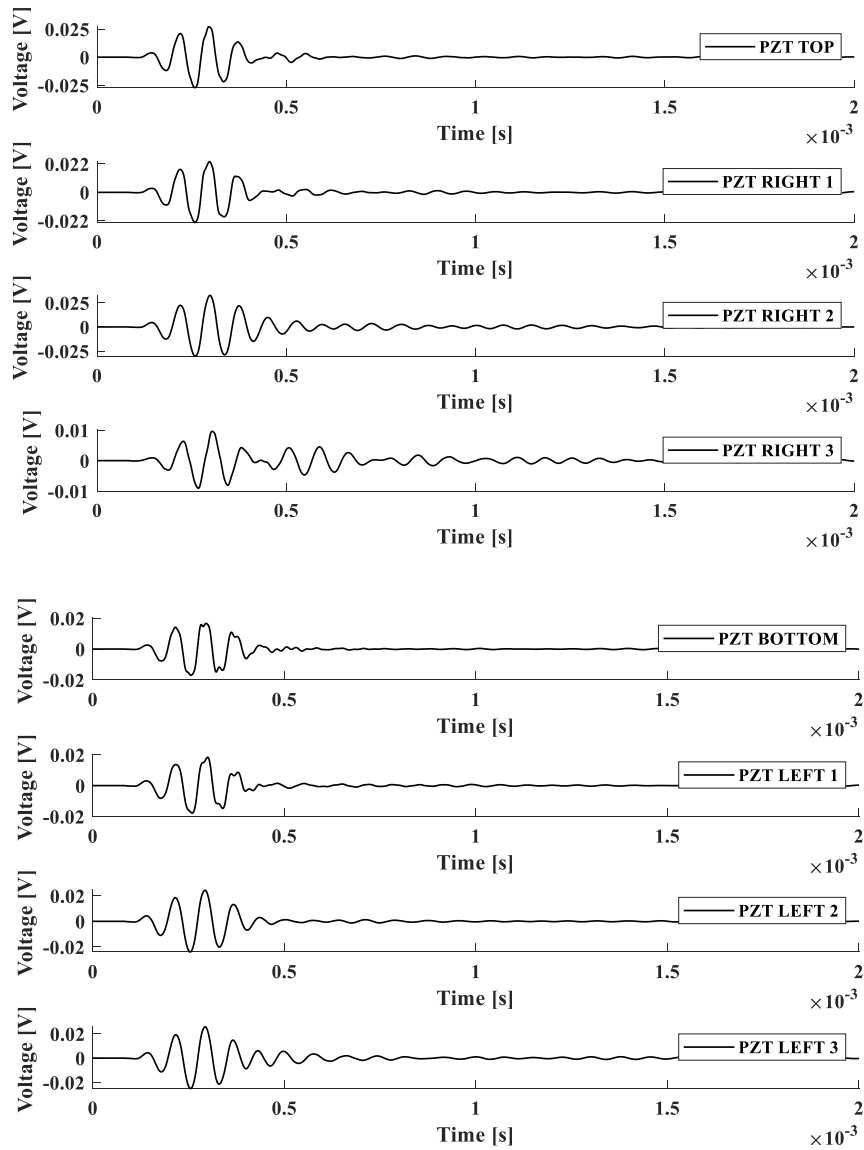


Figure 3.38 Acquired signals from the PZTs after actuating each subsequent MFC at 12.5kHz.

What can be noticed from this experiment is the variation in the acquired signals. This is due to several reasons such as the presence of knots in front of some of the actuated MFCs. For instance, PZTs located at the TOP, RIGHT 1, RIGHT 2, LEFT 1, LEFT 2 and LEFT 3 show almost the same signal which indicates that all the subsequent MFCs are

generating the same wave. On the other hand, for the PZT RIGHT 2 and PZT BOTTOM there is a significant difference. The presence of a crack on the lower surface where the MFC-PZT are located (BOTTOM) lead to the distortion of the signal acquired. Also, PZT RIGHT 3 acquires a delayed signal and a reflection as shown Figure 3.38 above with a lower amplitude than the rest of the sensors. The reason is that a knot is present between the MFC and PZT RIGHT 3 which is displayed in Figure 3.39. The knot caused the propagating wave to delay, in addition to a reflection at the edge of the same propagating wave.



*Figure 3.39 Presence of knot between MFC1 R3 and PZT R3.*

The difference in the generating signals from the MFC actuators might affect the propagating signal, especially when all 8 MFCs are actuated to induce non-axisymmetric mode suppression.

### **3.4.3. Reducing the Effects of Dispersion (Experimental)**

The numerical and experimental testing were only conducted using a 5-cycle input burst. However, it was mentioned earlier in the dispersion section that increasing the number of cycles decreases the effect of dispersion significantly due to the smaller frequency range in the signal. For this reason, an experimental analysis was performed to investigate the effect of increasing the number of cycles from five to ten. Figure 3.40 (a) shows an acquired signal from MFC3 TOP during the single actuation configuration using a 5-cycle input at 12.5 kHz. A dispersive reflected packet appears between times 1E-3 and 1.5E-3 seconds where the shape of the packet changes dramatically. This could disrupt the interpretation of the signals and lead to an un-accurate result. Figure 3.40 (b) shows the acquired signal for the same configuration but using a 10-cycle input burst. The same reflected packet is shown but with a completely non-dispersive structure. The 10 peaks indicate the arrival of a single-mode reflection from one of the ends. Therefore, the effect of increasing the number of cycles on dispersive packets is confirmed.



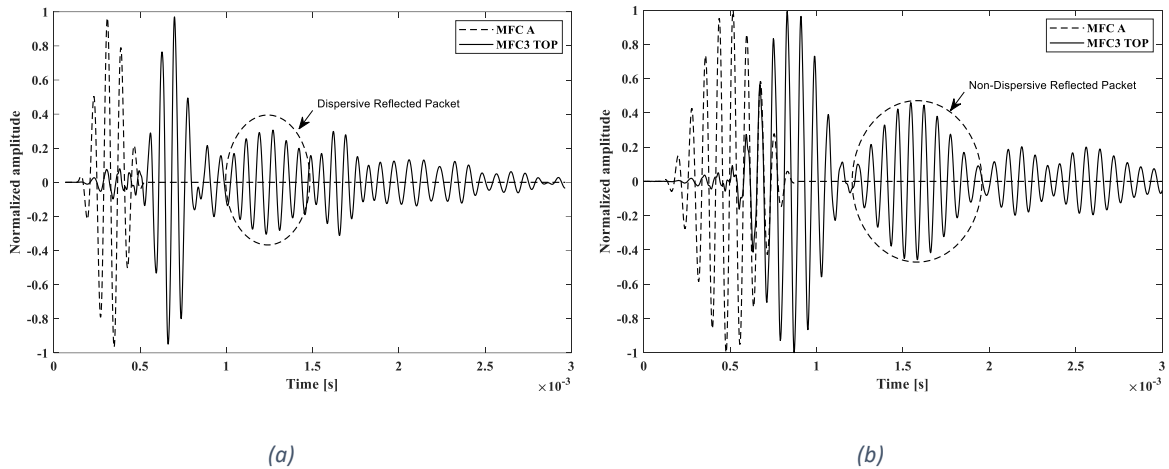


Figure 3.40 Experimental results: Acquired signals from MFC3 TOP sensor using single MFC actuation for a (a) 5-cycle and (b) 10-cycle tone burst at 12.5 kHz.

At frequencies where multiple wave modes propagate at close velocities the effect of increasing the number of cycles might affect the signal. Consider the same procedure as above where a single MFC is excited at 15 kHz and acquired by MFC3 TOP represented in Figure 3.41. The effect of increasing the number of cycles is clearly shown where the reflected packet after time 1.5E-3 seconds is shown to be dispersive in the 5-cycle burst. However, in the 10-cycle the packet does not show signs of dispersion. However, in the signal acquired from the 5-cycle, two separated packets are shown after 1E-3 for two different arrivals. These packets are combined in the 10-cycle input due to the additional number of cycles and appear as one packet. Therefore, caution must be taken when actuating with a 10-cycle burst to prevent the misinterpretation of the data. For the rest of the experiments and numerical testing, only the 5-cycle tone burst was used to avoid complication of the acquired signals. The results for both 5-cycle and 10-cycle input at 15 kHz bursts are shown below.

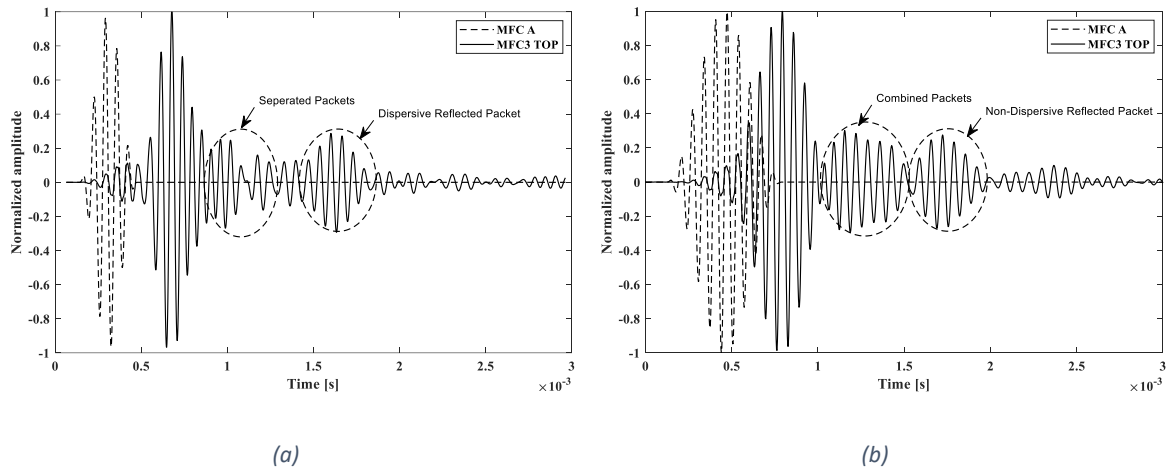


Figure 3.41 Experimental results: Acquired signals from MFC3 TOP sensor using single MFC actuation for a (a) 5-cycle and (b) 10-cycle tone burst at 15 kHz.

### 3.4.4. Ring Design

Actuating multiple MFCs around the circumference of the pole provides significant improvement in the behavior of guided waves. As mentioned in the above sections, at 12.5 kHz excitation frequency there exist flexural modes of high order  $F(4,m)$  that require the excitation of at least 4 MFCs in the ring. The results for three different actuation configurations corresponding of single, 4-ring and 8-ring MFC actuation are portrayed in this section for both numerical and experimental setups for the 1-meter length pole. Acquired raw data (in voltage) are from the sensor placed 75 cm away from the actuator (MFC4 sensor).

#### a) Numerical results

Results from the numerical model of the ring design are presented in this section. Figure 3.42 shows the raw data acquired from MFC 4 sensor for (a) single, (b) 4-ring and

(c) 8-ring MFC actuation at 12.5 kHz excitation frequency. The group velocity of the modes of interest was calculated for each major wave packet in the signal by extracting the time of flight, and using the distance between the actuator and sensor which is known to be 0.75 cm. The wave modes were identified from their group velocities in the dispersion curves generated from DISPERSE [53]. The signals acquired from the sensor at different actuation configurations clearly indicate the suppression of non-axisymmetric (flexural) modes. Also, other modes are shown to be enhanced when actuating multiple MFCs where the acquired voltage increased significantly by almost 25% in the 4-ring and 83% in the 8-ring MFC actuation.

The application of actuator ring is observed to have significant effects on the behavior of propagating wave modes in Figure 3.42, where the arrival of flexural modes was suppressed. In the single and 4-ring MFC actuation, flexural wave modes  $F(1,1)$  and  $F(1,2)$  arrive between  $1E-3$  and  $2E-3$  seconds traveling around 1240 m/s. Flexural mode  $F(3,1)$  appears at  $1.6E-3$  seconds, in addition to  $F(4,1)$  at  $2E-3$  seconds traveling at 1220 m/s and 1182 m/s speed. Longitudinal modes  $L(0,1)$  and  $L(0,2)$  arrive right before  $1E-3$  seconds propagating at 1400 m/s and 1300 m/s respectively. The amplitude of longitudinal modes is enhanced as the number of actuators around the circumference increase as shown in the 4 and 8 ring configurations. The generated voltage from sensor MFC 4 increases from 120 mV in the single actuation to around 220 mV in the 8-ring actuation. The flexural waves were cancelled in the 8-ring actuation only, and this is mainly due to the circumferential order as mentioned in the above sections. At 12.5 kHz, the highest circumferential order of flexural waves is 4 in  $F(4,m)$ , meaning that a minimum number of 4 transducers around the circumference are needed for the elimination to occur. However,

the actuation of 4 MFCs does not prove to have any effect on the propagating flexural modes. They are rather cancelled by actuating 8 MFCs only as shown above.

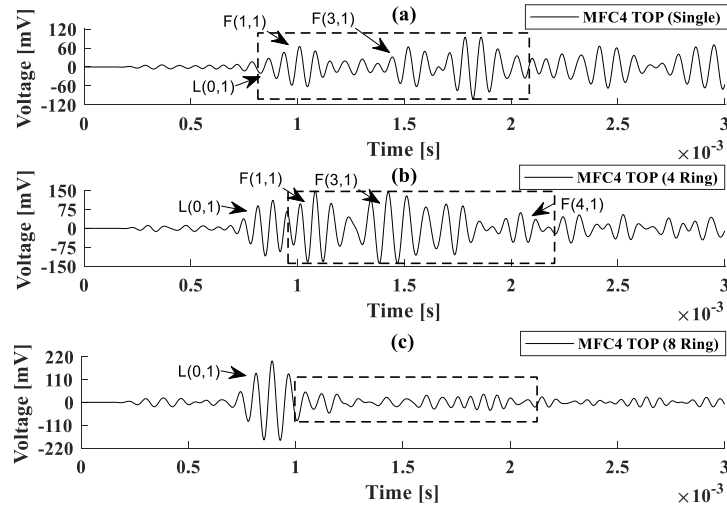


Figure 3.42 Raw numerical data collected using MFC4 sensor for (a) single, (b) 4-Ring and (c) 8-Ring actuation at 12.5kHz frequency.

The propagation of waves generated from the actuator in COMSOL can be visualized by plotting the surface x-velocity component (mm/s) for the timber specimen. Non-axisymmetric mode suppression can be identified by actuating multiple transducers around the circumference of the pole. Figure 3.43 displays snapshots of the surface x-velocity at different times for (a) single, (b) 4-ring and (c) 8-ring configuration at 12.5 kHz excitation frequency.

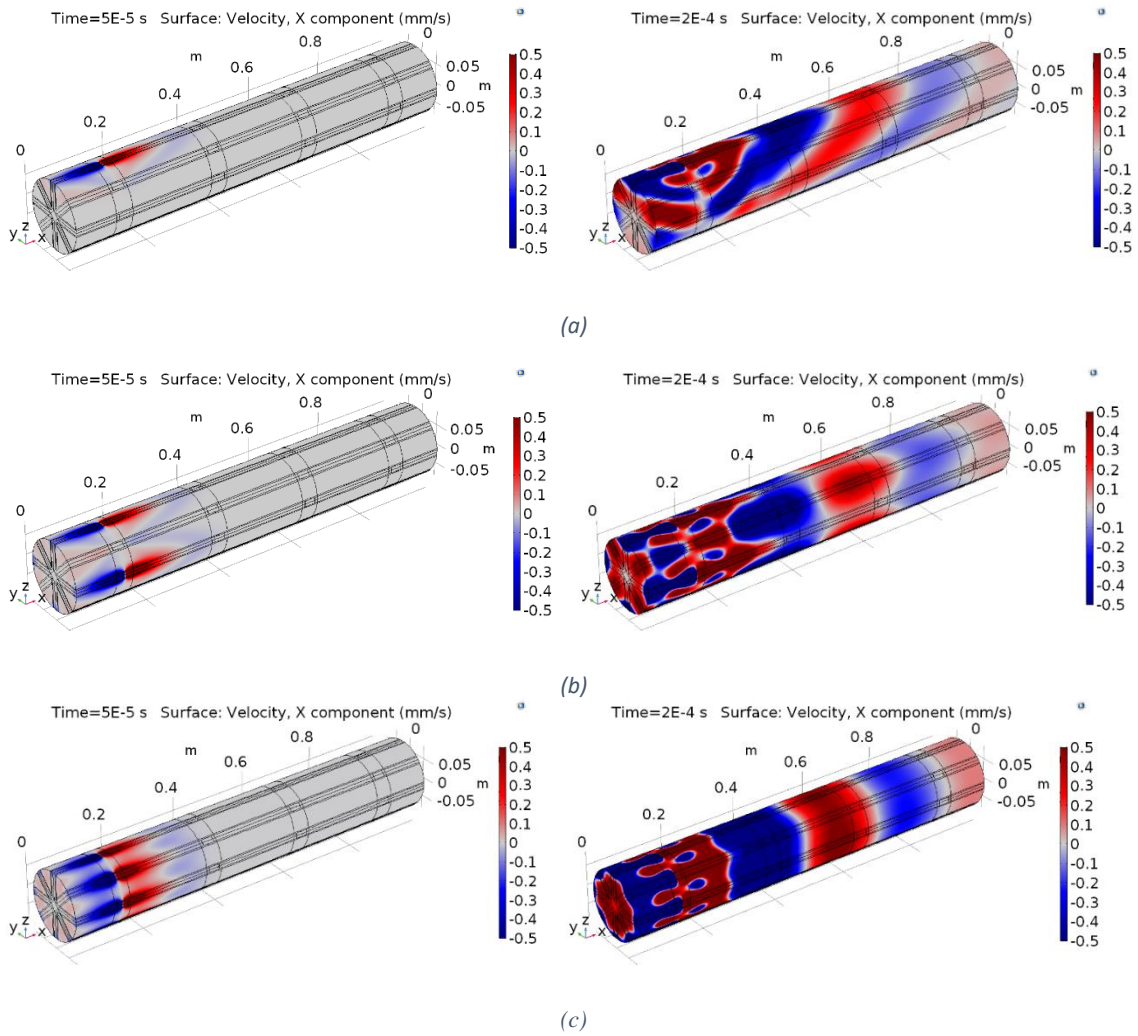


Figure 3.43 Surface x-velocity component for at different times for (a) single, (b) 4-Ring and (c) 8-Ring MFC actuation in COMSOL.

The x-velocity component in the single actuation (Figure 3.43 (a)) appears to start from the actuator in both directions. As the waves propagate, they wrap the cylinder in all directions which induces the conversion of non-axisymmetric modes. In the 4 and 8 ring actuations, the waves appear to propagate all-together from the actuation point, enhancing the conversion of pure longitudinal waves with less (or without) flexural wave modes.

## b) Experimental results

The numerical simulations in COMSOL were performed on a perfectly-sound timber specimen, which makes the acquired signals and analysis much less complicated. However, in the experimental setup, the natural timber specimen contains a significant number of small cracks and knots present at different locations. This can cause reflections and complicate the signals even further. The acquired data from the experimental setup confirms the suppression of flexural wave modes, and an enhancement of 25% (4-ring) and 63% (8-ring) in the amplitude of the propagating longitudinal wave modes when actuating the MFC ring. In addition, the MFCs exhibit promising results when actuating and sensing guided waves along the timber specimen. The raw data acquired from MFC 4 sensor is shown in Figure 3.44 for (a) single, (b) 4-ring and (c) 8-ring MFC actuation at 12.5 kHz.

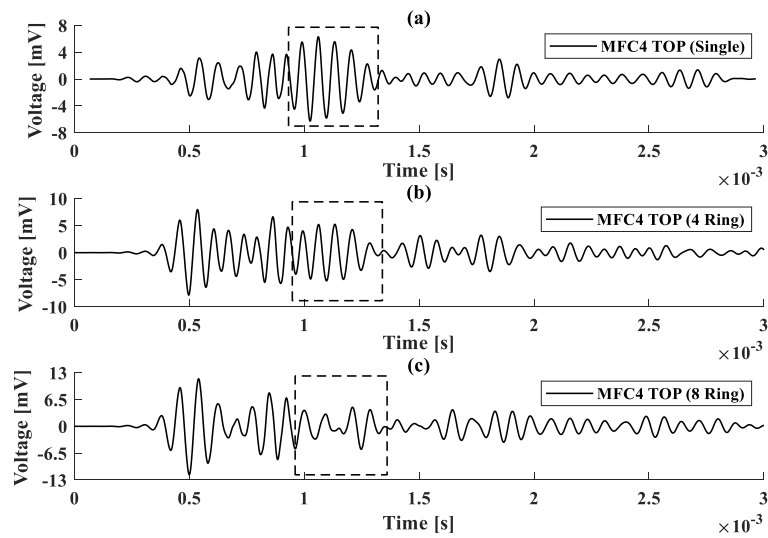


Figure 3.44 Raw experimental data collected using MFC4 sensor for (a) single, (b) 4-Ring and (c) 8-Ring actuation at 12.5kHz frequency.

The same procedure was performed for the experimental results acquired. The group velocity of each packet is calculated, and the wave mode type is identified from the dispersion curves. Figure 3.45 shows the analysis of the above acquired signals, indicating the propagating wave modes in each actuation configuration. It can be noted that the effect of ring is proven successful in both numerical and experimental tests. The propagating wave modes present in the numerical results are also determined in the experimental ones, with minor difference in velocities due to computational error and the fact that the timber pole modeled in COMSOL is perfectly sound.

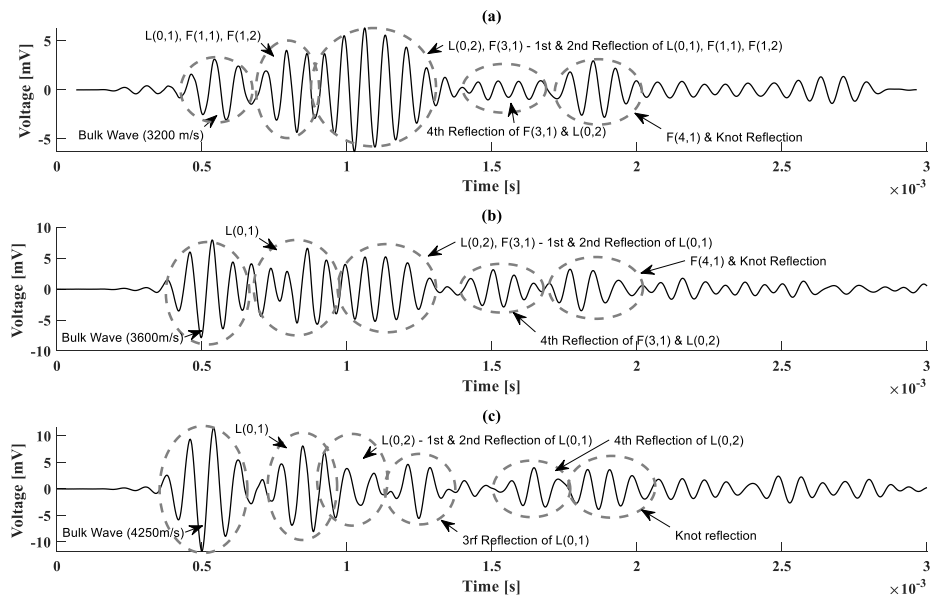


Figure 3.45 Analysis for the collected data from MFC 4 sensor at 12.5 kHz for (a) single, (b) 4-Ring and (c) 8-Ring MFC actuation in the experimental setup.

It can be shown that the first peak of each configuration is of high speed (3200 – 4250 m/s) which indicates the propagation of a pure bulk wave with a speed similar to the speed of sound in wood. The bulk wave appears in low amplitude in the single actuation as

shown in Figure 3.45 (a). As the number of actuators around the circumference increase, the amplitude of the bulk wave increases in addition to the increase in the propagating velocity. This increase could imply that the wave generated from the single MFC actuation travels a longer path than the distance between the actuator and the sensor (75 cm). Meaning that the presence of cracks and knots affects the propagation of the bulk wave. Examining the rest of the acquired signal, in the single actuation (a), modes L(0,1), F(1,1) and F(1,2) appear to propagate at a group speed of 1300 m/s between times 0.5E-3 and 1E-3 seconds. The first and second reflections of these modes traveling 100 cm (each reflection) appear around time 1E-3. The high amplitude of this packet is due to the addition of the first arrival of modes L(0,2) and F(3,1) with speed of 1050 m/s respectively. For the 4-ring actuation in (b), L(0,1) seems to arrive solely before 1E-3 seconds traveling at around 1300 m/s. L(0,2) and F(3,1) first arrival are also concatenated with the reflection of L(0,1) mode right after the time 1E-3 seconds. This indicates that the flexural modes are not yet cancelled with the 4-ring configuration where the highest order of non-axisymmetric modes is 4 at this frequency. At 1.5E-3 seconds, the 4<sup>th</sup> arrival of L(0,2) and F(3,1) remains similar to the single actuation, along with the arrival of F(4,1) and the knot reflection before time 2E-3 seconds. Last, in the 8-ring actuation (c) the number of transducers is significantly higher than the circumferential order where none of the flexural modes appear to propagate. L(0,1) propagates solely at 1300 m/s and arrives before 1E-3 seconds with a higher amplitude than the previous configurations. Mode L(0,2) arrives at 1E-3 with the second arrival of L(0,1). The latter is followed by the third reflection of L(0,1) between 1E-3 and 1.5E-3 seconds. The 4<sup>th</sup> reflection of L(0,2) is right after 1.5E-3



seconds, in addition to the knot reflection that remains with a lower amplitude before  $2E-3$  seconds.

### **3.4.5. Validation of the Ring Design and Effect of Boundary Conditions**

The validation process was performed numerically and experimentally on a 5.5-meter (numerically) and 8-meter (experimentally) timber pole where the selected excitation frequency was 12.5 kHz as mentioned previously. Additionally, multiple MFC configurations were actuated which correspond of single, 4-ring and 8-ring actuation. These configurations were applied separately to depict the effect of change in boundary conditions for traction free and embedded models.

Propagating wave modes were characterized by their group velocity in the numerical and experimental signals acquired. Results from single MFC actuation at 12.5kHz, traction free model, are displayed in Figure 3.46 for numerical model (a) and experimental setup (b). It can be seen that the propagating modes are similar in both results. The propagation velocity varies due to computational error, slightly different mechanical properties of timber used in the numerical model and the presence of knots and cracks in the experimental timber specimen. A bulk wave propagates at 5000 m/s as seen in both results, with significantly lower amplitude than other packets. Flexural modes F(1,1) and F(1,2) propagate at 2540 m/s and 1429 m/s in the numerical models. However, the velocities are slightly higher in the experimental results where they propagate at 2797 m/s and 1768 m/s respectively. The longitudinal modes L(0,1) and L(0,2) propagate at 980 m/s and 780 m/s in the numerical, compared to 1140 m/s and 845 m/s in the experimental

results. Flexural modes of higher order such as F(3,1) and F(4,1) propagate in the numerical model at 1220 m/s and 625 m/s respectively. In the experimental results, F(3,1) propagates at nearly 1300 m/s and arrivals right after F(1,2). The identification of edge reflections is presented in the subsequent sections.

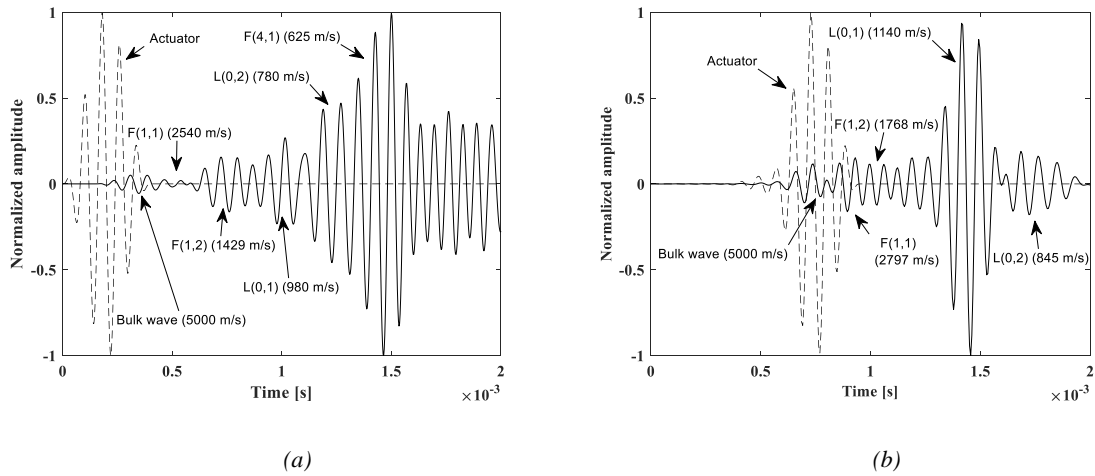


Figure 3.46 Acquired signals (normalized) for traction free/embedded sound timber, single MFC actuation at 12.5 kHz in (a) numerical model and (b) experimental setup.

Soil was added to a section of the timber pole to simulate the embedded condition both numerically and experimentally to study the effect of damping and wave attenuation. Similar to the experimental results shown in the Signal Processing section, the numerical results acquired were also decomposed using the CEEMD signal processing technique, providing a better understanding of the difference between the two boundary conditions. From the original numerical data seen in Figure 3.47 (a), the reflections from the propagating wave modes appear to have slightly higher amplitudes in the embedded boundary condition compared to the traction free one. This means that not only the wave is

contained inside the pole in the embedded condition, but also there is less leakage in soil than in air. Packets arriving at times  $4\text{E-}3$ ,  $4.65\text{E-}3$  and  $5.2\text{E-}3$  seconds have a higher amplitude in the embedded condition. After using CEEMD, the first mode (IMF 1) shown in Figure 3.47 (b) is almost the same in the two boundary conditions except at time  $5.2\text{E-}3$ . This packet has a significantly higher amplitude in the embedded condition and is determined clearly by the decomposition process. Furthermore, in the rest of the decomposed modes (IMFS) the packets in the embedded condition also appear to have a higher amplitude than in the traction free one. Identifying the propagating wave modes and their reflections from their group velocities can be performed on the original signals directly. Direct and reflected packets from single MFC actuation at 12.5 kHz were identified one by one and are shown in Figure 3.47 (a), for both traction free and embedded conditions. The bulk wave propagates at 5000 m/s and arrives at the beginning of the signal, with its reflections from both ends of the pole present at around  $1\text{E-}3$  and  $2\text{E-}3$  seconds. This bulk wave appears to be non-dispersive where the 5-peak packet maintains its shape as shown in the first and second arrival of the wave, with no change in the frequency components. Flexural modes propagate at 2540 m/s and 1429 m/s indicating  $F(1,1)$  and  $F(1,2)$ . Their reflections arrive at  $2\text{E-}3$  and  $3\text{E-}3$  from the bottom of the pole.  $F(1,1)$ 's second reflection from the top end arrives right before  $4\text{E-}3$  seconds. Also, flexural mode  $F(4,1)$  of order 4 propagates at 625 m/s. The rest of the high order flexural modes are not indicated in the figure for simplification purposes. Nevertheless, longitudinal modes  $L(0,1)$ ,  $L(0,2)$  and  $L(0,3)$  propagate at 980 m/s, 780 m/s and 508 m/s, respectively. Their reflections are also indicated in the figure, where  $L(0,1)$  and  $L(0,2)$  arrive at  $4\text{E-}4$  and  $4.5\text{E-}3$  seconds. The 5.5-meter pole and the distance between the actuator and sensor provide

enough distance for the waves to converge, which results in the propagation of various modes with different type and orders. As for the effect of soil embedment, no significant effect on flexural modes' first reflections is shown. However, for the second reflection of F(1,1) and first reflection of L(0,1) and L(0,2), there is a notable increase in the packet's amplitude in the embedded condition.

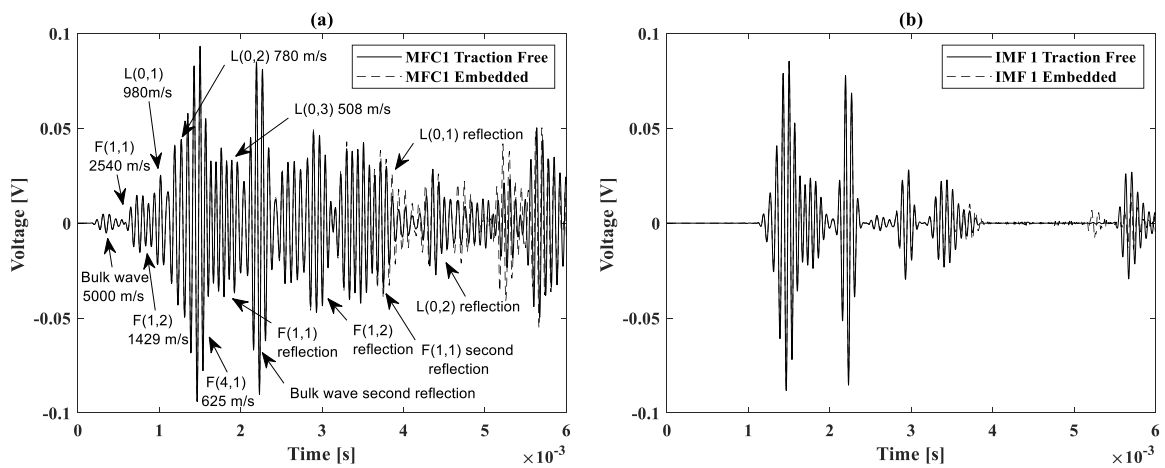


Figure 3.47 Numerical results: Traction free (solid) and embedded (dashed) using single MFC actuation at 12.5kHz

(a) original signal and (b) decomposed signal after CEEMD (IMF 1).

Similarly, the acquired signals from the experimental traction free and embedded boundary conditions were placed above each other and decomposed to examine the difference. The original signal and decomposed modes (IMFs) were shown previously in Figure 3.33 (signal processing section). Embedding the section of the pole did not have significant effects on the reflecting packets, but rather the waves were confined within the medium with minimal leakage. In some reflected packets, such as the one shown at time 3.2E-3 seconds in Figure 3.33 (d), the amplitude slightly increases in the embedded

compared to the traction free boundary condition. Wave mode identification can be performed on the original signals (embedded and traction free) as mentioned and are shown in Figure 3.48 for single MFC actuation at 12.5 kHz. It can be shown that all propagating modes are the same in traction free and embedded signals. The first arrival of flexural and longitudinal modes was depicted in the previous section from Figure 3.46. Longitudinal mode L(0,3) arrives right after  $2\text{E-}3$  seconds, propagating at 540 m/s. Additionally, reflections of modes F(1,1) and F(1,2) from the bottom edge of the pole arrive between  $2\text{E-}3$  and  $3\text{E-}3$  seconds. The reflections of L(0,1) and L(0,2) arrive roughly at  $4\text{E-}3$  and  $5.2\text{E-}3$  seconds from the bottom edge. The reflections of all propagating modes from the pole's bottom edge can be shown clearly. Furthermore, F(1,2) and L(0,2) reflect from a knot present at 1.2 meters to the left of the actuator, which appear in the packets at  $2.6\text{E-}3$  and  $3.65\text{E-}3$  seconds. The reflected packets from the knot travel a total distance of 3.2 meters. The effect of soil embedment appears only on the reflection of mode F(1,1) as shown in Figure 3.48, where the packet has a lower amplitude in the embedded condition. However, the rest of the modes reflected are not affected by the addition of soil, which indicates that they are confined in the timber medium with no attenuation and leakage to the outer soil medium.

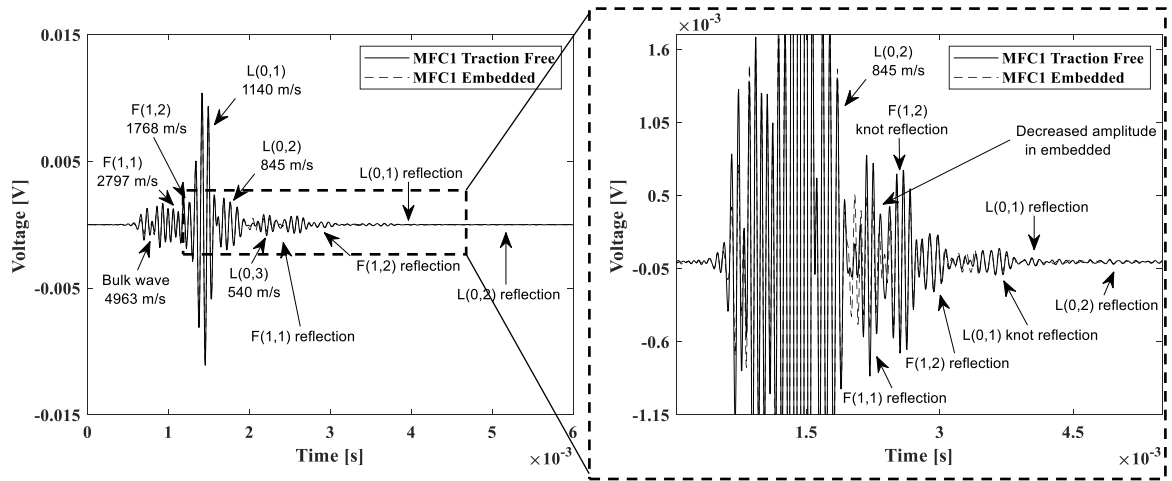


Figure 3.48 Experimental results: Propagating wave modes and their reflections–traction free/embedded signals, using single MFC actuation at 12.5 kHz.

Evaluating the health condition of the timber pole (estimating embedded length, damage detection, etc.) requires capturing and analyzing the first and reflected arrival of a certain (selected) wave mode. Several modes propagate at 12.5 kHz frequency as shown in the numerical and experimental results, where each identified reflected packet can be used for the evaluation process. However, some modes are more sensitive than others with respect to the boundary conditions present, knots and cracks in the structure and the configuration of MFC actuation. Since flexural modes are unwanted due to their complexity and the presence high order modes, the MFC ring actuation can cancel them out and simultaneously enhance the propagating longitudinal modes and their reflections. The enhanced modes can be used for a more adequate evaluation process.

Signals acquired from actuating 4 MFCs around the circumference of the pole are shown below for traction free and embedded boundary conditions. Results from the numerical model (Figure 3.49) confirm that the actuation of multiple MFCs enhances the

acquired packets in general, whether they were flexural (unsuppressed) or longitudinal wave modes. For instance, the amplitude of the direct transmission of bulk wave, L(0,1), L(0,2) and L(0,3) is higher than the ones in single MFC actuation. Also, L(0,1) amplitude increases by around 60%, as well as the reflection's amplitude of mode L(0,1) is enhanced in the 4-ring actuation by 58 %. Additionally, flexural modes F(1,1) and F(1,2) do not appear to propagate, however F(4,1) propagates at 630 m/s which means that the 4-ring MFC actuation did not suppress the high order flexural modes. The propagating wave modes and their velocities are indicated in Figure 3.49.

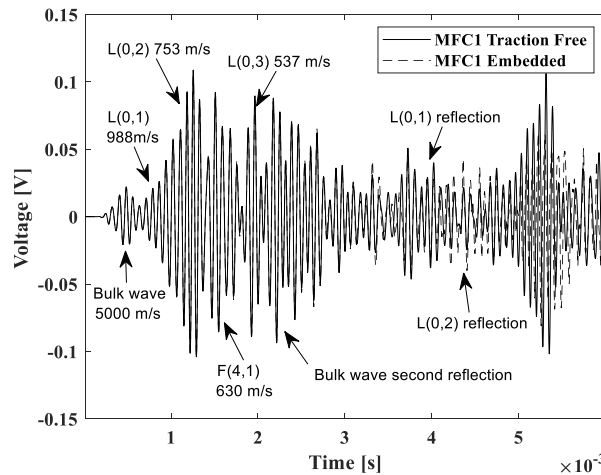


Figure 3.49 Numerical results: Propagating wave modes and their reflections for traction free/embedded signals using 4-Ring MFC actuation at 12.5 kHz.

Comparing the traction free and embedded signals, no significant difference can be identified as the single MFC actuation. When actuating 4 MFCs around the circumference, the complete signal is enhanced where the waves have a higher amplitude. This decreases the effect of external boundary conditions (soil/air) with respect to the longitudinal modes'

reflections. However, mode L(0,2) was the most affected by the soil embedment where it had a slightly higher amplitude than the traction free condition. Reflection of longitudinal mode L(0,1) had the same amplitude in the two boundary conditions.

In the experimental testing, the 4-MFC actuation also yields similar results as the numerical where the complete signal was enhanced compared to the single MFC actuation. Figure 3.50 shows the acquired signal for both traction free and embedded conditions. The bulk wave, L(0,1), and L(0,2) attained higher amplitudes than the single MFC actuation. The direct transmission enhancement of the longitudinal modes is around 30 %, whereas the reflection enhancement is 80%. Regarding the suppression of flexural modes, F(1,2) is suppressed after 1E-3 seconds. However, F(1,1) arrives at 1E-3 seconds and was not damped by the 4-ring actuation. The reflection's amplitude of F(1,1) was also slightly higher than the single actuation. The propagating wave modes and their velocities, along with their reflections are shown in Figure 3.50. L(0,1) reflects from a knot present on the right side of the timber pole, 0.8 meter far from the actuator ring (towards top edge of pole). The knot is located on the same straight line as one of the MFC actuators in the ring, placed at a 90-degree angle. This explains why the reflected packet only appears in the ring actuation, and not in the single MFC actuation discussed previously. Figure 3.50 displays all the propagating wave modes' velocities and reflections. The velocities are almost similar to the single MFC actuation configuration. The acquired signals are almost entirely similar for traction free and embedded conditions. Decomposing the signal shows that only mode F(1,1) is affected by the soil where its reflection from the bottom edge is slightly increased in the embedded condition.



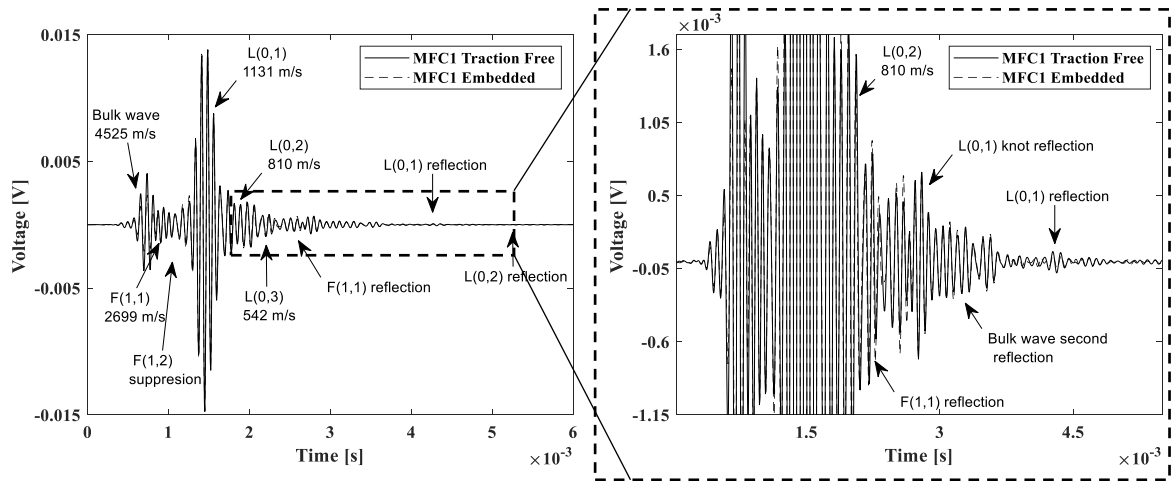


Figure 3.50 Experimental results: Propagating wave modes and their reflections– traction free/embedded signals, using 4-Ring MFC actuation at 12.5 kHz.

As mentioned, not all flexural modes were suppressed in the 4-ring MFC actuation. This could be due to the presence of high order modes like F(4,1) propagating at 12.5 kHz frequency. However, the numerical results acquired from actuating 8 MFCs in the ring confirm the suppression of all flexural modes present at 12.5 kHz. Figure 3.51 shows that F(1,1), F(1,2) and F(4,1) are not acquired from the sensor. Rather, only longitudinal modes and the bulk wave propagate with an enhanced amplitude. The direct transmission's amplitude of longitudinal modes increases by 60 % compared to the single MFC actuation. Reflection's amplitude of L(0,1) also increases by around 63 %, which is higher than the 4-ring actuation.

In the embedded boundary condition, L(0,1) gains a higher amplitude than in the traction free condition. The rest of the signal confirms that the 8-ring MFC actuation enhances the entire signal, causing no significant difference between the two boundary

conditions. The waves are maintained within the timber pole with negligible leakage to the surrounding medium.

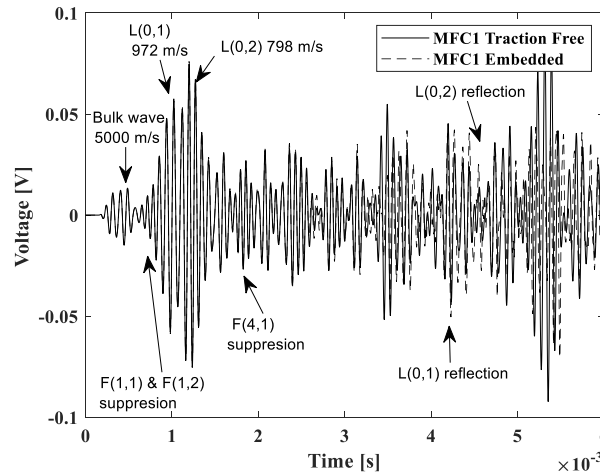


Figure 3.51 Numerical results: Propagating wave modes and their reflections– traction free/embedded signals using, 8-Ring MFC actuation at 12.5 kHz.

Similarly, for the 8-ring MFC actuation in the experimental setup, the flexural modes of all orders were cancelled out. The acquired signal from the setup is shown Figure 3.52, indicating the times where F(1,1) and F(1,2) are suppressed. The bulk wave's amplitude is enhanced by more than 80 % compared to the single MFC actuation experimental setup. Longitudinal modes enhancement is similar to the 4-ring actuation, with around 30 % increase in amplitude compared to the single actuation. The reflection of L(0,1) from the same knot as in the 4-ring appears at a higher amplitude and is indicated in the zoomed-in section of the signal shown in Figure 3.52. As for the reflection of L(0,1) from the pole's bottom edge, the amplitude increases by 93 % compared to the single actuation configuration.

The effect of soil embedment also seems negligible in the experimental 8-ring actuation, similar to the previous results acquired numerically. The reflection of bulk wave at 3.2E-3 seconds has a slightly higher amplitude in the embedded condition. However, the rest of the reflections seem to be similar with respect to time and amplitude of the packets in both embedded and traction free boundary conditions.

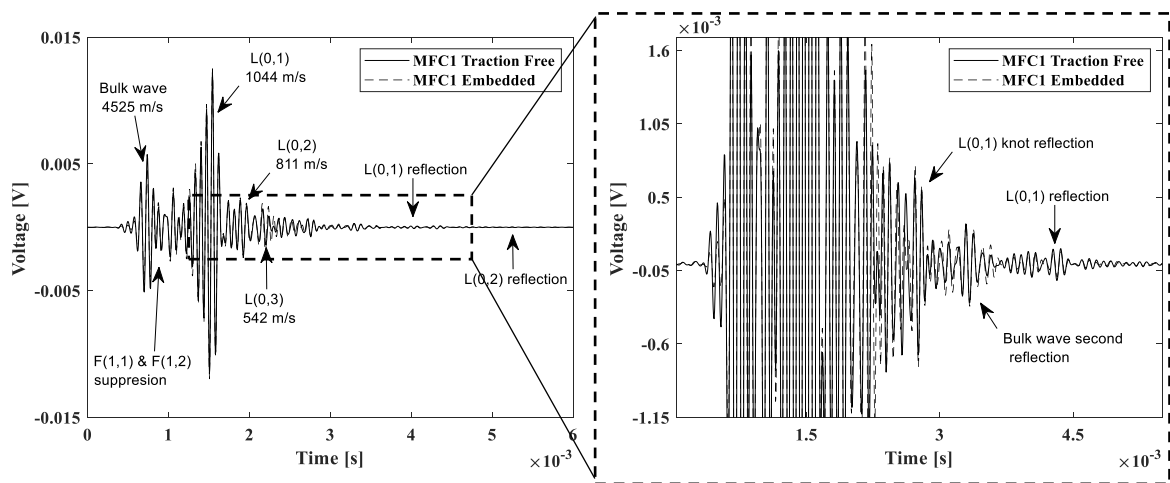


Figure 3.52 Experimental results: Propagating wave modes and their reflections– traction free/embedded signals, using 8-Ring MFC actuation at 12.5 kHz.

### 3.5. Discussion

A detailed inspection of guided wave propagation in timber structures was depicted in this work. Macro Fiber Composites (MFCs) have proved to be efficient for generating/sensing guided stress waves in timber poles, and reliable due to their flexibility and ability to be coupled on curved- rough surfaces. Primarily, the solution of the wave equation was solved analytically using DISPERSE software which generated the dispersion

curves for transversely isotropic circular timber, showing the possible propagating wave modes at different excitation frequencies.

The effect of MFC actuator ring coupled around the circumference of the pole was then tested numerically and experimentally on a 1-meter timber specimen, before being validated on an 8-meter length timber utility pole. The application of MFC ring proved to eliminate unwanted wave modes and enhance the amplitude of propagating longitudinal modes (direct transmission) and their reflections, which could be extremely crucial for evaluating the health state of the timber pole, especially with the variation of boundary conditions. The actuation of 4 MFCs in the ring enhanced the amplitude of the direct transmission by around 25% but did not fully eliminate the propagation of flexural modes, specifically modes F(1,1) and F(3,1). However, actuating 8 MFCs in the ring was able to completely suppress all flexural modes, in addition to enhancing the amplitude by 83% and 63% in the numerical model and experimental setup.

Furthermore, the effect of change in boundary conditions was investigated numerically and experimentally for traction free and soil embedment. It was found that the timber – soil interface slightly affects the propagation behavior of GWs, especially with respect to the reflected amplitudes and propagation velocities. In some cases, the embedded condition yielded higher amplitudes of reflected waves than the traction free one. As for the propagation velocities, some wave modes (such as longitudinal mode L(0,2)) were affected in the embedded condition where they had a slightly lower velocity than in the traction free boundary condition. These velocities were less affected in the MFC ring actuation than the single actuation configuration. The most accurate results with respect to calculating the reflection's velocity was achieved in the 4-ring actuation, followed by the 8-ring and the

single MFC actuation. The reason the 4-ring performed better than the 8-ring may be due to the presence of several knots in the timber pole, which created more reflections when actuating 8 MFCs in the ring that interfere with the bottom edge reflections. Nevertheless, when evaluating the conditions of the pole whether for embedded depth estimation or decay detection, the differences in the velocities and amplitudes in both boundary conditions can be considered negligible.

# **Chapter 4 Condition Assessment and Damage Detection in Timber Utility Poles using Guided Waves**

## **4.1. Introduction**

Timber is famously known in the electric power distribution industry, serving as utility poles for supply lines. These poles support overhead power lines, electrical cables and other utility equipment where the timber serves as perfect insulator. Also, embedding the poles into the ground is a lot easier than other materials [3]. Besides utility poles, the use of timber in the construction industry has been undergone for decades. The long service life of 40 to 80 years [54] with low production costs proves that it can act as a replacement for other materials. To maintain the health of timber poles and ensure their safety and reliability in any application, evaluation practices must be conducted to determine if damage has occurred during its life cycle. In addition to damages, natural defects/decays such as rots, termites and fungi can affect the overall health condition of the pole and require appropriate assessment and treatment [4]. The lack of information in most in-service timber utility poles such as the embedment depth, can cause additional maintenance costs and require to be determined by non-destructive testing (NDT) techniques.

In this study, guided waves have been used for the assessment of timber poles experimentally and numerically using COMSOL Multiphysics. Important features such as the embedded length and the health state of the timber pole has been evaluated by the means of Macro Fiber Composites (MFCs) [49]. The application of an MFC-ring assisted in the generation of purely longitudinal wave modes, such as mode  $L(0,1)$ , which were used in the evaluation process. The excitation frequency was selected according to a set of

factors such as the number of propagating wave modes, dispersion and the number of MFCs required in the actuator ring. The effect of change in boundary conditions (traction free and soil embedment) on the length estimation and damage assessment was also investigated.

## **4.2. Methodology**

### **4.2.1. Numerical FEA Model**

The evaluation of embedded length and health state of a timber pole was scrutinized numerically by examining the propagation of guided waves in traction free and embedded boundary conditions. COMSOL Multiphysics [39] is a powerful tool for the finite element modeling of piezoelectric transducers generating guided waves in structures. The Piezoelectric Devices module is composed of two physics, Solid Mechanics and Electrostatics where each component in the study can be modelled separately. The guided wave propagation resulting in particle displacement and deformation was solved in the Solid Mechanics physics, while the piezoelectric effect and the actuation/sensing of the transducers were solved in the Electrostatics physics. The numerical model was simulated on an Intel® Xeon® 2.10 GHz virtual machine with 150 GB RAM and 300 GB disc space, which created some computational limits especially at high frequencies.

For utility poles in specific, the recommended embedment depth is 10% of the total pole's length plus 2 ft (61 cm). The total length of the pole modeled in COMSOL was 5.5 meters, in order to account for a suitable embedment length of 1.45 meters. This selected length was the expected value of an in-service embedded utility pole with an 8-

meter length. Due to computational limits the 8-meter pole cannot be modeled in COMSOL and was substituted by a 5.5-meter model. Regarding the soil – timber interface, a contact node was added to the common surface between both timber and soil where the contact pressure method used was Penalty. The actuators were placed at 2.3 meters, and the sensor at 1.5 meters from the bottom (right) edge of the pole as shown in Figure 4.1 (a) for the traction free model. Figure 4.1 (b) displays the model for the embedded boundary condition. As for applying mesh to the model, the wavelength found from the dispersion curves were used to calculate the mesh size, where an average of 6-10 elements per wavelength is required [42, 43]. For instance, the wavelength at 12.5 kHz is around 88 mm which results in a maximum element size of 14.6 mm when divided among 6 elements (minimum value). However, convergence tests were performed on the calculated mesh size and yielded 5.5 mm, with around 16 elements per wavelength.

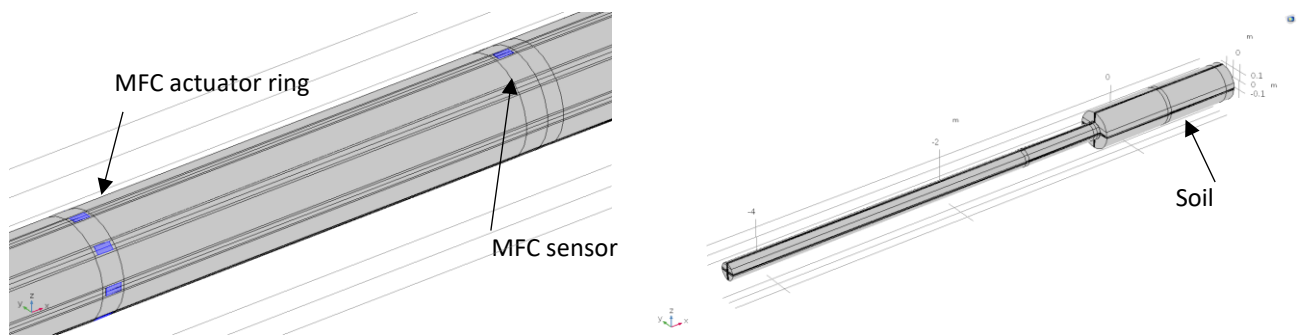


Figure 4.1 5.5-meter timber pole in COMSOL: (a) actuator ring and sensor placement and (d) embedded boundary condition.

Damage was introduced to the timber structure in the embedded section by removing a small section of the timber. This is to simulate the decay caused by external factors such as



termites or fungi. The numerical model for damaged timber was simulated for traction free and embedded models with the application of MFC ring. In addition, the effect of damage induction on determining the embedded length of the timber pole was examined. Figure 4.2 displays the damaged timber pole for traction free (a) and soil embedment (b) boundary conditions. Section of the soil was hidden to display the damage location in (b).

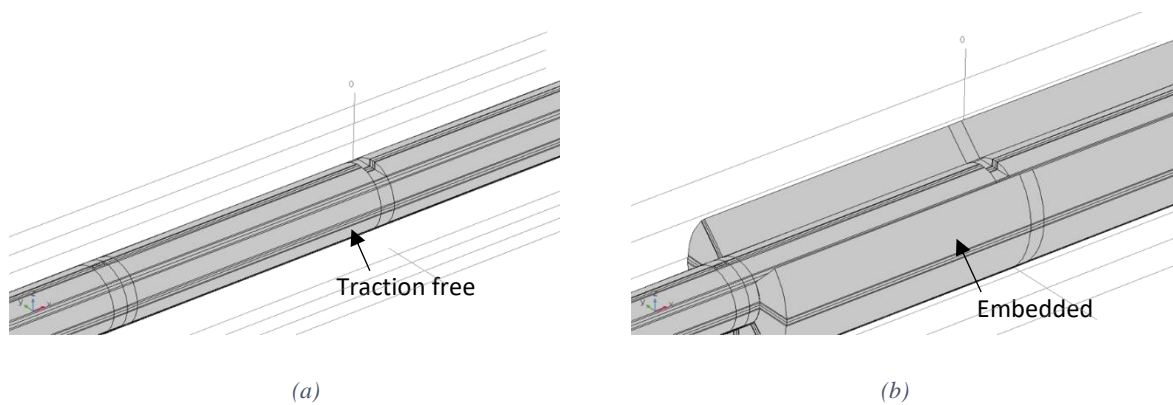


Figure 4.2 Damage induced in the timber structure for (a) traction free and (b) embedded boundary conditions.

In the traction free model, the location of damage was left empty where a section of the timber pole was removed. In the embedded model the location of the damage was filled with soil which was part of the embedded media. Figure 4.3 is a sketch of the top view of the timber pole, displaying the location of the damage, soil embedment and MFC locations. The sketch is a representation of the model used in COMSOL as well as the experimental setup discussed in the subsequent section. The damage was located 67.5 cm from the bottom edge of the pole and had a rectangular cross section of 4 cm width, 10 cm length and 10 cm depth inside the A clearance of 10 cm was added between the soil and the timber pole to create an adequate embedment condition.

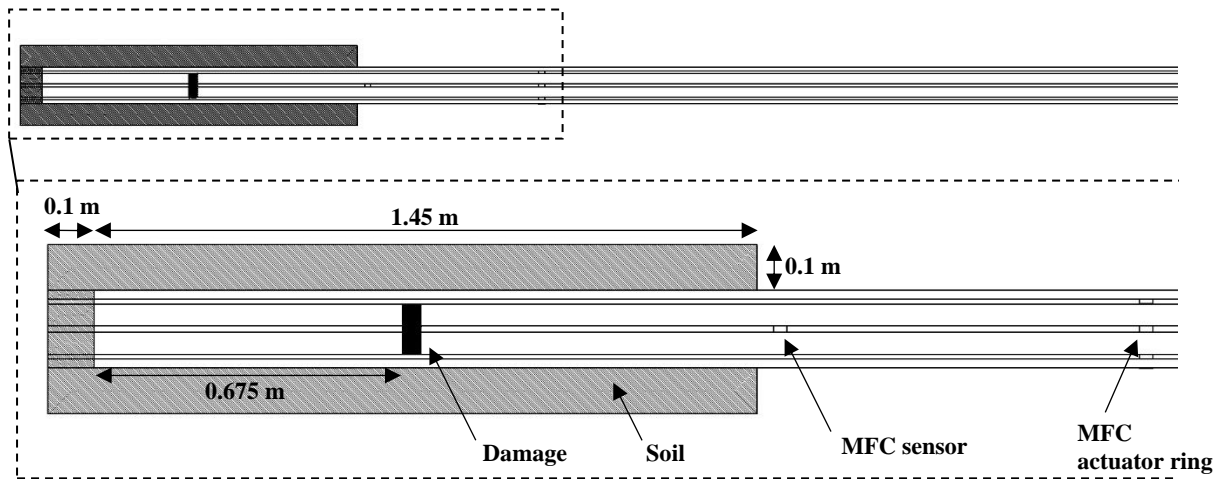


Figure 4.3 Top view sketch of the timber pole displaying embedment soil, damage location and MFCs.

#### 4.2.2. Experimental Setup

##### a) Validation

One of the most common types of timber in the electric distribution industry (utility poles) is scots pine (also known as *Pinus Sylvestris* [50] or white pine) which was used in the experimental setup. A validation process was undergone on an 8-meter timber pole where the effect of change in boundary conditions and damage induction was inspected. Multiple MFC actuation configurations (MFC ring) for tuning the propagating waves were tested to determine the embedded length and location of the damage. The embedded length corresponds of the distance between the MFC sensor and bottom edge of the pole, and the damage location corresponds of the distance between the sensor and the damage. MFCs of type M-2814 P1 were coupled to the pole's surface using Loctite's E120 HP epoxy adhesive at different locations along the specimen. The MFCs locations, as shown in Figure 4.3, were extremely critical due to the presence of knots and cracks that

can affect the propagating signal. In order to create an arrangement where the variable is the embedded condition, a wooden box was inserted at the back end of the pole where soil can be added and removed. Figure 4.4 (a) displays the 8-meter pole where the bottom section was inserted into the box. The pole was simply supported at the top end with metal supports and wood plies at the bottom end inside the box. The testing setup was only performed on the bottom end of the pole, which was the location of interest, to evaluate the embedded section and acquire less reflections from the top end of the pole. Last, the frequency of excitation was selected at 12.5 kHz and the actuator ring contained 8 MFCs, similar to the numerical model.

A damage was induced in the structure where the timber pole was cut in the section located inside the wooden box (embedded section). The experiments were performed for traction free and embedded conditions for sound (pre-damage) and damaged timber to investigate the effect on guided waves and embedment length estimation. The location of the damage was determined from the setups for both boundary conditions. Figure 4.4 (b) shows the damage created in the section of the pole, prior to soil embedment. To avoid variations during the experiment, all setups were performed simultaneously. To simulate the embedded condition, soil was added gradually to the wooden box and compressed at each layer to provide as much contact as possible with the surface of the timber pole.



Figure 4.4 (a) 8-meter timber utility pole and (b) MFC actuators and sensor configuration on the bottom end of the pole.

Figure 4.5 summarizes the step-by-step approach performed in the numerical and experimental analysis of the timber specimen under-study. The first steps that include the MFC ring design, GWs characterization and effect of boundary conditions were depicted previously in [55]. Evaluating the health state of the timber structure was then investigated, by determining the embedment length and damage location for the boundary conditions under testing.

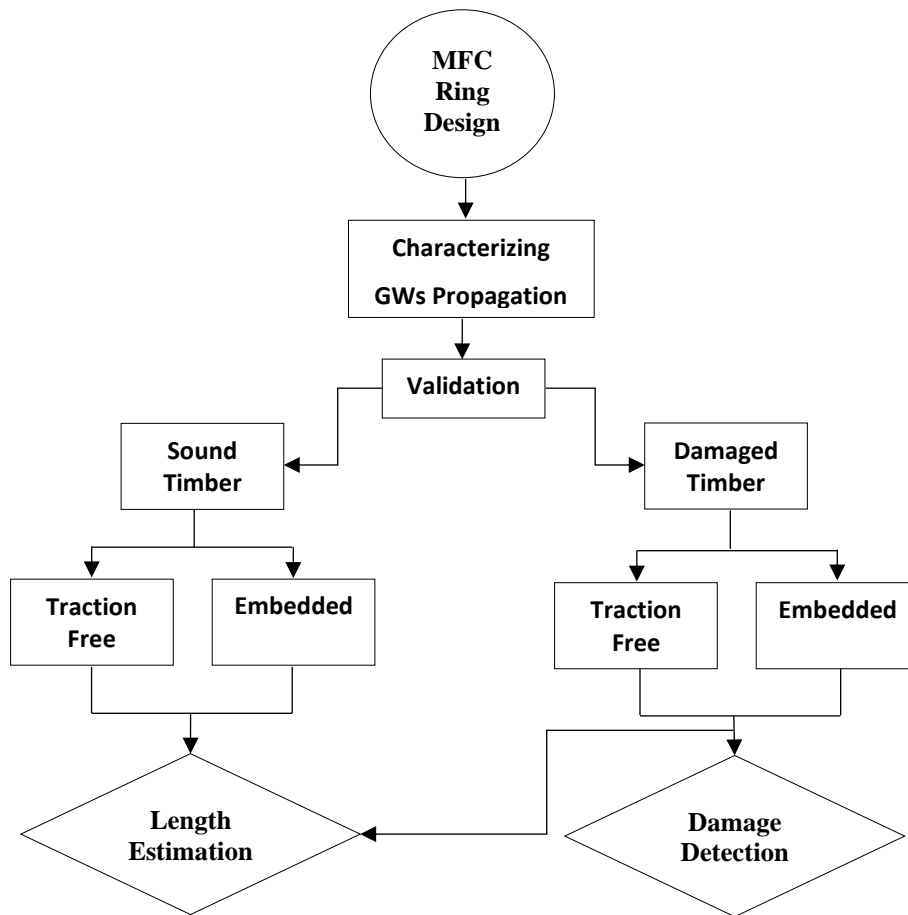


Figure 4.5 Flowchart of the approach undergone numerically and experimentally.

## b) Data Acquisition

The equipment used in the experimental setup were a Keysight 33500B signal generator, EPA-104 Piezo System Inc amplifier and Keysight InfiniiVision DSO-X-3024A oscilloscope. The 5-cycle Hanning window input signal to the actuator was generated with an initial peak to peak voltage of 10 V, then passed through the signal amplifier which increased the gain to reach almost 300 V peak to peak. Signals from the sensors were then acquired using the oscilloscope at a sampling rate of 2 MHz. The experimental setup for the validation performed on the 8-meter timber utility pole is shown in Figure 4.6.



*Figure 4.6 Experimental setup used on the 8-meter length timber utility pole.*

## **4.3. Results and Analysis**

### **4.3.1. Effect of Boundary Conditions**

The effect of boundary conditions on guided wave propagation behavior was depicted in Chapter 3:

## Understanding Guided Wave Propagation Behavior in Utility Timber Poles.

Multiple MFC configurations were actuated separately which correspond of single, 4-ring and 8-ring actuation at the selected frequency of excitation (12.5 kHz). Determining the embedded length with the variation of external boundary conditions is shown in section 4.3.3. Length Estimation and Damage Localization.

### **4.3.2. Effect of Damage Induction**

Behavior of guided waves in timber has been examined previously with the change in boundary conditions (traction free and embedded models) for sound wood. Results from inducing a damage in the timber structure (embedded section) are shown. The same boundary conditions and MFC actuation configurations were performed, at 12.5 kHz frequency. Also, to analyze the signals and determine reflections from the damage, it was crucial to apply the previously mentioned signal processing technique CEEMD.

Results from single MFC actuation for traction free and embedded conditions are displayed below for the numerical models. Figure 4.7 (a) shows the original acquired signal from single MFC actuation at 12.5 kHz in the traction free model for sound timber (solid line) and damaged timber (dashed line). From the original signals, some difference can be identified after time  $3E-3$  seconds. No solid identification of the damage reflection can be identified, which requires the usage of CEEMD to better identify the packets resulting from the damage. The first decomposed mode (IMF 1) is displayed in Figure 4.7 (b) where the reflected packets from the edge of the pole and damage are indicated. Flexural modes  $F(1,1)$  and  $F(1,2)$  reflect from the bottom edge of pole and arrive at  $1.8E-3$  and  $2.95E-3$



seconds propagating at 2540 m/s and 1429 m/s respectively. The second reflection of the bulk wave appears at  $2.2E-3$  seconds where the packet is completely non-dispersive. Reflections of longitudinal modes  $L(0,1)$  and  $L(0,2)$  arrive at  $4E-3$  and  $4.5E-3$  seconds. As for the damage reflections, the decomposed signal shows the arrival of  $F(1,2)$  from the damage at  $1.8E-3$  seconds, which coincides with the arrival of  $F(1,1)$  edge reflection. Longitudinal mode  $L(0,1)$  reflects from the damage and arrives solely at  $2.6E-3$  seconds. The packet at  $3.4E-3$  seconds appears to have a higher amplitude in the damaged signal (dashed line) due to the arrival of  $L(0,2)$  damage reflection, which coincides with the second reflection of  $F(1,1)$  from the top edge of the pole. Last, longitudinal mode  $L(0,3)$  propagating at around 508 m/s reflects from the damage and arrives solely at  $4.35E-3$  seconds. Longitudinal modes provide more accurate information about the damage, especially due to the non-concatenated packets such as  $L(0,1)$  and  $L(0,3)$  reflections from the damage. Due to their higher speed, flexural modes reflections seem to arrive early in the signal which results in the concatenation with other modes of lower speeds. Therefore, longitudinal modes can be solely used for the damage localization process. Figure 4.8 (a) shows the numerical original acquired signal from single MFC actuation at 12.5 kHz in the embedded model for sound timber (solid line) and damaged timber (dashed line). The propagating modes are identified similarly according to their group velocity where minor differences can be identified between the sound and damaged timber. The results are similar to the traction free model, especially with respect to the arrival times of the modes from the pole's edge and damage. It can be noted that some of the reflections in the embedded boundary condition have higher amplitudes than the traction free one. For instance,  $F(1,2)$ 's second reflection has an amplitude of 43 mV, compared to 29 mV in the

traction free model. Furthermore, a new packet appears in the embedded model at  $3.75E-3$  seconds, indicating the arrival of mode  $F(4,1)$  from the damage. This mode propagates at  $625$  m/s and its reflection from the damage does not appear in the traction free model. Longitudinal mode  $L(0,3)$  reflects from the damage and arrives solely at  $4.35E-3$  seconds propagating at  $508$  m/s. The reflection amplitude is  $24$  mV, compared to  $15$  mV in the traction free model which means that the amplitude was maintained further in the embedded condition.

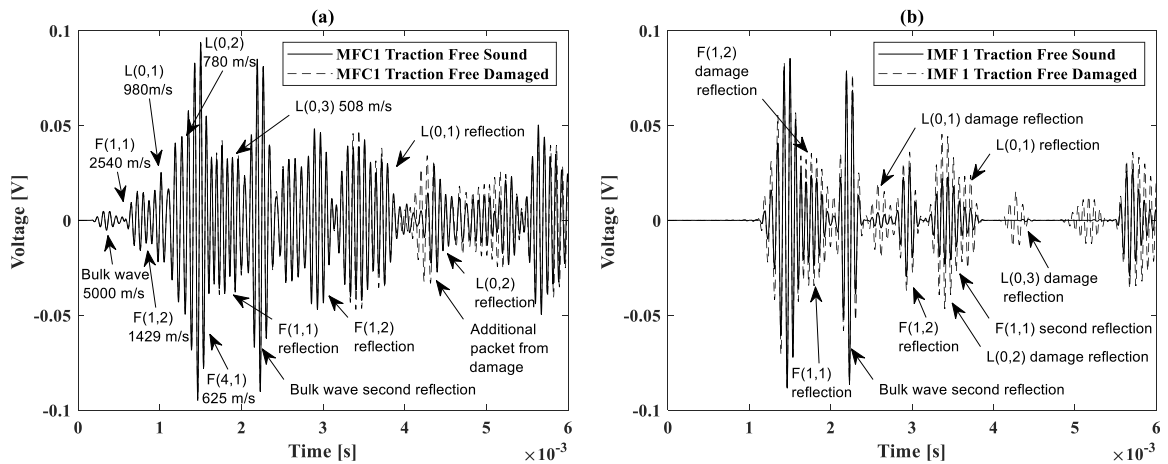


Figure 4.7 Numerical results: Traction free sound (solid line) and damaged (dashed line) using single MFC actuation at  $12.5$  kHz (a) original signal and (b) decomposed signal after CEEMD (IMF 1).

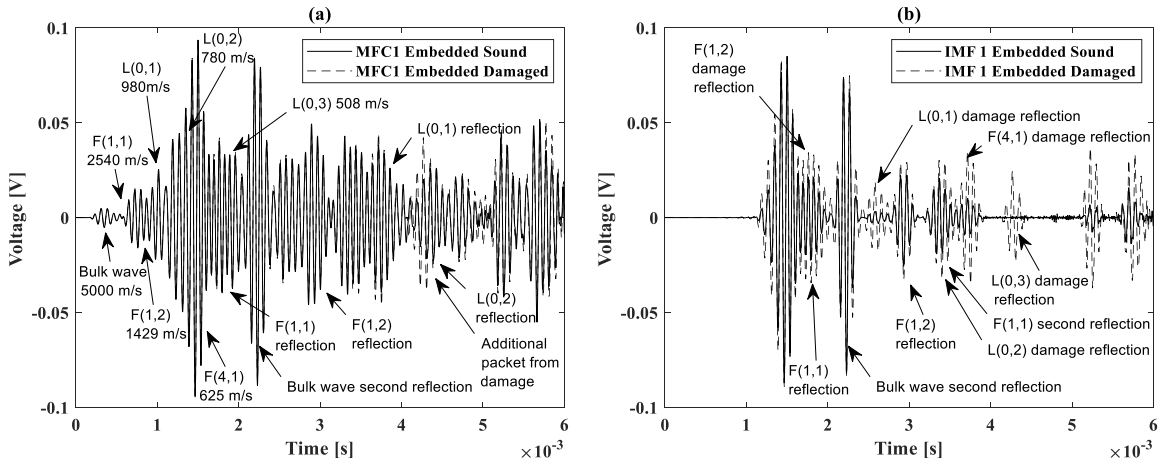


Figure 4.8 Numerical results: Embedded sound (solid line) and damaged (dashed line) using single MFC actuation at 12.5 kHz (a) original signal and (b) decomposed signal after CEEMD (IMF 1).

In the experimental validation, the induced damage in the timber structure resulted in much more complicated results than the numerical. In the experimental timber specimen, several knots and cracks in the structure cause reflections which complicates the acquired signals. Therefore, the propagating wave modes arrivals could be overlapping in most cases which makes it hard to determine the damage location for more than one mode. Figure 4.9 displays the acquired signal from the traction free model for single MFC actuation at 12.5 kHz excitation frequency. The modes are identified in a similar manner and are displayed on the figures with their reflections. Flexural modes F(1,1) and F(1,2) arrive at the beginning of the signal and reflect from the bottom edge of the pole at 2E-3 and 3E-3 seconds. Also, longitudinal modes L(0,1) and L(0,2) propagate at 1140 m/s and 845 m/s. The reflection of mode L(0,1) from the bottom edge is clear in the sound signal, but does not appear in the damaged signal at 4E-3 seconds, which is due to the presence of damage between the edge and the direction of propagation of the waves. No other major difference

can be identified between the original sound and damaged signals, therefore CEEMD was applied to be able perform the comparison. Figure 4.10 shows the second IMF of the decomposed signal where the reflections can be identified more accurately. F(1,1) knot reflection arrives around  $3E-3$  seconds resulting from knot present 1 meter from the actuator. An additional packet concatenates the arrival of F(1,2) edge reflection, which indicates the reflection of mode L(0,1) from the damage. The packet has a higher amplitude in the damaged signal, which means that there are two concatenated reflections compared to only one reflection in the sound signal. In addition, the reflection of L(0,1) at  $4E-3$  seconds is only present in the sound signal. This reflection seems to be missing in the damaged signal where the wave does not reach the sensor due to the presence of damage between the sensor and the pole's bottom edge.

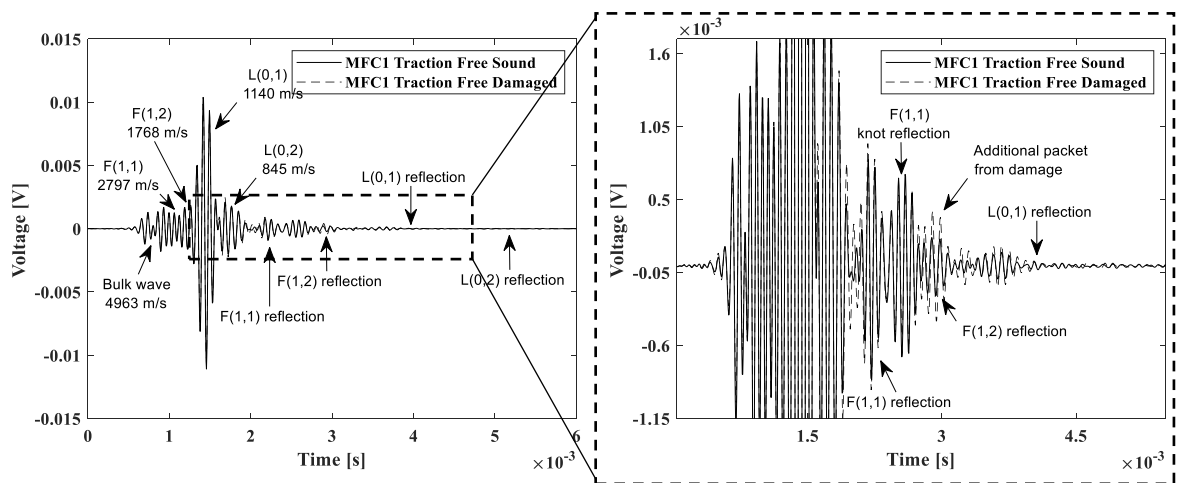


Figure 4.9 Experimental results: Traction free sound (solid line) and damaged (dashed line) using single MFC actuation at 12.5 kHz.

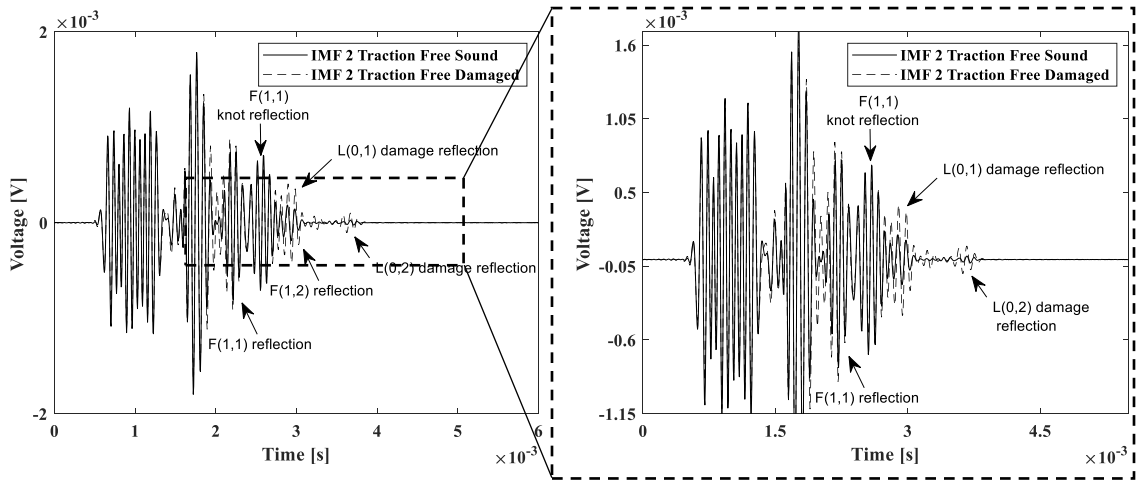


Figure 4.10 Experimental results: Decomposed signal after CEEMD (IMF 2) for traction free sound/damaged using single MFC actuation at 12.5 kHz.

In the embedded boundary condition, the reflecting wave packets from the damage were highly distorted compared to the traction free condition. This might be due to the timber – soil contact at the damage location which absorbed the propagating waves. Figure 4.11 shows the acquired signal from the embedded condition for single MFC actuation at 12.5 kHz. The propagating modes are identified similarly, with minor variations in the speed and edge reflections. Unlike the traction free model, mode L(0,1) reflection from the bottom edge of the pole was captured in the damaged signal. Longitudinal modes L(0,1) and L(0,2) reflect from the damage and arrive at around  $3 \times 10^{-3}$  and  $3.65 \times 10^{-3}$  second. The arrival of L(0,1) damage reflection coincides with the reflection of F(1,2) from the pole's edge, where the amplitude of the packet in the damaged signal is slightly higher. The amplitude of reflecting packet from the damage is higher for mode L(0,1) in the traction free condition, compared to the embedded one which might be due to the timber – soil interface at the damage location. The damage can still be localized accurately using mode

L(0,1) in both boundary conditions. Also, the arrival of L(0,2)'s damage reflection can be indicated which coincides with the arrival of knot reflection of L(0,1) present at 1.2 meters from the actuator.

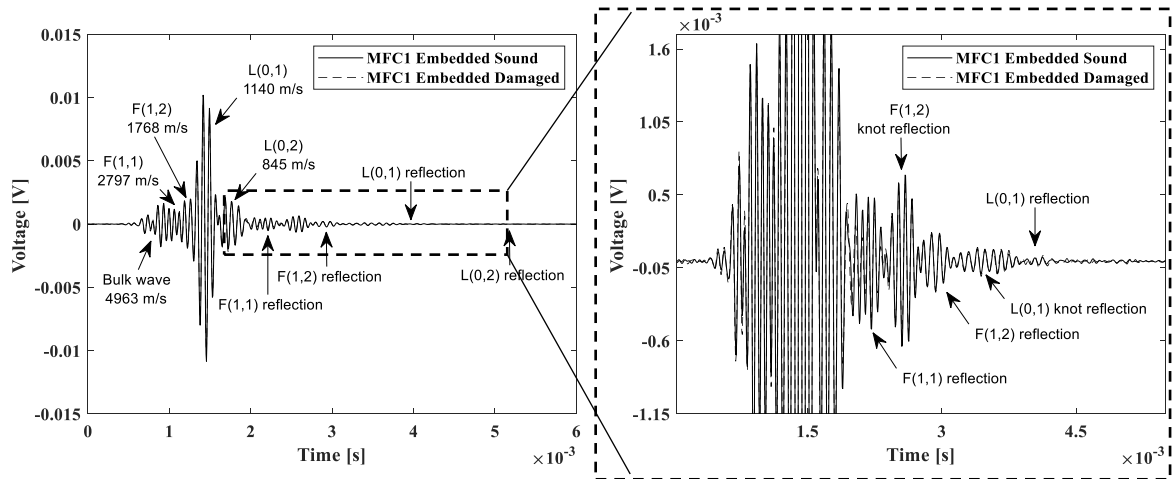


Figure 4.11 Experimental results: Embedded sound (solid line) and damaged (dashed line) using single MFC actuation at 12.5 kHz.

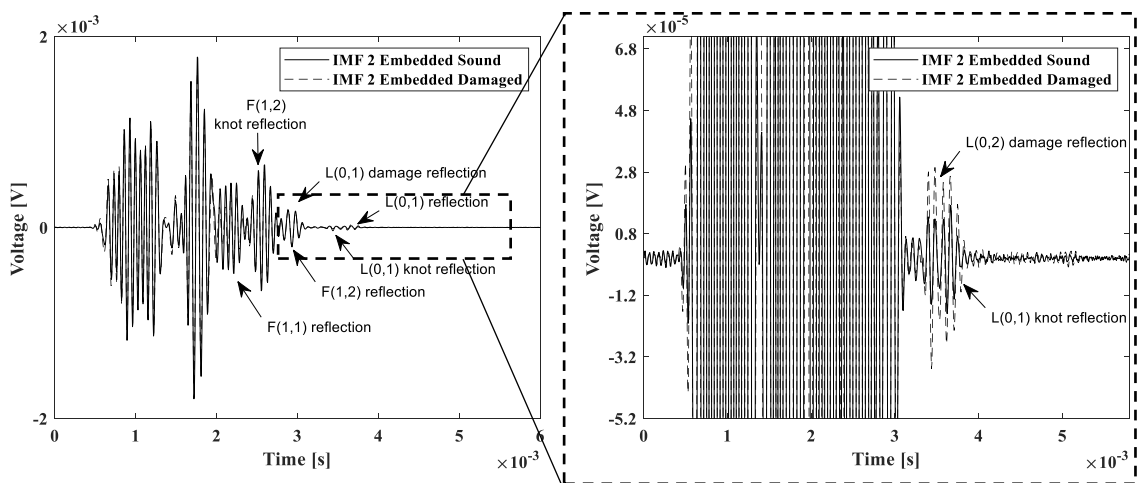


Figure 4.12 Experimental results: Decomposed signal after CEEMD (IMF 2) for embedded sound/damaged using single MFC actuation at 12.5 kHz.

The single MFC actuation could provide enough information regarding the presence of decay or damage inside the timber specimen. The reflected packets from the damage were identified successfully in both traction free and embedded boundary conditions. However, multiple MFC actuation might not be suitable for damage identification, especially if the damage is located axially along a certain face of the timber pole. For instance, the induced damage in the tested pole lied axially on the same straight line as the MFCs in the single actuation configuration. Therefore, actuating the 4 or 8-ring could prevent the damage reflection to be properly acquired from the sensor. This was depicted numerically and experimentally where the MFC ring was actuated in the damaged condition and compared to the results of the sound specimen.

The results of the damaged timber pole show that the ring actuation could have negative effects on damage localization. For instance, Figure 4.13 and Figure 4.14 show the original and decomposed (IMF1) numerical signals in the embedded model using 4 ring actuation. The acquired results show that there is negligible difference between the sound and damaged timber specimen. Reflection of longitudinal modes  $L(0,1)$  and  $L(0,2)$  from the damage are not captured as the single actuation shown earlier, where the expected time of arrival does not show any packet. This is depicted in the decomposed signals after CEEMD (IMF 1) shown in Figure 4.13 (b) and Figure 4.14 (b). In the traction free model, actuating 4 and 8 MFCs lead to similar results as the embedded boundary conditions. No reflections from the damage were acquired where they do not appear in the signal, even after applying CEEMD. However, the reflections of  $L(0,1)$  and  $L(0,2)$  from the bottom edge of the pole were successfully captured and are identified on the figures in both MFC ring actuations.

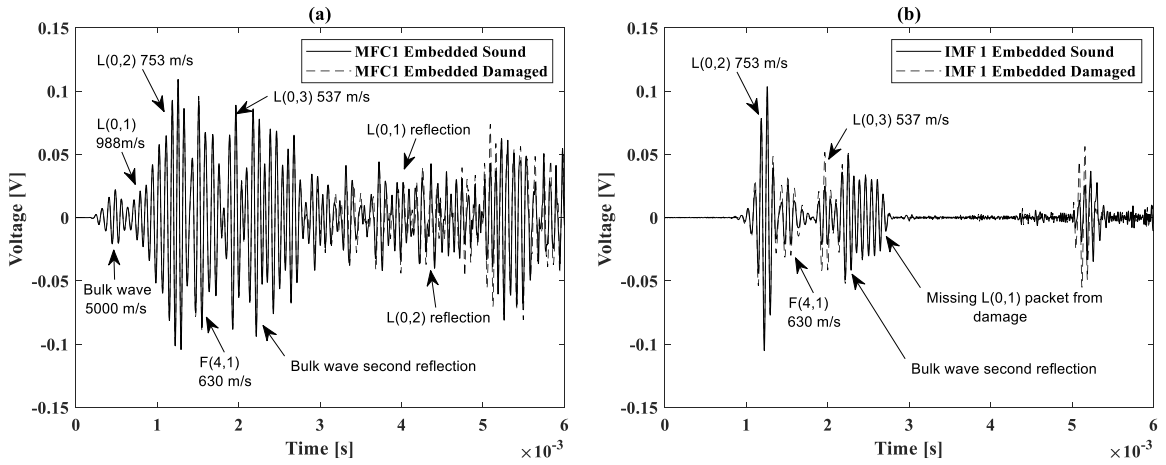


Figure 4.13 Numerical results: Embedded sound (solid line) and damaged (dashed line) using 4 ring MFC actuation at 12.5 kHz (a) original signal and (b) decomposed signal after CEEMD (IMF 1).

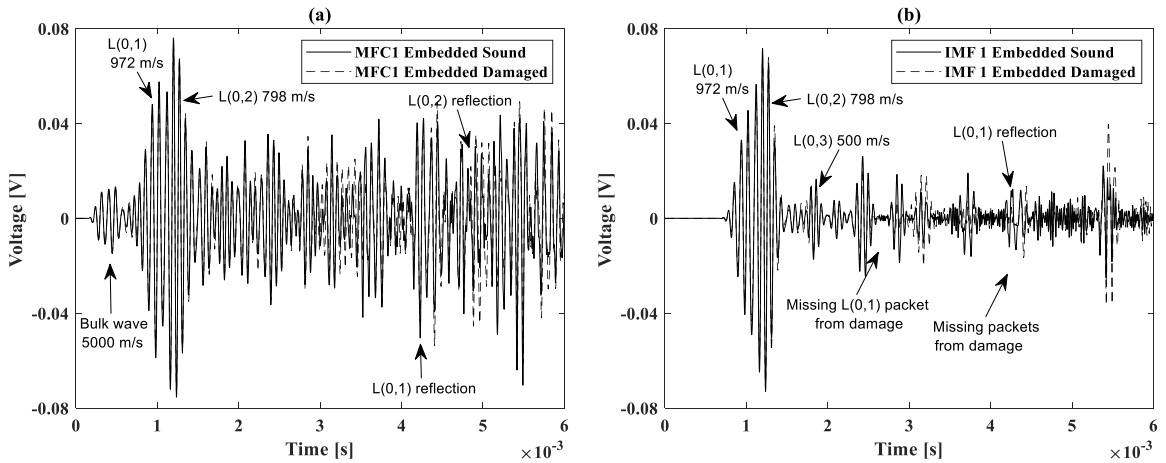


Figure 4.14 Numerical results: Embedded sound (solid line) and damaged (dashed line) using 8 ring MFC actuation at 12.5 kHz (a) original signal and (b) decomposed signal after CEEMD (IMF 1).

In the experimental results, the MFC ring actuation also causes the reflections from the damage to be less exposed. In 4 ring actuation shown in Figure 4.15, no acquired packets from the damage appear before time 3E-3 seconds in the embedded boundary condition. No major difference can be determined between the sound and damaged timber



specimen, even after performing CEEMD. The same appeared in the 8 ring actuation shown in Figure 4.16 where no reflections from the damage were captured. The packet of L(0,1) from the damage appears to be missing around time 3E-3 seconds as indicated in the figure. Results acquired from the traction free setups also returned similar results, where the damage did not have any significant effect on the transmitted signals. It can be noticed that reflection of L(0,1) is clearly identified using the 4 and 8 MFC ring actuation, where the embedded length can be estimated even with the presence of the damage.

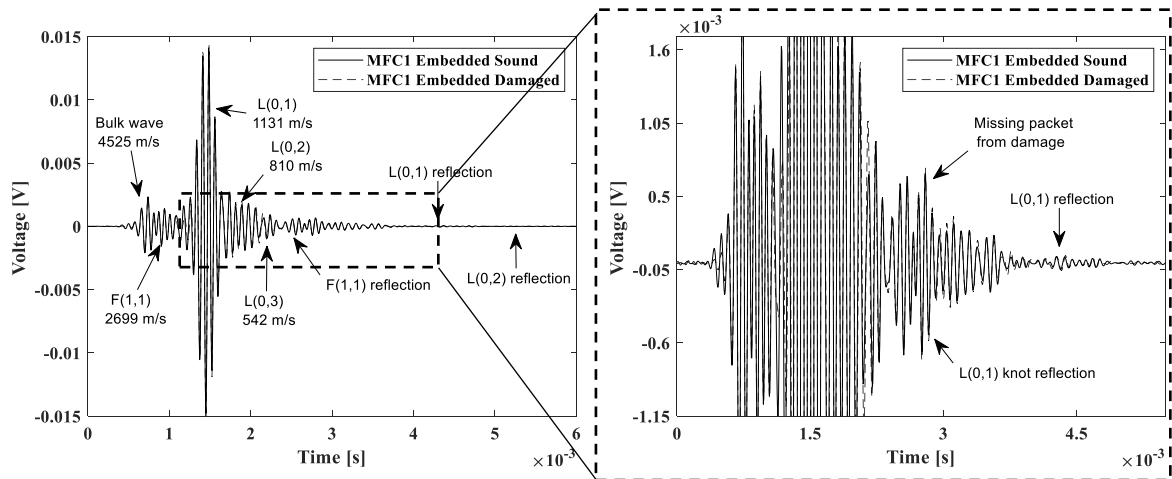


Figure 4.15 Experimental results: Decomposed signal after CEEMD (IMF 2) for embedded sound/damaged using 4 ring MFC actuation at 12.5 kHz.

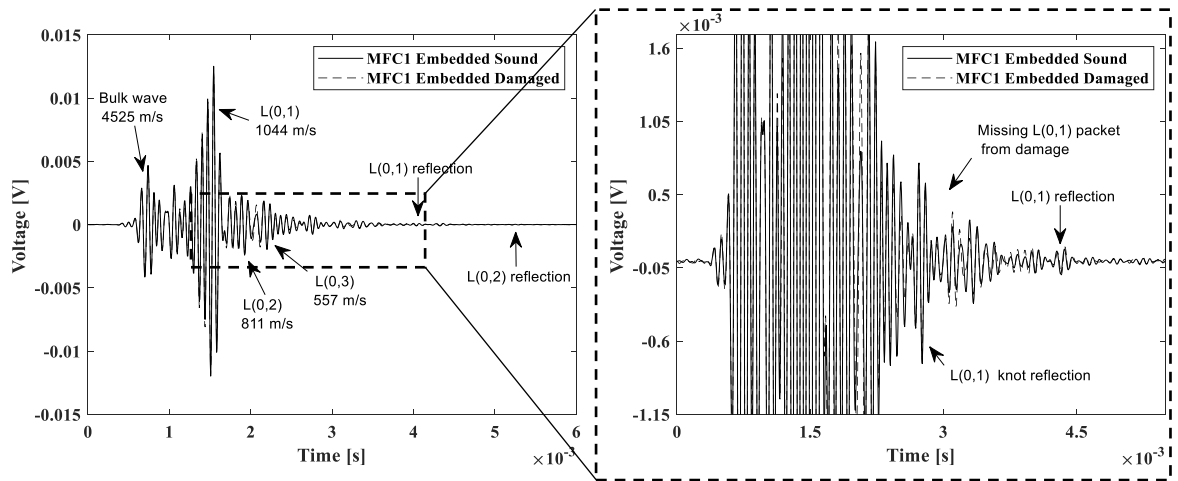


Figure 4.16 Experimental results: Decomposed signal after CEEMD (IMF 2) for embedded sound/damaged using 8 ring MFC actuation at 12.5 kHz.

### 4.3.3. Length Estimation and Damage Localization

The estimation of embedment length and damage location can be performed using the resulting reflected packets of a selected wave mode. From the propagation velocity and arrival time of the reflections, the total propagation distance can be calculated. Figure 4.17 shows a top view sketch of the pole used in the numerical and experimental validation. The reflecting packets from the bottom edge of the pole can provide an estimation of the distance between the edge and the MFC sensor. As for locating the damage, the reflections resulted can be used to estimate the distance between the damage and the MFC sensor. The actual distance between the MFC sensor and bottom edge of the pole is 1.5 meters, and between the sensor and center of the damage is 79 cm. These values are a reference used for calculating the distance estimation error.

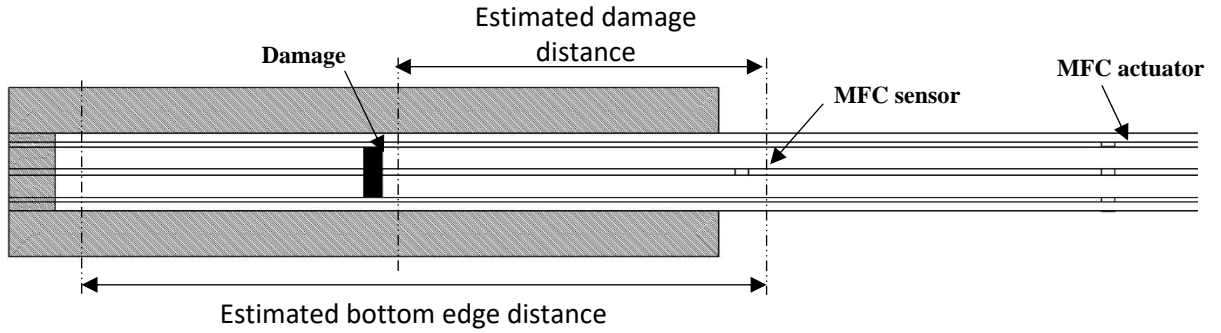


Figure 4.17 Top view sketch of the pole specimen displaying the embedded and damage distances to be estimated.

The below formula is used to estimate the distance between the MFC sensor and the bottom edge, and the center of the damage.  $V$  is the propagation velocity of the wave mode selected.  $\Delta t$  is the time difference between the first arrival of the selected mode, and the second arrival resulting from the reflection. This reflection could be either from the damage or the bottom edge of the pole. The total distance indicates the propagation distance covered by the wave and must be divided by 2.

$$d = \frac{V \times \Delta t}{2} \quad (m)$$

Several wave modes can be selected to estimate the distances required, which were shown in the results section at 12.5 kHz frequency. However, not all modes can be used due to their complexity and dispersive nature. Longitudinal wave modes can be found in almost all cases, whether in sound/damaged timber or in multiple MFC (ring) actuation where they acquire an enhanced amplitude. Therefore, they can be used for the distance estimation. The distance between the MFC sensor and bottom edge of the pole, which corresponds to the embedment length of the pole, was determined using data from longitudinal mode L(0,1). This mode was selected due to its consistency in all experiments

and least dispersive nature, in addition to the higher amplitude it acquires than any other mode.

Table 4.1 displays the bottom edge distance estimation using the numerical results for single, 4-ring and 8-ring MFC actuation at 12.5 kHz excitation frequency. The propagation velocity of L(0,1) is calculated from the first arrival of the mode and the distance between the MFC actuator and sensor. It can be noted how the multiple MFC actuation (4 and 8 ring) enhances the reflection amplitude in mV, where it is significantly higher than the single actuation. The embedded condition has no significant effects on the reflections other than the amplitude. The presence of damage in all actuation configurations causes the reflection amplitude from the bottom edge to be lower than the sound timber pole.

<i>Actuation</i>	<b>Boundary condition</b>	<b>1<sup>st</sup> arrival time (s)</b>	<b>2<sup>nd</sup> arrival time (s)</b>	<b>Reflection amplitude (mV)</b>	<b>Velocity (m/s)</b>	<b>Estimated distance (m)</b>	<b>Error (%)</b>
<i>Single</i>	<b>Traction Free Sound</b>	0.001018	0.004023	8.7	979	1.471	1.94
	<b>Embedded Sound</b>	0.001018	0.00402	17.5	979	1.469	2
	<b>Traction Free Damaged</b>	0.001018	0.004002	5.5	979	1.461	2.62
	<b>Embedded Damaged</b>	0.001018	0.004023	7.4	979	1.471	1.94
<i>4-Ring</i>	<b>Traction Free Sound</b>	0.00101	0.004023	39.9	988	1.475	1.68
	<b>Embedded Sound</b>	0.00101	0.00402	33.3	988	1.473	1.77
	<b>Traction Free Damaged</b>	0.00101	0.004028	32.2	988	1.477	1.51

	<b>Embedded Damaged</b>	0.00101	0.004028	26.1	988	1.477	1.51
<b>8-Ring</b>	<b>Traction Free Sound</b>	0.001023	0.004198	45.3	972	1.543	2.79
	<b>Embedded Sound</b>	0.001023	0.004193	40.2	972	1.541	2.64
	<b>Traction Free Damaged</b>	0.001023	0.004198	35.6	972	1.543	2.79
	<b>Embedded Damaged</b>	0.001023	0.004195	37.3	972	1.542	2.7

Table 4.1 Numerical results: Bottom edge distance estimation using mode  $L(0,1)$  for single, 4-ring and 8-ring MFC actuation.

Table 4.2 displays the bottom edge distance estimation using the experimental results for single, 4-ring and 8-ring MFC actuation. The application of MFC ring actuation causes the reflection amplitude of  $L(0,1)$  to increase compared to the single MFC actuation. Also, in the traction free damaged timber pole, the single actuation was not enough for the edge reflection to appear which resulted in a missing packet around  $4E-3$  seconds. In the embedded damaged pole, single actuation, the reflection from the bottom edge of the pole was captured but at a lower amplitude than the sound timber specimen. The missing packet in the damaged condition does not appear in the 4 and 8-ring MFC actuation, where the distance is estimated normally.

<i>Actuation</i>	<b>Boundary condition</b>	<b>1<sup>st</sup> arrival time (s)</b>	<b>2<sup>nd</sup> arrival time (s)</b>	<b>Reflection amplitude (mV)</b>	<b>Velocity (m/s)</b>	<b>Estimated distance (m)</b>	<b>Error (%)</b>
<i>Single</i>	<b>Traction Free Sound</b>	0.001446	0.004046	0.0422	1140	1.482	1.2
	<b>Embedded Sound</b>	0.001446	0.004113	0.0402	1140	1.52	1.33
	<b>Traction Free Damaged</b>	0.001446	N/A	N/A	1140	N/A	N/A
	<b>Embedded Damaged</b>	0.001446	0.004098	0.0265	1140	1.512	0.77
<i>4-Ring</i>	<b>Traction Free Sound</b>	0.001451	0.004092	0.034	1131	1.4935	0.434
	<b>Embedded Sound</b>	0.001451	0.004113	0.0352	1131	1.5054	0.36
	<b>Traction Free Damaged</b>	0.001451	0.004035	0.0536	1131	1.461	2.58
	<b>Embedded Damaged</b>	0.001451	0.004124	0.0381	1131	1.512	0.766
<i>8-Ring</i>	<b>Traction Free Sound</b>	0.00151	0.004326	0.1253	1044	1.47	2
	<b>Embedded Sound</b>	0.00151	0.004332	0.121	1044	1.473	1.79
	<b>Traction Free Damaged</b>	0.00151	0.004316	0.064	1044	1.465	2.35
	<b>Embedded Damaged</b>	0.00151	0.004352	0.11	1044	1.4835	1.1

Table 4.2 Experimental results: Bottom edge distance estimation using mode  $L(0,1)$  for single, 4-ring and 8-ring MFC actuation.

Determining the location of the damage was performed using longitudinal mode  $L(0,1)$  for the single MFC actuation. Table 4.3 shows the damage location estimation using the numerical results acquired.

<i>Actuation</i>	<b>Boundary condition</b>	<b>1<sup>st</sup> arrival time (s)</b>	<b>2<sup>nd</sup> arrival time (s)</b>	<b>Reflection amplitude (mV)</b>	<b>Velocity (m/s)</b>	<b>Estimated distance (m)</b>	<b>Error (%)</b>
<i>Single</i>	<b>Traction Free Damaged</b>	0.001018	0.00266	3.107	979	0.804	1.71
	<b>Embedded Damaged</b>	0.001018	0.002673	2.83	979	0.81	2.48

Table 4.3 Numerical results: Damage localization using mode L(0,1) for the single MFC actuation.

Estimating the damage location using the experimental results is shown in Table 4.4 for the single MFC actuation. In the 4-ring actuation – traction free condition, the reflecting packet from the damage was identified but with a higher error of 7.8 %. It does not appear in the 4-ring – embedded boundary condition, nor in any of the 8-ring MFC actuations.

<i>Actuation</i>	<b>Boundary condition</b>	<b>1<sup>st</sup> arrival time (s)</b>	<b>2<sup>nd</sup> arrival time (s)</b>	<b>Reflection amplitude (mV)</b>	<b>Velocity (m/s)</b>	<b>Estimated distance (m)</b>	<b>Error (%)</b>
<i>Single</i>	<b>Traction Free Damaged</b>	0.001446	0.002928	0.42	1140	0.845	6.48
	<b>Embedded Damaged</b>	0.001446	0.002928	0.22	1140	0.8245	6.48

Table 4.4 Experimental results: Damage localization using mode L(0,1) for the single MFC actuation.

It was mentioned in the Effect of Damage Induction section that reflections from other modes were captured and might predict accurately the location of the damage. For instance, in some cases longitudinal mode L(0,2) appears to reflect from the damage. In the experimental single MFC actuation – embedded condition, reflection of L(0,2) from the damage arrives at 3.7E-3 seconds providing a damage location estimation with 0.886 %

error. This mode does not appear in the 4 and 8-ring MFC actuation experimental results. However, in the numerical results the damage reflections of mode L(0,2) were acquired in the 8-ring MFC actuation. The damage location was estimated in the traction free and embedded boundary conditions with a 2.75 % error. In addition, damage reflections of flexural modes F(1,1) and F(1,2) were also captured in the single MFC actuation from the numerical results in both boundary conditions simulated. Location of the damage estimated using F(1,1) and F(1,1) resulted in an error of 8.8 % and 5 % respectively. This indicates how the flexural modes are much more complicated than flexural modes with a highly dispersive nature, which results in inaccuracy when estimating the location of the damage.

#### **4.4. Discussion**

For the evaluation of timber poles using guided stress waves, it is important to understand the propagation behavior and characteristics of the waves under certain features. These features include the change in boundary conditions from traction free to embedded, and the presence of decay/damage in the embedded section of the pole. Two separate structural health states were tested, where the effect of soil embedment was analyzed for sound and damaged timber. The condition assessment was performed on all cases, by estimating the embedded depth of the pole and damage location. Based on the investigation performed in the previous work [55], the application of an MFC ring (4 and 8 MFC actuation), further reduced the effects of the boundary conditions tested where the reflections' velocities were less effected, especially for longitudinal mode L(0,1).



For determining the embedded length, the acquired numerical and experimental results revealed that longitudinal mode  $L(0,1)$  was the most suitable where it had the least amount of dispersion and highest amplitude compared to other propagating modes. This mode had clear reflections from the bottom edge of the pole, even with the variation of boundary conditions and damage induction inside the timber. The embedded condition lead to a more accurate embedded length estimation than the traction free one. The most accurate length estimation was achieved in the 4 ring MFC actuation, damaged pole (traction free and embedded) numerical model with a 1.51 % error. Experimentally, the 4 ring MFC actuation also had the lowest estimation error in the embedded sound pole with only 0.36 %.

The presence of a defect or damage in the timber structure can be identified using guided waves by the reflected wave modes. The behavior of these reflections depends on the wave mode present and its displacement profile. Therefore, discrepancies might occur within the acquired signals especially with the variation of several features during the testing process. These features include the multiple MFC actuation configuration and the change in boundary conditions. For instance, the results displayed in the Effect of Damage Induction section for multiple MFC actuation (4 and 8 ring) confirmed that the reflections from the damage can be extremely difficult to identify. This can be caused by several factors, one of which is the damage location. The induced damage was located at the top face of the timber pole, in the same plane as the MFC sensor and actuator in the single actuation configuration. As a result, the MFC ring actuation leads to a suppression effect of the reflected waves occurring at the top plane where the damage is located. Since there is no change in geometry on the rest of the planes of the pole where the actuation is occurring,

the waves propagate normally along the pole and dominate the reflections that arise from the damage. However, if a more significant change exists in the geometry that covers a larger section of the pole (a deeper or larger damage along the circumference), the MFC ring actuation might capture the reflecting waves more precisely since they become more dominant. This was proven in the numerical and experimental results for the single MFC actuation, where the reflections from the damage were acquired in both traction free and embedded boundary conditions especially for longitudinal mode  $L(0,1)$ . Since the single actuation was performed on the same plane as the damage, the MFC sensor was able to catch the reflections of  $L(0,1)$  where there was no other point of actuation on the pole's circumference. Results from the single actuation yielded a 2.5 % and 6.5 % accuracy when locating the damage location in the numerical and experimental testing. The soil – timber interface could have affected the behavior of guided waves, where the displacement profiles of the propagating modes could be more sensitive in the embedded condition than the traction free. Therefore, for damage localization and detection it is proposed to actuate each plane solely at a time, while acquiring the signals on the same plane as actuation. This procedure is similar to creating a tomographic image of the timber pole, where each plane can be analyzed separately and compared to provide a better understanding of the conditions of the pole at each plane of actuation. This requires the installment of a sensor ring with the same number of MFCs as the actuator ring. As for the effect of damage on embedded length estimation, it was found that reflections from the bottom edge of the pole were not affected especially in the MFC ring actuation, where the distance was adequately estimated.

## Chapter 5 Future Work

Guided waves deliver crucial information about the structural integrity of timber structures. The health state can be evaluated qualitatively and quantitatively, where the embedded length and the presence of damage in the structure can be accurately identified. In order to provide a better evaluation of timber poles, deep learning algorithms for automated guided wave interpretation can be performed. The evaluation techniques used in this work lead to a well-defined system for damage detection with less than 7 % error. However, no further information was collected concerning the damage state of the timber pole. Therefore, the application of learning algorithms could potentially improve the damage detection process providing more information regarding the location and dimensions of the defect present. The assessment of timber poles using the techniques provided in this work can be improved significantly. More damage cases can be experimented, whether by inducing additional damages at different locations in the timber specimen or by increasing the size of the already-induced damage. This step would be beneficial to validate the single MFC actuation for damage localization in addition to the effect of MFC ring. For a robust damage localization process, it is required to have an MFC sensor ring facing the MFC actuator ring. Therefore, the application of additional MFC sensors around the pole's circumference could also be beneficial for evaluating damaged timber where a tomographic diagram can be created.

Development of the hardware used in this work could lead to further improvement of the acquired results, especially when dealing with high wave attenuation, distortion and other external factors that could affect the performance of MFC transducers. For instance,

the MFCs were actuated with 300 Volts peak to peak in the experimental setup, which was the maximum capability of the amplifier used in this work. Therefore, a higher-gain amplifier can be used to increase the input voltage to the MFC, which can handle up to 2000 Volts peak to peak [49], almost six times higher than the voltage used. This enhancement can in return cause higher acquired voltage from the MFC sensors, and an enhanced amplitude of the generated waves and their reflections. The MFCs also require further refinement, especially that there was no external protection and enclosure which could greatly affect their performance. Consequently, the design of an MFC enclosure or a complete MFC ring add-on for the actuators and sensors, is crucial for the lifecycle and performance of the MFCs used for generating/sensing guided waves.

## Chapter 6 Conclusions

Propagation behavior of guided waves (GWs) in timber was scrutinized by the means of Macro Fiber Composites (MFCs) experimentally and numerically using COMSOL Multiphysics. When performing NDT on timber utility poles using GWs, the complex structure of timber causes a relatively complicated wave propagation behavior, which requires methods to control the propagating waves. In this work, the MFCs proved to be a convenient tool for generating/sensing GWs in timber structures, especially due to their reliability and flexibility to be coupled on curved – rough surfaces. Several methods for wave mode tuning and enhancement were investigated, while varying the external boundary conditions and health state of the timber under study.

In order to understand the behavior of GWs, the excitation frequency was varied where the propagating wave modes were identified, by their group velocities, from the dispersion curves generated for transversely isotropic timber. The actuation of an MFC ring coupled around the pole's circumference was tested numerically and proved to cancel out unwanted flexural wave modes. The ring also enhanced the propagation of longitudinal modes and their reflections, causing a higher acquired voltage from the MFC sensor. A validation process was performed on an actual 8-meter length timber utility pole, where the MFC ring was applied. The propagation behavior of GWs was then analyzed considering traction free and embedded boundary conditions. It was found that the soil does not have significant effects on GWs, where the amplitude and propagation velocities of certain wave modes were slightly affected. The difference between traction free and embedded boundary

conditions can be considered negligible when performing the evaluation process for embedded depth determination and decay/damage localization.

The assessment of the two most important features when performing non-destructive testing on timber utility poles was conducted in this work. Embedded length of the pole and the presence of damage/decay in the embedded section were determined numerically and experimentally using GWs. Evaluating the structure's health state was performed with the variation of external boundary conditions, such as soil embedment, and the application of an MFC ring coupled around the pole's circumference. The ring enhanced the propagation of mode  $L(0,1)$  and was recommended for estimating the embedded depth of the pole, yielding an accuracy of 97 % in both numerical and experimental results, even with the presence of damage in the structure. Determining the location of the damage in the embedded section was performed using the single MFC actuation and data from mode  $L(0,1)$ , with an error less than 7 %. Actuating 4 and 8 MFCs in the ring did not provide enough information about the location of the damage, where the reflections were more difficult to identify. Therefore, it was proposed to use the single MFC actuation configuration for allocating the decays present within the plane of actuation. As for the embedded length, it can be successfully determined by the MFC ring actuation configuration.

Various improvements can be achieved with further future effort, especially with respect to applying learning algorithms for damage detection and localization. Additional damage cases can be simulated to validate the effect of single MFC excitation numerically and experimentally on the timber utility pole. Further work on the MFC ring design and

enclosure can enhance the generated guided waves, which could eventually lead to a more accurate and suitable system for the assessment of timber structures.

## BIBLIOGRAPHY

- [1] E. P. DeGarmo, J. T. Black, R. A. Kohser, and B. E. Klamecki, *Materials and process in manufacturing*, 9th ed. Upper Saddle River: Prentice Hall, 1997.
- [2] M. Subhani, "A Study on the Behaviour of Guided Wave Propagation in Utility Timber Poles," Doctoral Dissertation, University of Technology Sydney, Australia, 2014.
- [3] G. R. Lowe Jr and G. A. Baum, "Electrical conductivity of single wood pulp fibers," 1978.
- [4] F. Zain. (2017). *Different Types of Defects in Timber*. Available: <http://civilblog.org/2017/05/30/different-types-defects-timber/>
- [5] U. Dackermann *et al.*, "In situ assessment of structural timber using stress-wave measurements," *Materials and Structures*, vol. 47, no. 5, pp. 787-803, 2014.
- [6] J. A. Dos Santos, *The Application of Stress-wave Theory to Piles: Science, Technology and Practice: Proceedings of the 8th International Conference on the Application of Stress-Wave Theory to Piles*. Lisbon, Portugal: IOS Press, 2008.
- [7] F. Seco and A. R. Jiménez, "Modelling the generation and propagation of ultrasonic signals in cylindrical waveguides," in *Ultrasonic waves*, A. S. Jr., Ed.: InTechOpen, 2012, pp. 1-28.
- [8] D. C. Gazis, "Three-dimensional investigation of the propagation of waves in hollow circular cylinders. I. Analytical foundation," *The journal of the Acoustical Society of America*, vol. 31, no. 5, pp. 568-573, 1959.
- [9] J. L. Rose, *Ultrasonic guided waves in solid media*. Cambridge University Press, 2014.
- [10] M. Subhani, J. Li, and B. Samali, "A comparative study of guided wave propagation in timber poles with isotropic and transversely isotropic material models," *Journal of civil structural health monitoring*, vol. 3, no. 2, pp. 65-79, 2013.
- [11] M. Subhani, J. C. Li, H. Gravenkamp, and B. Samali, "Effect of elastic modulus and poisson's ratio on guided wave dispersion using transversely isotropic material modelling," in *Advanced Materials Research*, 2013, vol. 778, pp. 303-311: Trans Tech Publ.
- [12] M. Subhani, J. Li, B. Samali, and K. Crews, "Reducing the effect of wave dispersion in a timber pole based on transversely isotropic material modelling," *Construction and Building Materials*, vol. 102, pp. 985-998, 2016.
- [13] M. Subhani, J. Li, and B. Samali, "A study of guided wave propagation in timber pole using spectral finite element method," in *Proceedings of the 19th World Conference on Non-Destructive Testing (WCNDT 2016), 13-17 June 2016, Munich, Germany, 2016*, pp. 2242-2251.
- [14] M. Subhani, J. Li, B. Samali, and N. Yan, "Determination of the embedded lengths of electricity timber poles utilising flexural wave generated from impact," *Australian Journal of Structural Engineering*, vol. 14, no. 1, pp. 85-96, 2013.
- [15] Y. Yu and N. Yan, "Numerical study on guided wave propagation in wood utility poles: Finite element modelling and parametric sensitivity analysis," *Applied Sciences*, vol. 7, no. 10, p. 1063, 2017.
- [16] N. Yan, J. Li, U. Dackermann, and B. Samali, "Numerical and experimental investigations of stress wave propagation in utility poles under soil influence," in *From Materials to Structures: Advancement Through Innovation-Proceedings of the 22nd Australasian Conference on the Mechanics of Structures and Materials, ACMSM 2012*, 2013.



- [17] R. N. Emerson, D. G. Pollock, J. A. Kainz, K. J. Fridley, D. McLean, and R. J. Ross, "Nondestructive evaluation techniques for timber bridges," in *V World conference on timber engineering. Montreux, Switzerland, 1998*, vol. 1, pp. 670-677.
- [18] B. Kasal and R. W. Anthony, "Advances in in situ evaluation of timber structures," *Progress in Structural Engineering and Materials*, vol. 6, no. 2, pp. 94-103, 2004.
- [19] H. Kolsky, *Stress waves in solids*. Courier Corporation, 1963.
- [20] K. F. Graff, *Wave motion in elastic solids*. Courier Corporation, 2012.
- [21] K. Lepinay and F. Lorut, "Three-dimensional semiconductor device investigation using focused ion beam and scanning electron microscopy imaging (FIB/SEM Tomography)," *Microscopy and Microanalysis*, vol. 19, no. 1, pp. 85-92, 2013.
- [22] M. Riggio, F. Prandi, R. De Amicis, and M. Piazza, "Close Range Photogrammetry and NDT imaging techniques for the characterization of timber structural elements," in *Proceedings International Conference on Structural Health Assessment of Timber Structures (SHATIS), Lisbon, Portugal, 2011*.
- [23] L. Socco, L. Sambuelli, R. Martinis, E. Comino, and G. Nicolotti, "Feasibility of ultrasonic tomography for nondestructive testing of decay on living trees," *Research in Nondestructive Evaluation*, vol. 15, no. 1, pp. 31-54, 2004.
- [24] N. E. R. Center. (2014). *Wave Propagation*. Available: <https://www.nde-ed.org/EducationResources/CommunityCollege/Ultrasonics/Physics/wavepropagation.php>
- [25] H. Wang, "Theoretical evaluation of embedded plate-like and solid cylindrical concrete structures with guided waves," Northwestern University, 2004.
- [26] F. Seco and A. R. Jiménez, "Modelling the generation and propagation of ultrasonic signals in cylindrical waveguides," in *Ultrasonic waves: InTech, 2012*.
- [27] J. Zemanek Jr, "An experimental and theoretical investigation of elastic wave propagation in a cylinder," CALIFORNIA UNIV LOS ANGELES 1962.
- [28] F. Honarvar, E. Enjilela, A. N. Sinclair, and S. A. Mirnezami, "Wave propagation in transversely isotropic cylinders," *International journal of solids and structures*, vol. 44, no. 16, pp. 5236-5246, 2007.
- [29] N. T. Mascia and F. A. R. Lahr, "Remarks on orthotropic elastic models applied to wood," *Materials Research*, vol. 9, no. 3, pp. 301-310, 2006.
- [30] D. W. Green, J. E. Winandy, and D. E. Kretschmann, "Mechanical properties of wood," *Wood handbook: wood as an engineering material. Madison, WI: USDA Forest Service, Forest Products Laboratory, 1999. General technical report FPL; GTR-113: Pages 4.1-4.45*, vol. 113, 1999.
- [31] D. E. Kretschmann, "Mechanical properties of wood," in *Wood handbook: wood as an engineering material*, vol. 113 Wisconsin: Forest Products Laboratory, 2010, pp. 5.1-5.46.
- [32] D. A. Russell, "Acoustics and vibration animations," *Penn State Graduate Program in Acoustics*, 2001.
- [33] B. J. Tucker, D. A. Bender, D. G. Pollock, and M. P. Wolcott, "Ultrasonic plate wave evaluation of natural fiber composite panels," *Wood and fiber science*, vol. 35, no. 2, pp. 266-281, 2007.
- [34] I. Elishakoff, *Mechanical vibration: where do we stand?* Springer Science & Business Media, 2007.
- [35] H. A. Winston, F. Sun, and B. S. Annigeri, "Structural health monitoring with piezoelectric active sensors," *Journal of Engineering for Gas Turbines and Power (Transactions of the ASME)*, vol. 123, no. 2, pp. 353-358, 2001.

- [36] G. R. Edwards and T.-H. Gan, "Detection of corrosion in offshore risers using guided ultrasonic waves," in *ASME 2007 26th International Conference on Offshore Mechanics and Arctic Engineering*, 2007, pp. 377-384: American Society of Mechanical Engineers.
- [37] M. Silk and K. Bainton, "The propagation in metal tubing of ultrasonic wave modes equivalent to Lamb waves," *Ultrasonics*, vol. 17, no. 1, pp. 11-19, 1979.
- [38] D. Alleyne and P. Cawley, "The excitation of Lamb waves in pipes using dry-coupled piezoelectric transducers," *Journal of Nondestructive Evaluation*, vol. 15, no. 1, pp. 11-20, 1996.
- [39] C. Multiphysics, "Introduction to COMSOL Multiphysics®," *COMSOL Multiphysics, Burlington, MA, accessed Feb*, vol. 9, p. 2018, 1998.
- [40] K. Steiger and P. Mokřý, "Finite element analysis of the macro fiber composite actuator: macroscopic elastic and piezoelectric properties and active control thereof by means of negative capacitance shunt circuit," *Smart Materials and Structures*, vol. 24, no. 2, p. 025026, 2015.
- [41] M. Subhani, J. Li, and B. Samali, "Separation of longitudinal and flexural wave in a cylindrical structure based on sensor arrangement for non-destructive evaluation," *Journal of civil structural health monitoring*, vol. 6, no. 3, pp. 411-427, 2016.
- [42] S. Marburg, "Six boundary elements per wavelength: Is that enough?," *Journal of Computational Acoustics*, vol. 10, no. 01, pp. 25-51, 2002.
- [43] S. Mustapha and L. Ye, "Leaky and non-leaky behaviours of guided waves in CF/EP sandwich structures," *Wave Motion*, vol. 51, no. 6, pp. 905-918, 2014.
- [44] W. R. Lovelace, "The wood pole 2005: Design considerations, service benefits, and economic reward," *Hi-Line Engineering, LLC, Tech. Rep.*, 2005.
- [45] W.-f. DUAN, X.-h. LIAO, J.-s. JIN, and Y.-q. WANG, "Numerical modeling of pile-soil interface and numerical analysis of single pile QS curve [J]," *Journal of Harbin University of Civil Engineering and Architecture*, vol. 5, 2001.
- [46] H. Vanlangen, "Numerical analysis of soil-structure interaction," Doctoral Thesis, Technische Univ., Delft. Geotechnical Lab., Netherlands, 1991.
- [47] G. Zhang and J.-M. Zhang, "Numerical modeling of soil-structure interface of a concrete-faced rockfill dam," *Computers and Geotechnics*, vol. 36, no. 5, pp. 762-772, 2009.
- [48] D. M. Potts, L. Zdravkovic, T. I. Addenbrooke, K. G. Higgins, and N. Kovacevic, *Finite element analysis in geotechnical engineering: application*. London: Thomas Telford, 2001.
- [49] S. Materials, "Macro Fiber composites," ed: Smart Materials Company, 2017.
- [50] D. Bieker and S. Rust, "Non-destructive estimation of sapwood and heartwood width in Scots pine (*Pinus sylvestris* L.)," *Silva Fennica*, vol. 44, no. 2, pp. 267-273, 2010.
- [51] M. A. Colominas, G. Schlotthauer, and M. E. Torres, "Improved complete ensemble EMD: A suitable tool for biomedical signal processing," *Biomedical Signal Processing and Control*, vol. 14, pp. 19-29, 2014.
- [52] M. A. Fakhri, S. Mustapha, J. Tarraf, G. Ayoub, and R. Hamade, "Detection and assessment of flaws in friction stir welded joints using ultrasonic guided waves: experimental and finite element analysis," *Mechanical Systems and Signal Processing*, vol. 101, pp. 516-534, 2018.
- [53] B. Pavlakovic and M. Lowe, "Disperse Software Manual Version 2.0. 1 6B," *Imperial College, London, UK*, 2003.
- [54] R. Marquardt. (2012, 1 November 2018). *Extending Wood Pole Life With Remedial Preservatives*. Available:

<https://www.utilityproducts.com/home/article/16002834/extending-wood-pole-life-with-remedial-preservatives>

- [55] J. El Najjar and S. Mustapha, "Understanding the Wave Propagation Behavior in Timber Structures towards Application in the Assessment of Utility Timber Poles," *Civil Structural Health Monitoring*, 2020.

